ΕΘΝΙΚΟ ΚΑΙ ΚΑΠΟΔΙΣΤΡΙΑΚΟ ΠΑΝΕΠΙΣΤΗΜΙΟ ΑΘΗΝΩΝ

ΙΑΤΡΙΚΗ ΣΧΟΛΗ

Β' ΕΡΓΑΣΤΗΡΙΟ ΑΚΤΙΝΟΛΟΓΙΑΣ

ΓΕΝΙΚΟ ΠΑΝΕΠΙΣΤΗΜΙΑΚΟ ΝΟΣΟΚΟΜΕΙΟ 'ΑΤΤΙΚΟΝ'

ΔΙΔΑΚΤΟΡΙΚΗ ΔΙΑΤΡΙΒΗ

Πατατούκα Γεωργίου

Θέμα: *Μέτρηση αιμοδυναμικών χαρακτηριστικών με απεικόνιση Μαγνητικού Συντονισμού*

3μελής Συμβουλευτική Επιτροπή

Γουλιάμος Αθανάσιος Κελέκης Νικόλαος Ευσταθόπουλος Ευστάθιος

(ΕΠΙΒΛΕΠΩΝ ΜΕΛΟΣ ΔΕΠ)

ΕΥΧΑΡΙΣΤΙΕΣ

Με τις παρακάτω σύντομες προτάσεις, ο συγγραφέας του παρόντος πονήματος θα ήθελε να εκφράσει τις ευχαριστίες του σε ένα σύνολο ανθρώπων χωρίς τους οποίους η ολοκλήρωση της διατριβής δεν θα ήταν δυνατή.

Στον Καθηγητή Ακτινολογίας/Ακτινοδιαγνωστικής της Ιατρικής Σχολής του Ε.Κ.ΠΑ. και Διευθυντή του Β' Εργαστηρίου Ακτινολογίας του Π.Γ.Ν. «ΑΤΤΙΚΟΝ» ***κ. Νικόλαο Κελέκη*** για την αμέριστη συμπαράστασή του σε κάθε βήμα αυτής της διαδικασίας.

Στον Αναπληρωτή Καθηγητή Ιατρικής Φυσικής της Ιατρικής Σχολής του Ε.Κ.ΠΑ ***κ. Ευστάθιο Ευσταθόπουλο*** χωρίς τον οποίον η εργασία αυτή δεν θα είχε ξεκινήσει, δεν θα είχε εξελιχθεί και δεν θα ολοκληρωνόταν ποτέ.

Στον Καθηγητή Ακτινολογίας/Ακτινοδιαγνωστικής της Ιατρικής Σχολής του Ε.Κ.ΠΑ. ***κ. Αθανάσιο Γουλιάμο*** για τις πολύτιμες συμβουλές του και τις παρατηρήσεις του.

Ο συγγραφέας ευχαριστεί ιδιαίτερα τους:

Δρ. Πλατώνη Καλλιόπη Ακτινοφυσικό, Δρ. Κυπραίου Ευφροσύνη Ακτινοθεραπευτή-Ογκολόγο, την Δρ. Κουγιουμτζοπούλου Ανδρομάχη Ακτινοθευτή-Ογκολόγο, κα Διλβόη Μαρία Ακτινοφυσικό, τον Αναπληρωτή Καθηγητή Ακτινοθεραπευτικής Ογκολογίας κ. Κουλουλία Βασίλειο, την κα Καζέρου Ασπασία Ακτινοφυσικό, κ. Αργυρόπουλο Γεώργιο Ακτινοφυσικό, την κα Κορδολαίμη Σοφία Ακτινοφυσικό, κα Πλουσή Αγάπη Ακτινοφυσικό, κ. Παπαδόγιαννη Παναγιώτη Ακτινοφυσικό, κα Θραψανιώτη Ζωή Ακτινοφυσικό, κα Κότη Γεωργία Διοικητικό Προσωπικό «ΑΤΤΙΚΟ»

ΓΙΑ ΤΗΝ ΑΓΑΠΗ ΤΟΥΣ . ΓΙΑ ΤΗ ΒΟΗΘΕΙΑ ΤΟΥΣ.

"The most beautiful experience we can have is the mysterious. It is the fundamental emotion that stands at the cradle of true art and true science."

— **Albert Einstein**, **The World As I See It**

"The man who moves a mountain begins by carrying away small stones."

— **Confucius**, **Confucius: The Analects**

ΣΚΟΠΟΣ

Ο σκοπός της παρούσας διδακτορικής διατριβής είναι να παρουσιάσει και να αναδείξει στον αναγνώστη τα αποτελέσματα από μια σειρά μετρήσεων, οι οποίες αφορούν στη μελέτη αιμοδυναμικών χαρακτηριστικών με τη χρήση μαγνητικής τομογραφίας.

Καθώς στη διεθνή βιβλιογραφία- και κατ' επέκταση στην κλινική πράξη- παρουσιάζονται ολοένα και περισσότεροι παράγοντες οι οποίοι φαίνονται να συνδέονται με την αιμοδυναμική κατάσταση του ανθρώπου, αποτελεί ανάγκη η επιστημονική διερεύνηση τους, η οποία πρέπει και μπορεί να οδηγήσει την επιστημονική κοινότητα στη βαθύτερη κατανόησή τους και σαν αποτέλεσμα στην πιο αποτελεσματική τους χρήση για την εξαγωγή ορθών κλινικών συμπερασμάτων.

Ένα αιμοδυναμικό χαρακτηριστικό το οποίο τα τελευταία χρόνια 'απολαμβάνει' την ιδιαίτερη εκτίμηση της διεθνούς ιατρικής επιστημονικής κοινότητας είναι και η 'τοιχωματική τάση διάτμησης' –'WALL SHEAR STRESS (WSS)'. Η τάση διάτμησης του αγγειακού τοιχώματος ορίζεται ως η δύναμη ανά μονάδα επιφάνειας, την οποία ασκεί το αίμα (ρευστό) στο αγγειακό τοίχωμα κατά την ροή του εντός του αγγειακού αυλού.

Υπάρχει ένα εκτενές σύνολο διεθνών δημοσιεύσεων, το οποίο αφορά στη σύνδεση του εν λόγω αιμοδυναμικού χαρακτηριστικού με ένα ευρύ φάσμα κλινικών περιπτώσεων και κυρίως με παθήσεις που αφορούν στο σχηματισμό, την πρόοδο και την κατακερμάτιση της αγγειακής αρωματικής πλάκας.

Πάρα το γεγονός ότι μακροσκοπικά, η παραπάνω συσχέτιση φαίνεται να είναι σε ισχύ, παρατηρήθηκε ένα έλλειμμα ως προς την κατανόησή των φυσικομαθηματικών φορμαλισμών ο οποίοι οδηγούν στην τελική παραμετροποίηση (μαθηματική σχέση-εξίσωση) αυτό του μεγέθους.

Για τον λόγο αυτόν η παρούσα εργασία αποτελεί έναν τρόπο –το μοναδικό έως τώρα σύμφωνα με τη διεθνή βιβλιογραφία- σύνδεσης της φυσικομαθηματικής υπόστασης του παράγοντα αυτού με την κλινική του υπόσταση.

Πιο αναλυτικά, μελετήθηκε το WSS σε ένα σύνολο ασθενών, οι οποίοι υπεβλήθησαν σε μαγνητική αγγειογραφία στο Β' εργαστήριο Ακτινολογίας της Ιατρικής Σχολής του Εθνικού και Καποδιστριακού Πανεπιστήμιου Αθηνών. Στη συνέχεια υπολογίστηκε με βάση το σύνολο των μαθηματικών σχέσεων οι οποίες το περιγράφουν ,ώστε να ελεγχθεί εάν ισχύει η θεωρητική (φυσικομαθηματική) ισοδυναμία τους στην κλινική πράξη.

Τέλος, τα ίδια τα μεγέθη από τα οποία απορρέουν οι φορμαλισμοί της διατρητικής τάσης αγγειακού τοιχώματος, μελετήθηκαν σε πλήρως ελεγχόμενες συνθήκες εργαστηρίου (in vitro) με σκοπό την πλήρη κατανόησή και περιγραφή του εν λόγω αιμοδυναμικού χαρακτηριστικού.

ΠΕΡΙΛΗΨΗ

Στο παρόν μέρος παρουσιάζεται μια σύντομη περίληψη των περιεχομένων της παρούσας διατριβής.

Στο ΚΕΦΑΛΑΙΟ 1 παρουσιάζονται μερικές από τις πιο βασικές και θεμελιώδης αρχές της ρευστοδυναμικής. Πιο συγκεκριμένα γίνεται αναφορά στις εξισώσεις Navier- Stokes οι οποίες μαζί με την εξίσωση του συνεχούς της μάζας και υπό συγκεκριμένες συνθήκες περιορισμού, οδηγούν στο φορμαλισμό της ροής κατά Poiseuille. Είναι αυτές οι εξισώσεις και τα επαγόμενα από αυτές χαρακτηριστικά ροής, όπως η διατμητική τάση των αγγειακών τοιχωμάτων, αυτά τα οποία θα αποτελέσουν στα επόμενα κεφάλαια το αντικείμενο διερεύνησης.

Το ΚΕΦΑΛΑΙΟ 2 κατά ένα παρόμοιο τρόπο αναφέρεται περιγραφικά στο δεύτερο βασικό άξονα της παρούσας διατριβής, δηλαδή την απεικόνιση με Μαγνητικό Συντονισμό. Αναλυτικότερα χαρακτηριστικά όπως η ιδιοστροφορμή, η συνολική μαγνήτιση και άλλα παρουσιάζονται στον αναγνώστη, καθώς και τα βασικά χαρακτηριστικά του Μαγνητικού Τομογράφου. Έμφαση δίνεται στην ανάλυση της αρχιτεκτονικής των ακολουθιών της μαγνητικής τομογραφίας αλλά και ακόμα περισσότερο στη νεοεισελθείσα τεχνική της Μαγνητικής Αγγειογραφίας, στην οποία βασίζονται οι λήψεις όλων των δεδομένων στην εργασία αυτή.

Το ΚΕΦΑΛΑΙΟ 3παρουσιαζει τα υλικά και τη μέθοδο που ακολουθήθηκαν για τον υπολογισμό του WSS στην κλινική πράξη. Αρχικά παρουσιάζεται η εκτενέστερη έως τώρα βιβλιογραφική ερεύνα η οποία παρουσιάζει τα ευρήματα για το WSS και τις τιμές που παίρνει ανά τμήμα του αγγειακού δένδρου. Επιπλέον περιγράφονται αναλυτικά όλες οι παράμετροι της μεθόδου που ακολουθήθηκε για τον υπολογισμό της αγγειακής τάσης διάτμησης καθώς και το δείγμα των ασθενών οι οποίοι συμπεριελήφθησαν στην μελέτη.

Το ΚΕΦΑΛΙΑΟ 4 με παρεμφερή τρόπο παρουσιάζει τα υλικά και τη μέθοδο που ακολουθήθηκε για τον υπολογισμό των θεμελιωδών χαρακτηριστικών της αιματικής ροής σε συνθήκες εργαστήριου, πλήρως ελεγχόμενες, και παρουσιάζονται και περιγράφονται αναλυτικά όλα τα επιμέρους τμήματα του εξοπλισμού και ο ρόλος τους στην συνολική συμπεριφορά της πειραματικής αυτής διάταξης.

Στα ΚΕΦΑΛΑΙΑ 5 και 6 παρουσιάζονται όλα τα αποτελέσματα και από τα δυο μέρη (in-vivo and in-vitro) υπό τη μορφή πινάκων και γραφημάτων.

Το ΚΕΦΑΛΑΙΟ 7 χωρίζεται στο τμήμα Ι και ΙΙ τα οποία γίνεται η ανάλυση και ο σχολιασμός των αποτελεσμάτων που παρουσιάστηκαν στα κεφαλαία 5 (Ι) και 6 (ΙΙ) αντίστοιχα.

Το ΚΕΦΑΛΑΙΟ 8 οδηγεί τον αναγνώστη στο σύνολο των συμπερασμάτων που αφορούν στην κατανόηση των αιμοδυναμικών παραγόντων και τη συσχέτιση τους με την κλινική πράξη.

Το περιεχόμενο της διατριβής ολοκληρώνεται με την απαραίτητη αναφορά στους περιορισμούς που αναπόφευκτα παρουσιάζονται σε κάθε ερευνητική εργασία αλλά και στις μελλοντικές προεκτάσεις, οι οποίες μπορούν να συνεχίσουν το έργο αυτής της διατριβής το οποίο είναι η μελέτη των αιμοδυναμικών χαρακτηριστικών με τη χρήση μαγνητικής αγγειογραφίας και η βοήθεια που η κατανόηση τους μπορεί να προσφέρει στην ιατρική κοινότητα.

ΠΙΝΑΚΑΣ ΠΕΡΙΕΧΟΜΕΝΩΝ

1.8 Αλληλεπίδραση των παραγόντων ροής και η επίδραση τους στην αιματική ροή

ΚΕΦΑΛΑΙΟ 2

ΑΠΕΙΚΟΝΙΣΗ ΜΑΓΝΗΤΙΚΟΥ ΣΥΝΟΤΝΙΣΜΟΥ

2.1 Γενικοί ορισμοί

2.2 Εξοπλισμός

ΚΕΦΑΛΑΙΟ 5

ΙΝ VIVO ΑΠΟΤΕΛΕΣΜΑΤΑ

ΚΕΦΑΛΑΙΟ 6

ΙΝ VITRO ΑΠΟΤΕΛΕΣΜΑΤΑ

ΚΕΦΑΛΑΙΟ 7

Α. IN VIVO ΑΝΑΛΥΣΗ

Β. IN VITRO ΑΝΑΛΥΣΗ

ΣΥΜΠΕΡΑΣΜΑΤΑ

IN VIVO

PURPOSE

The purpose of the present PhD thesis is to present and underline to the reader the results generated from a series of measurements that were made regarding the study of the hemodynamic characteristics using magnetic resonance imaging.

Due to the fact that in the international literature and bibliography-and within the everyday clinical practice- there seems to be appearing more and more newly presented factors that seem to be linked to the hemodynamic and rheological condition of the human body, it seems more evident than ever that there is an absolute need for the complete and scientific study and knowledge of these factors.

A relatively newly introduced such factor id wall shear stress (WSS), that describes the force per unit are that is exerted on the arterial wall by the flowing blood. There seem to be an increasing interest in this factor as the international literature is beginning to accept the fact that this factor not only is it linked, but also it seems to be playing a vital role in the genesis, progression and even in the rapture of the atheromatic plaque which in turn is related directly to the overall hemodynamic homeostasis of the human body.

Despite the fact that macroscopically this relationship between WSS and atheromatic plague seem to be valid, there seems to be a gap in the overall scientific understanding of the physical and mathematical formalism which lead to the final WSS equation(s).

This is the reason why this thesis comes to provide –for the first time to the best of our knowledge- the complete link between the mathematical, the physical and the clinical overview of this hemodynamic factor.

More in detail, WSS was measured in a cohort of patients that underwent magnetic resonance angiography (MRA), in our clinic at the second Department of Radiology of the Medical School of the National and Kapodestrian University of Athens at the General University hospital of Athens 'ATTIKON'. The acquired data was used to test the validity and equality of the four mathematical equations derived from the Poiseuille's theory of flow with the clinical practice.

Furthermore in-vitro experimentation was carried out under completely modulated rheological conditions and geometries' in order to study on first principles a number of fundamental hemodynamic factors from which the aforementioned equation(s) of flow are derived.

OVERVIEW

The layout of the present PhD thesis is described in the present section.

In CHAPTER 1, the reader is introduced to some of the most basic and fundamental fluid dynamics principles. More in particular the general fluid dynamics principles are introduced, including the Navier- Stokes set of equations, which together with the mass conservation equation, and following the imposed boundary conditions, they give rise – with their analytical solutions- to the Poiseuille's Law of fluid. Additionally the concepts of Newtonian and non-Newtonian fluid and flow are being described together with concepts such as pressure, Reynolds number and of course viscosity, WSR and WSS.

CHAPTER 2 deals with the second of the two main subjects of contained in this work, namely Magnetic Resonance Imaging. General concepts such as spin, net magnetization as well as the magnetic resonance imaging unit instrumentation. MR signal phase space encoding and sequence architecture are also describe with emphasis given in the newly introduced concept of Magnetic Resonance Angiography with its own parameters characteristics, limitation and applications to the human circulatory system.

CHAPTER 3 presents the materials and method that were followed in order to calculate WSS equations in clinical practice (IN-VIVO MATERIALS AND METHODS).Firstly a full international scientific bibliography is reviewed with emphasis given to ALL previously measured WSS values and their corresponding segments of the human arterial tree. Furthermore, a full description and analysis is given to the patient cohort, the MR angiographic imaging sequence parameters and to the four fundamental WSS equations of which the equivalence was tested.

CHAPTER 4 in a similar way describes the IN-VITRO set up and instrumentation that was used in order to simulate fully controlled blood flow in straight and stenotic segments using the appropriate apparatus such as the flow pump the ECG generator, the blood mimicking fluid, the programmable logic controller etc.

CHAPTERS 5 and 6 display all the acquired data from the in-vivo and in-vitro set ups in tabulated or graphical format depending on the nature of the variable studied. In addition any results of the statistical tests performed are presented in these chapters.

CHAPTERS 7 is divided into two sections namely I and II. The first refers to the analysis and discussion of the in vivo results presented in chapter 5 and the second in a similar way refers to the analysis and discussion of the in-vitro results presented n chapter 6.

CHAPTER 8 takes the reader to the sum of all the conclusions that can be drawn based on the analysis and discussion of the results in both for the in vivo (WSS) or in vitro data (parabolicity, stenosis percentage calculation).

The thesis concludes with a brief presentation of the inevitable limitations of the work presented and finally with a complete proposal for future work that can bring the study of hemodynamic parameters using MRA to a new era.

TABLE OF CONTENTS

CHAPTER 2

Nuclear Magnetic Resonance

CHAPTER 3

IN-VIVO

CHAPTER 4

IN VITRO

CHAPTER 5

IN VIVO RESULTS

CHAPTER 6

IN VITRO RESULTS

CHAPTER 7

A. IN VIVO ANALYSIS

B.IN VITRO ANALYSIS

CONCLUSIONS

IN VIVO

IN VITRO

CHAPTER 1

Fluid dynamics Principles

1.1 General principles

For the purpose of complete flow analysis two important general principles must be examined: *mass* and *momentum conservation*.

According to **mass conservation**, the total amount of mass in the system remains stable. The control volume is assumed to be all the blood in the selected region. The volume of the control volume is constant, *as the arteries are rigid*. *The blood is incompressible*, implying that its density (mass per unit volume) is constant (at any point and at any time). Occasionally, the mass in the control volume changes in time. Therefore:

(Mass flux in) = (Mass flux out) + (Net rate of increase of mass in control volume). *(1)*

Equation (*1*) is verified in all situations.

According to the **conservation of momentum**, the total amount of momentum in the system changes as a result of forces acting upon it. As stated in Newton's second law, the rate of change of momentum equals the force. If no force is acting then the momentum remains constant. These conservation laws are applied to a control volume – a particular region of a fluid. The forces acting on the fluid can be classified into *surface, stress and body* forces. ***Pressure is a surface force***, acting at the surface of the fluid. *Stress forces*, arise in viscous fluids due to ***interaction of the fluid with the boundary***. *Body forces* ***act over the interior of the fluid***, as often considered gravity and viscous forces. For the application of momentum conservation, the specification of the momentum flux into the control volume precedes; (it is a vector quantity with dimensions N/m^2). The resultant force acting on the fluid in the control volume is the force due to pressure forces acting on the sides and ends of the vessels (gravitational, viscous and stress forces are neglected). Conservation of momentum implies:

(Momentum flux out) − (Momentum flux in) = (Forces acting on fluid in control volume), *(2)*

Equation (*2*) is applied only to steady flows (independent on time). If the flow is time-dependent the rate of change of momentum in the control volume should be taken in account too:

(Momentum flux out) − (Momentum flux in) + (Rate of increase of momentum within control volume) = (Forces acting on fluid in control volume). *(3)*

Reynolds Transport Theorem

The Reynolds Transport Theorem is a generalization of the principles of mass and momentum conservation. The rate of a physical quantity that obeys to conservation in the system, is quantified in terms of other physical effects. The theorem is a conservation law that can, in principle, be applied to any conserved quantity (for instance: mass, linear and angular momentum, energy, charge).

Concerning a conserved quantity B in a control volume of the fluid:

(Rate of change of B in system) = (Rate of change of B in control volume) + (Flux of B through control surface) (*4*)

By definition of a conserved quantity, its rate of change can be quantified. Consequently, the left-hand side of the above equation in terms of other effects can be defined. In the case of steadiness, the rate of change of B in the control volume is zero. The flux through the control surface (the boundary of the control volume) is found in general by considering an infinitesimal area of the surface and finding the amount of B that flows through it. Integrating over the surface gives the total flux through the surface. The control volume considered so far with stable inlets and outlets, the fluid flowed uniformly and perpendicularly across them. For a general formula, β is defined as the amount of B per unit mass or intensive amount of B:

Quantity conserved B	***Usual formula***	***B***
Mass	Mass	Mass / m=1
Linear momentum	Mass times velocity	Momentum / m=u
Angular momentum	Perp. distance times momentum	Ang. momentum / m= r x u

The amount of B per unit volume is ρβ.

For the definitions of the infinitesimal volume, a small rectangle of area dA is considered on the surface. During a short time dt, a parallelepiped of fluid flows through the surface. The volume is the area of the base multiplied by the perpendicular height. In this case the base has area dA and the other edges are given by the vector u dt. The volume is therefore (u n) dA dt, where n is the unit normal vector to the surface. Hence the amount of B crossing the infinitesimal surface in the infinitesimal time is ρβ (u n) dA dt and the rate of crossing is: ρβ (u n) dA.

Therefore:

$$\text{(Flux of B through control surface)} = \int_{\text{Control surface}} \rho\beta\,(u\,n)\,dA \quad (5)$$

Model for definition of the flow profile in an artery

Previously uniform flow was assumed. This neglects the effects of the viscosity of the fluid. Viscosity is a kind of internal friction in the fluid. It also enforces a ***no-slip boundary condition*** on rigid surface, meaning that ***the velocity of the fluid at the wall equals the velocity of the wall***. For a pipe, this enforces ***the flow to be zero at the walls***. Hence the velocity is slow around the edges and rises to a maximum in the center of the pipe. Therefore the flow has a profile in space (the velocity u is a function of position). ***The resulting flow looks approximately like parabolic***. An equation for the velocity of the blood as a function of the position in the artery will be calculated. In order to investigate the flow profile, a simplified model is developed. Finding the profile enables the estimation of useful quantities and predictions to be made.

The simplifying assumptions are (concerning the geometry):

1. The artery to be a circular cylindrical tube;
2. The walls to be rigid;
3. The fluid: the blood as incompressible Newtonian fluid ;
4. The flow:
    i. Is steady (independent of time);
    ii. Is in the axial direction (parallel to the tube);
    iii. Is axisymmetric (stable after rotating the tube);
5. The flow is fully- developed (stable on every cross-section of the tube).

To find an equation for the velocity profile we need some governing equations.

Differential equations of fluid mechanics

The analysis of flow using the differential equations of fluid mechanics, expresses respectively mass and momentum conservation in a fluid.

The Continuity Equation

The Continuity Equation expresses mass conservation in a fluid. It may be derived by applying the Reynolds Transport Theorem for mass conservation (1) to a small cube with side length δx and letting $\delta x \rightarrow 0$.

The continuity equation is

$$\partial\rho/\partial t + \nabla(\rho u) = 0; \quad (6)$$

Where ρ(x, t) is the density and u(x, t) is velocity. In the case of incompressible fluids, ρ is constant, meaning that the continuity equation *(6)* becomes

$$\nabla u = 0; \textit{ (7)}$$

Hereafter the fluid is assumed to be incompressible.

Conservation of momentum

By applying the Reynolds Transport Theorem for momentum conservation *(3)* to a cubic box of side length δx and letting $\delta x \rightarrow 0$

$$\rho \left(\partial u/\partial t + (u \nabla) u\right) = F; \textit{ (8)}$$

Where F(x, t) is the force per unit volume acting on the fluid.

The expression $\partial u/\partial t + (u \nabla) u$ is the acceleration of a particle moving with the fluid. 'Moving with the fluid' expresses the fact that the Lagrangian frame rather than the Eulerian frame of reference is used. Therefore the left-hand side of *(8)* represents the rate of change of fluid momentum per unit volume in the Lagrangian frame of reference while the right-hand side represents the force per unit volume acting on the fluid. Thus *equation (8) is just Newton's second law expressed per unit volume.*

Stress–strain relationships

In order to find an expression for the force per unit volume, F, appearing in *(8)*, a relationship between the viscous forces acting on the fluid and the velocity field of the fluid is required. This is usually achieved by relating the stress and strain tensors of the fluid resulting to a constitutive equation for the fluid behavior. The stress tensor σ is a 3 x 3 matrix in 3 dimensions. If a hypothetical cross section in the fluid, on a plane with unit normal n, the force per unit area on this plane would be σ*n. The body force per unit volume in the fluid is then:

$F = \nabla E\ \sigma = \sigma_{ji} / \partial x_j$

Which is abbreviation for $\sum_i \sum_j (\sigma_{ji} / \partial x_j)\ e_i\ i,j = (1,3)$ *(9)*

The strain tensor ε is also a 3x3 matrix in 3 dimensions, defined by

$$\varepsilon_{ij} = \partial u_i / \partial x_j + \partial u_j / \partial x_i \textit{ (10)}$$

In Cartesian coordinates xi, where $u = (u_{ij})$ is the fluid velocity.

1.2 Types of fluid

Fluids are categorized according to the nature of the relationship between the stress tensor and the strain tensor:

Newtonian fluids obey a stress–strain relationship of the form

$$\sigma = 2\mu\varepsilon - pI; \quad (11)$$

Where p is the pressure and μ is the viscosity (which is constant), inviscid fluids obey

$$\sigma = -pI; \quad (12)$$

While other fluids have a more complicated relationship between the stress and strain tensors, which may depend on the time development of the fluid motion, as well as the current state.

The Navier–Stokes equation

The equations (*9*) and (*11*) are substituted into (*8*). For incompressible fluids: $\nabla u = 0$ (*7*), hence the viscous force term simplifies, resulting in the Navier–Stokes equation:

$$\rho\, \partial u/\partial t + (u\nabla)\, u = -\nabla p + \mu\nabla^2 u; \quad (13)$$

The term $-\nabla p$ is the pressure force per unit volume and $\mu\nabla^2 u$ is the force per unit volume due to the viscous stresses.

Model for definition of the flow profile in an artery

As aforementioned, the equations (*7*) and (*11*) express the mass and momentum balance for an incompressible Newtonian fluid. Referring to the model of an artery as formulated earlier, the velocity field u(x, t) and the pressure p(x, t) are now requested. Cylindrical polar coordinates (r, θ, and z) are used. The components of u (u_r, u_θ, u_z) and p are expressed as functions of r, θ, z and t. The assumptions made earlier to simplify the equations are used.

Specifically: the steady flow implies that the components of u and p do not depend on t, the flow in the axial direction implies that the u_r and u_θ are both zero (u_z and p are left), the axisymmetric flow implies that u_z and p do not depend on θ. Finally, that fully-developed flow implies that u_z does not depend on z. Functions u_z (r) and p(r , z) pending to be found. The continuity equation and azimuthal component of the Navier–Stokes equation are automatically satisfied. The radial and axial components of the Navier–Stokes equation respectively become

$$0 = -\partial p/\partial r, \quad 0 = -\partial p/\partial z + (\mu/r)\, \partial/\partial r\, (r^*\, \partial u_z/\partial r) \quad (14)$$

Equation (*14a*) implies that p is a function of z only, while differentiating (*14b*) with respect to z gives

$$\partial^2 / \partial z^2 = 0 \quad (15)$$

and solving this subject to $p = p_1$ at $z = 0$ and $p = p_2$ at $z = L$ thus

$$p = p_1 - [(p_1 - p_2)/L]\, z \quad (16)$$

Hence the pressure field drops linearly along the pipe, and it is constant across the cross-section. Substituting this expression for p into Equation (*25b*), the general solution is obtained

$$u_z = C_1 + C_2 \ln r - [(p_1 - p_2)/4\mu L]\, r^2 \quad (17)$$

The fact that lnr is unboundedly near $r = 0$, implies that $C_2 = 0$. The **no-slip boundary condition** implies that $u = 0$ at the boundary $r = pA/\pi$, and hence **the Poiseuille profile is obtained**:

$$u_z = [(p_1 - p_2)/4\pi\mu L]\, (A - \pi r^2) \quad (18)$$

Generalization of formula for mass flux definition

The flux of mass through an artery as aforementioned is given by $dm/dt = \rho A u$. However, in order this to be derived, the flow was assumed as:

- Incompressible,
- Uniform and
- Perpendicular to the cross-section.

In the case of an arterial model of non-uniform flow, the formula is adapted. In this case the length of fluid per unit time crossing the surface is u_z, which varies over the surface. The volume crossing an infinitesimal area dA per unit time is $u_z\, dA$ and the mass per unit time is $\rho u_z\, dA$. Hence

$$dm/dt = \int \rho u_z\, dA = \iint \rho u_z\, r\, dr\, d\theta. \quad (19)$$

This result could also be derived from the formula (*5*) for flux of a quantity across a surface (using $\beta = 1$ for mass):

$$dm/dt = \int_s \rho\, (u\, n)\, dS, \quad (20)$$

Where, S is the surface and dS is a small element of the surface area, (x, t) is the fluid density (now a function of space and time), u(x, t) is the fluid velocity (a vector function of space and time), n is the unit normal vector (constant if the surface is fixed and flat). The formula above is affirmed for any flow (in the present case, $un = u_z$).

Poiseuille flow

$$\text{The flow is } p = p_1 - (\Delta p\, z/\, L),\ u_z = (\Delta p/\, 4\pi\mu L) * (A - \pi r^2) \quad (21)$$

The volume flux along the pipe is

$$\int_{\text{Cross section}} u_z \, r \, dr \, d\theta = A^2 \, \Delta p / 8\pi\mu L \quad (22)$$

Which, for a given pressure gradient, is proportional to the fourth power of the diameter. Therefore if a pipe is replaced by one with double the diameter (other parameters remain constant) the flux will increase by a factor of 16.

Stress induced by the flow

Endothelial cells (lining the arterial walls) respond to the shear stress they experience from the blood flow. The initiation process of atherosclerosis is linked to the shear stress profile and time-dependence. Therefore it is important to define the shear stress in an artery. ***Shear stress is the force per unit area that the fluid exerts on the wall***. This is given by σn, where n is the outward pointing vector from the wall, which, in this case, equals − ˆr.

The correspondence of (*10*) in polar coordinates is quite complicated, resulting to:

$$\sigma(-\hat{r}) = (-pI + 2\mu\varepsilon)(-\hat{r}) = p\hat{r} - \mu(\partial u_\theta / \partial r)\hat{\theta} - \mu(\partial u_z / \partial r)\hat{z}. \quad (23)$$

The normal stress is therefore merely the pressure, while the shear stress (the tangential components) decomposes into the axial shear stress, proportional to the radial derivative of the axial velocity, and the azimuthal shear stress, proportional to the radial derivative of the azimuthal velocity.

Axial shear stress

In the case of Poiseuille flow, the axial shear stress is

$$-\mu \, (\partial u_z / \partial r)|_{r=1} = (\Delta p \sqrt{A}) / (2\sqrt{\pi} L) \quad (24)$$

Considering the azimuthal shear stress is zero and the normal stress is $p_1 - (\Delta p \, z)/ L$. The total drag force is the integral of the shear stress over the surface, which equals

$$(\Delta p \sqrt{A})/(2\sqrt{\pi} L) * (2\pi L \sqrt{(A/\pi)}) = A\Delta p$$

The fact of no acceleration of the fluid could also have led to the same result. Hence, the resultant force on the fluid must be zero. Considering the forces acting on the fluid, they are:

- The pressure force on the circular ends of the fluid and
- The stress forces exerted from the walls. The pressure force on the ends of the fluid is AΔp in the direction of the flow. Therefore the total stress force from the walls is AΔp opposing the flow. Since the pressure forces cancel out due to the circular symmetry, this force is the drag force from the walls (the force of the walls on the fluid). Thus the total shear stress force by the cells (the force of the fluid on the walls) equals AΔp.

Non-axisymmetric flow

To derive Poiseuille flow, axisymmetric flow was assumed. However, this need not be the case, as there are other solutions of the equations with broken symmetry. However, these are only observed for high Reynolds numbers, when the flow becomes turbulent. Another reason for the flow to become non-axisymmetric is if the pipe is not perfectly circular. ***Reynolds number*** is a dimensionless quantity used to describe a fluid flow.

The Assumptions of Poiseuille flow relate to assumptions of:

- axisymmetric flow
- fully developed flow
- rigid vessel with a uniform cross-section
- straight vessel, steady flow
- artery large enough that a Newtonian fluid model is appropriate

It is defined by: $R_e = \rho UL/\mu$ (*25*)

Where: ρ is the fluid density, U is a characteristic velocity scale, L is a characteristic length scale, and μ is the viscosity of the fluid.

The Reynolds number gives a qualitative description of the flow, and is an order of magnitude estimate. The precise value is usually not of great importance. For instance, the difference between a flow with Re = 60 and one with Re = 80 is often unimportant, but the difference between one with Re = 100 and Re = 1000 is important.

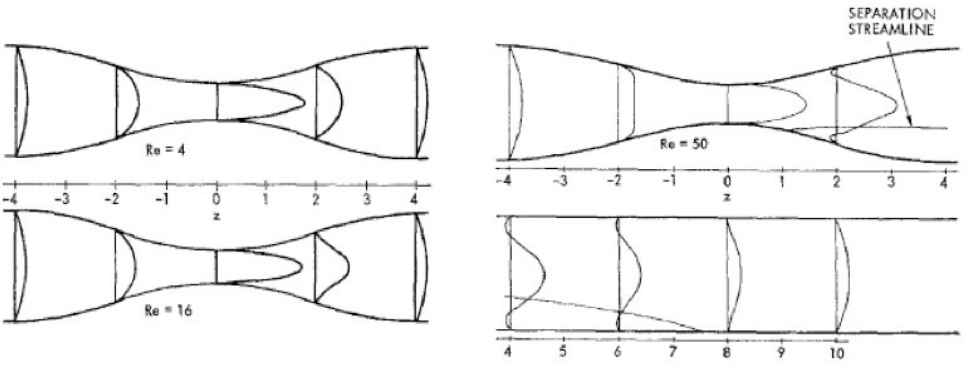

Fig.1a *Velocity profiles for axisymmetric model at various Re values.* [1]

1.3 Non-fully-developed flow

Arteries are usually long compared with their diameter having a regular cross-section, thus the assumption of fully developed flow is often reasonable. However: The cross-section may not be constant along the pipe, for example due to: Arterial taper, which tends to occur

in most arteries. Elasticity in the arterial walls, cause the cross-sectional area to change in response to a change in pressure, resulting in non-uniformities in the cross-section along the pipe. There may be entrance effects due to a change in the vessel, for instance: Flow in the ascending aorta is unlikely to be fully developed, since it is affected by the profile as it leaves the ventricle. Flow in a daughter artery just after a bifurcation is affected by the splitting of the flow in the parent vessel. Entrance effects persist for a distance proportional to *a Re*, where *a* is the radius of the artery and Re is the Reynolds number.

Effect of arterial curvature on the flow

The derivation of Poiseuille flow assumes the artery is straight. In fact, most arteries are curved, resulting in a significant effect on the flow structure. Eventually, it is still feasible to gain some insight using analytical techniques in the case when the centerline of the artery (the locus of centers of cross-sections of the pipe) is circular.

The other assumptions are the same as those used in the derivation of Poiseuille flow. The blood may be assumed as a Newtonian fluid and the application of Navier–Stokes equations with no-slip boundary conditions. All above considered in terms of a natural coordinate system of the pipe. Instead of x, y and z, the distance along the pipe, s and polar coordinates r and θ in the cross-section are used (fig.1b)

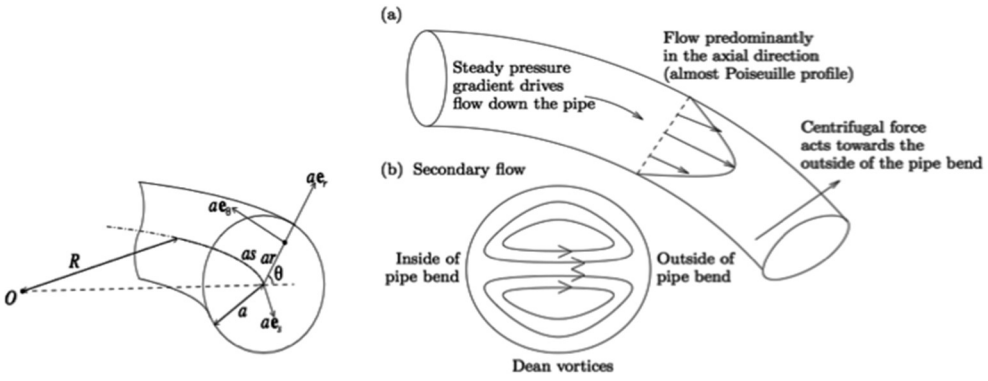

Fig.1b*: Dean flow. (a) Longitudinal cross-section, showing Poiseuille-like profile, (b) transverse cross-section, showing secondary flow, which forms Dean Vortices.*

After non dimensionalization, the system has just two non-dimensional parameters:

The non-dimensional: curvature $\delta = a/R$, and flux $\rho Q/\mu a$.

Simplification: Considering the limit as $\delta \rightarrow 0$, the system tends to a straight pipe (and the solution would be Poiseuille flow). However, a rescaling is initially made, in which long length

scales and high velocities in the axial direction are assumed. Hence as $\delta \to 0$, the centrifugal terms do not vanish (although the Coriolis terms do). The equations are significantly uncomplicated, notably in that the coordinate system effectively becomes like cylindrical polar coordinates. Though the non-dimensional flow is assumed small, a series solution may then be found using analytical techniques. The series solution result in

$$u_r = Q^2 u_{r,0} + Q^4 u_{r,1} + \ldots, \; u_\theta = Q^2 u_{\theta,0} + Q^4 u_{\theta,1} + \ldots, \; u_s = Q u_{s,0} + Q^3 u_{s,1} + Q^5 u_{s,2} + \ldots . (26)$$

The leading-order flow, $Qu_{s,0}$, is Poiseuille flow, in the axial direction. The largest correction to this flow the components $Q^2 u_{r,0}$ and $Q^2 u_{\theta,0}$, which describe Dean flow across the cross section of the pipe. This flow has two vortices one in each half of the pipe cross-section. The next correction, $Q^3 u_{s,1}$ causes the location of the maximal axial velocity to be moved towards the outside of the bend of the pipe. Poiseuille flow has a linear relationship between flow and pressure gradient. Interestingly, in the relationship between flow and pressure gradient in the curved pipe, the first few terms in the flow profile do not contribute to the axial flow rate. The departure from a linear relationship between flow and pressure gradient occurs at the fifth power:

$$Q = C_0 D + C_1 D^5 + \ldots, (27)$$

Where C_0 is the coefficient in Poiseuille flow.

Effect of unsteadiness in the flow

Flow in the cardiovascular system is not steady, but is rather highly pulsatile (fig.*2*), showing pressure and flow in the aorta. When the oscillations in the pressure gradient are sufficiently slow, there is enough time for Poiseuille flow to develop, meaning the profile at any fixed time looks like the Poiseuille flow solution with the same pressure gradient. This a quasi-steady solution, because the time-derivative terms in the Navier–Stokes equations may be neglected.

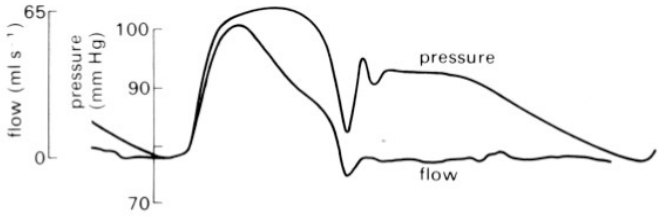

Fig.2 *Measured pressure and flow over the cardiac cycle*

Unsteady flow: High-frequency oscillations

In this case, the time-derivative term in the Navier–Stokes equations cannot be neglected. The flow is considered in the same model as above, except that p_1 and p_2 are functions of time. Assumptions remain for: axisymmetric flow, for flow is in the axial direction and fully developed (independent of z). As before, the continuity equation and azimuthal component of the Navier–Stokes equation are automatically satisfied. The radial and axial components respectively become

$$0 = -\partial p/\partial r,\ 0 = -\partial p/\partial z + (\mu/r)\,\partial/\partial r\,(r^*\,\partial u_z/\partial r) \quad (28)$$

Equation (14a) implies that p is a function of z and t only, and, by differentiating (28b) with respect to z, thus obtained as before

$$p = p_1 - [(p_1 - p_2)/L]\,z \quad (28b)$$

In order to solve the equation (*28b*), Δp should be prescribed as a function of time. For simplicity, it is assumed that the time-dependence oscillates sinusoidally, $\Delta p = p_o \exp(i\omega t)$, and also that $u_z = U_0 \exp(i\omega t)$. Substituting into Equation (28b):

$$a^2/r^*\,\partial/\partial r\,(r^*\,\partial U_o/\partial r) - i\alpha^2 U_o = -(a^2 p_o/\mu L) \quad (29)$$

Where $\alpha = \sqrt{(\rho\omega a^2/\mu)}$ is the Womersley number. The homogeneous equation of (*29*) (found by replacing the right-hand side with zero) implies solutions of the form $c_1 J_0(kr/a) + c_2 Y_0(kr/a)$, where $k = \sqrt{-i}\,\alpha$ and J_0 and Y_0 are Bessel functions (J_0 is the Bessel function of the first kind of zero order and Y_0 is the corresponding Bessel function of the second kind).

Unsteady flow: Bessel functions

$J_0(x)$ is regular at x = 0 and tends to 1 there, whereas $Y_0(x) \sim (2/\pi)(\ln(x/2) + \gamma)$ for $x \ll 1$ (where γ is Euler's constant). For large x, $J_0(x) \sim \sqrt{(2/\pi x)} * \cos(x - \pi/4)$ and $Y_0(x) \sim \sqrt{(2/\pi x)} * \sin(x - \pi/4)$

A particular solution of (*28*) is $U_0 = -ip_0/(L\omega)$. Thus the general solution is

$U_0 = c_1 J_0(kr) + c_2 Y_0(kr) - ip_0 L\omega$ (*30*)

The regularity condition is applied U_0 finite at r = 0 and the no-slip condition $U_0 = 0$ at $r = \pi/A$ to obtain the amplitude of the axial flow profile:

$U_0 = -(ia^2 p_0/\alpha^2 L\mu)(1 - (J_0(kr)/J_0(k\sqrt{(A/\pi)}))$ (*31*)

This is a Womersley flow profile:

$u_z = -(ia^2 p_0/\alpha^2 L\mu)(1 - (J_0(kr)/J_0(k\sqrt{(A/\pi)}))\,*\exp(i\omega t)$. (*32*)

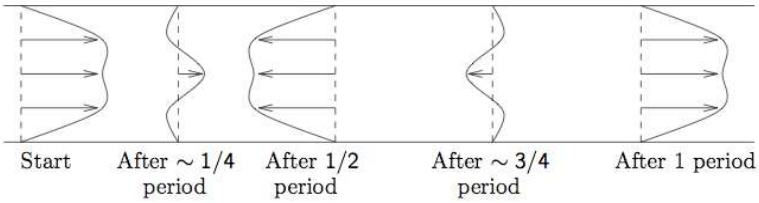

Fig.3 Womersley profile

1.4 Non-Newtonian flow

So far blood is treated as a Newtonian fluid, thus satisfying a stress–strain relationship of the form

$$\sigma = 2\mu\varepsilon - pI, \quad (33)$$

Where σ is the stress tensor, ε is the strain tensor, p is the pressure and μ is the viscosity (assumed constant). This is a remarkably good approximation to the behavior of many real fluids in widely differing flows. We now consider its validity as a model for blood.

Mechanical behavior of the red blood cells

Blood contains a multitude of constituents with different mechanical properties (water; 50%, formed elements; 48%, proteins; 4%, ions< 1% and others <1%), therefore it is far from being an ideal fluid. In fact, the complex mechanics of the red blood cells is usually the cause of the greatest inaccuracy associated with a Newtonian model. Developing an accurate model of these mechanics is challenging for the following reasons:

a) Cell–cell interactions: Red blood cells occupy 45% of the blood volume, and therefore blood is a highly concentrated suspension. Cells are closely packed and cell–cell interactions are important.

b) Alignment of cells: Red cells are not spherical; they have a biconcave shape. If the fluid shear is low, the cells are orientated randomly, but in high shear they align with the direction of the shear. The effective viscosity of the blood is much lower when the cells are aligned than when they have random orientations. Thus the effective viscosity decreases as shear increases (shear-thinning property of blood).

Mechanical behavior and implications of the red blood cells

Deformation of cells: As they flow along the arteries, the red blood cells deform significantly, meaning that a rigid-particle model to describe them is probably inaccurate. In order to pass through the narrow capillaries the cells adopt a completely different shape.

Particulate nature of cells: The cells have diameter of around 8 μm, and in small vessels this is a substantial proportion of the vessel diameter. In the capillaries it may be larger than the vessel diameter. With such relatively large particles in a small vessel, a continuum model may not be justified.

Despite these complexities, **it is actually reasonable to treat blood as a Newtonian fluid** under many circumstances, for *instance if the vessel is relatively large compared with the red cell size, and the shear stays in a fairly narrow range of values. In small vessels in particular, the Newtonian model may not be the most appropriate.* In this case we need the different properties of blood under different shear rates should be taken in account. In a model of the capillaries the red cells individually should be taken in account.

Relationship between stress and shear rate

In smaller vessels the effective viscosity of the blood is highly dependent on the local fluid flow, in particular the shear rate. For realistic blood models a working definition of the effective viscosity should be formulated, respectively to the case of a Newtonian fluid. The flow is assumed as a simple shear u = u (y)$\hat{x}$, where $\hat{x}$ is the unit vector in the x-direction and consider the force it exerts on a surface with unit normal $\hat{y}$. The shear stress τ (component of stress that is tangential to the surface) is given by

$$\tau = \mu\,(\partial u/\partial y) = \mu\,(d\gamma/dt), \quad (34)$$

Where *dγ/dt is the shear rate*.

Newtonian fluids have the important property that the viscosity μ is constant. To find the effective viscosity of a non-Newtonian fluid, the shear stress and the shear rate in an experiment should be measured. By analogy the effective viscosity is defined

$$\mu_{eff} = \tau / (d\gamma/dt) \quad (35)$$

Blood models

Shear-thinning fluid model:

Shear-thinning fluids have an effective viscosity μ_{eff} that is a decreasing function of the shear rate dγ/dt. Their properties under shear may be defined by specifying the functional form of $\mu_{eff}\,(d\gamma/dt)$ that is the dependence of μ_{eff} on dγ/dt. Therefore

$$\tau = \mu_{eff}\,(d\gamma/dt) \quad (36)$$

The bulk properties of the fluid can be assumed as being Newtonian.

Viscoelastic model:

In common with many biological materials, the effective viscosity of blood depends on the time development of the shear rate as well as the present value. Such fluids are called viscoelastic, and their properties are a combination of fluid and solid properties.[2]

1.5 Fluid dynamics in circulatory system

The function of the circulation is to service the needs of the body tissues, to transport nutrients to the body tissues, to transport waste products away, to conduct hormones from one part of the body to another, and in general, to maintain an appropriate environment in all the tissue fluids of the body for optimal survival and function of the cells. The rate of blood flow through most tissues is controlled in response to tissue need for nutrients. The heart and circulation in turn are controlled to provide the necessary cardiac output and arterial pressure to cause the needed tissue blood flow.[3]

Physical Characteristics of the Circulation

The circulation is divided into the systemic circulation and the pulmonary circulation. Because the systemic circulation supplies blood flow to all the tissues of the body except the lungs, it is also called the greater circulation or peripheral circulation.

Functionality of the Circulation.

The function of the arteries is to transport blood under high pressure to the tissues. For this reason, the arteries have strong vascular walls, and blood flows at a high velocity in the arteries. The arterioles are the last small branches of the arterial system; they act as control conduits through which blood is released into the capillaries. The arteriole has a strong muscular wall that can close the arteriole completely or can, by relaxing, dilate it several fold, thus having the capability of vastly altering blood flow in each tissue bed in response to the need of the tissue. The function of the capillaries is to exchange fluid, nutrients, electrolytes, hormones, and other substances between the blood and the interstitial fluid. To serve this role, the capillary walls are very thin and have numerous minute capillary pores permeable to water and other small molecular substances. The venules collect blood from the capillaries, and they gradually coalesce into progressively larger veins. The veins function as conduits for transport of blood from the venules back to the heart; equally important, they serve as a major reservoir of extra blood. Because the pressure in the venous system is very low, the venous walls are thin. Even so, they are muscular enough to contract or expand and thereby act as a controllable reservoir for the extra blood, either a small or a large amount, depending on the needs of the circulation.

Cross-Sectional Areas and Velocities of Blood Flow

If all the *systemic vessels* of each type were put side by side, their approximate total cross-sectional areas for the average human being would exceed those of non-systemic. Note particularly the much larger cross-sectional areas of the veins than of the arteries, averaging about four times those of the corresponding arteries. This explains the large storage of blood in the venous system in comparison with the arterial system. Because the same volume of blood must flow through each segment of the circulation each minute, the velocity of blood flow is inversely proportional to vascular cross-sectional area. Thus, under resting conditions, the velocity averages about 33 cm/sec in the aorta but only 1/1000 as rapidly in the capillaries, about 0.3 mm/sec. However, because the capillaries have a typical length of only 0.3 to 1 millimeter, the blood remains in the capillaries for only 1 to 3 seconds. This short time is surprising because all diffusion of nutrient food substances and electrolytes that occurs through the capillary walls must do so in this exceedingly short time.

1.6 Interrelationships among Pressure, Flow, and Resistance

Blood flow through a blood vessel is determined by two factors:

(1) *Pressure difference* of the blood between the two ends of the vessel, also sometimes called "*pressure gradient*" along the vessel, which is the force that pushes the blood through the vessel, and

(2) *The impediment to blood flow* through the vessel, which is called *vascular resistance.*

Considering a blood vessel segment located anywhere in the circulatory system, P_1 represents the pressure at the origin of the vessel; and at the other end, the pressure is P_2. Resistance occurs as a result of friction between the flowing blood and the intravascular endothelium all along the inside of the vessel. The flow through the vessel can be calculated by the following formula, which is called *Ohm's law*:

$$F= \Delta P/R \ (37)$$

Where, F is blood flow, DP is the pressure difference (P_1 - P_2) between the two ends of the vessel, and R is the resistance. This formula states, in effect, that *the blood flow is directly proportional to the pressure difference* but inversely proportional to the resistance. Note that it is the *difference* in pressure between the two ends of the vessel, not the absolute pressure in the vessel that determines rate of flow. For instance, if the pressure at both ends of a vessel is 100 mm Hg and yet no difference exists between the two ends, there will be no flow despite the presence of 100 mm Hg pressure. Ohm's law expresses the most important of all the relations that the reader needs to understand to comprehend the hemodynamics of the circulation. Because of the extreme importance of this formula, the reader should also become familiar with its other algebraic forms:

$$\Delta P=F \times R, \ R=\Delta P/F \ (38)$$

Blood Flow

Blood flow means simply the quantity of blood that passes a given point in the circulation in a given period of time. Ordinarily, blood flow is expressed in *milliliters per minute* or *liters per minute,* but it can be expressed in milliliters per second or in any other unit of flow. The overall blood flow in the total circulation of an adult person at rest is about 5000 ml / min. This is called the *cardiac output* because it is the amount of blood pumped into the aorta by the heart each minute.

Types of flow:

***a) Laminar Flow of Blood in Vessels*.**

When blood flows at a steady rate through a long, smooth blood vessel, it flows in *streamlines*, with each layer of blood remaining the same distance from the vessel wall. Also, the central most portion of the blood stays in the center of the vessel. This type of flow is called *laminar flow* or *streamline flow*, and it is the opposite of *turbulent flow*, which is blood flowing in all directions in the vessel and continually mixing within the vessel, as discussed subsequently.

Parabolic Velocity Profile During Laminar Flow:

When laminar flow occurs, the velocity of flow in the center of the vessel is far greater than that toward the outer edges. A vessel containing, for instance two fluids can demonstrate this. Considering, the one at the left colored by a dye and the one at the right a clear fluid, but there is no flow in the vessel. When the fluids are made to flow, a *parabolic interface* develops between them, the portion of fluid adjacent to the vessel wall has hardly moved, the portion slightly away from the wall has moved a small distance, and the portion in the center of the vessel has moved a long distance. This effect is called the "***parabolic profile for velocity of blood flow***."

The cause of the parabolic profile is the following: The fluid molecules touching the wall barely move because of adherence to the vessel wall. The next layer of molecules slips over these, the third layer over the second, the fourth layer over the third, and so forth. Therefore, the fluid in the middle of the vessel can move rapidly because many layers of slipping molecules exist between the middle of the vessel and the vessel wall; thus, each layer toward the center flows progressively more rapidly than the outer layers.

***b) Turbulent Flow of Blood Under Conditions*.**

When the rate of blood flow becomes too great, when it passes by an obstruction in a vessel, when it makes a sharp turn, or when it passes over a rough surface, the flow may then become *turbulent*, or disorderly, rather than streamline. Turbulent flow means that the blood flows crosswise in the vessel as well as along the vessel, usually forming whorls in the blood called *eddy currents*. These are similar to the whirlpools that one frequently sees in a rapidly flowing river at a point of obstruction. When eddy currents are present, the blood flows with much greater resistance than when the flow is streamline because eddies add tremendously to the overall friction of flow in

the vessel. The tendency for turbulent flow increases in direct proportion to the velocity of blood flow, the diameter of the blood vessel, and the density of the blood, and is inversely proportional to the viscosity of the blood, in accordance with the following equation:

$$R_e = (\nu\, d\, \rho) / \eta \quad (39)$$

Where Re is *Reynolds' number, as aforementioned (axisymmetric flow, eq.25),* is the measure of the tendency for turbulence to occur, n is the mean velocity of blood flow (cm/s), d is the vessel diameter (cm), r is density, and h is the viscosity (poise).

The viscosity of blood is normally of about 1/30 poise, and the density is only slightly greater than 1. When Reynolds' number rises above 200 to 400, turbulent flow will occur at some branches of vessels but will die out along the smooth portions of the vessels. However, when Reynolds' number rises above approximately 2000, turbulence will usually occur even in a straight, smooth vessel. Reynolds' number for flow in the vascular system even normally rises to 200 to 400 in large arteries; as a result there is almost always some turbulence of flow at the branches of these vessels. In the proximal portions of the aorta and pulmonary artery, Reynolds' number can rise to several thousand during the rapid phase of ejection by the ventricles; this causes considerable turbulence in the proximal aorta and pulmonary artery where many conditions are appropriate for turbulence:

(1) high velocity of blood flow
(2) Pulsatile nature of the flow,
(3) Sudden change in vessel diameter, and
(4) Large vessel diameter

However, in small vessels, Reynolds' number is almost never high enough to cause turbulence.

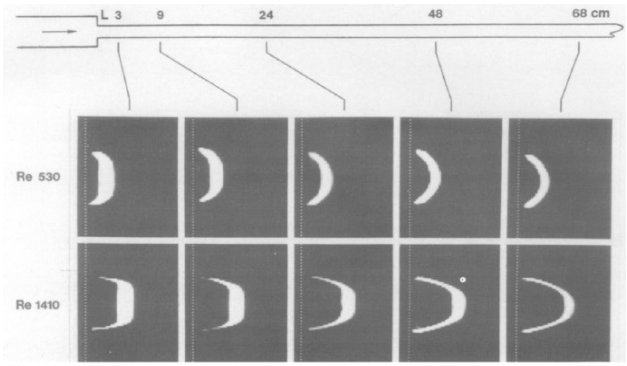

Fig.4 *MR fluid velocity profile images demonstrating the entrance effect. Images were acquired at selected distances, L (cm), from the entrance of a 16 mm i.d. tube at Re 530 and 1410[4]*

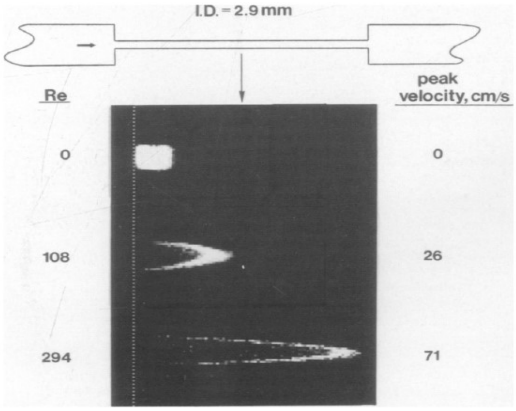

Fig.5 *Velocity profile images of flow through a tube of 2.9 mm inner diameter[4]*

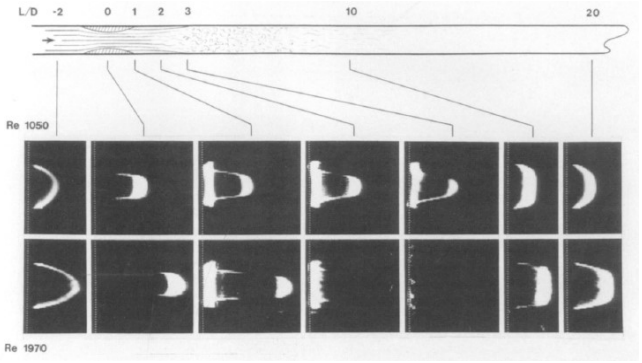

Fig.6 *Velocity profile images of flow through an axisymmetric constriction of 40% diameter reduction at Re 1050 and 1970. Axial distances, L, from the stenotic throat are measured in units of the tube diameter. D[4]*

c) Vortex

Vortex flow is a combination of laminar flow (while entering the vessel) and turbulent (while traverses along the stenosis), it can be any circular or rotary flow. Unexpectedly, not all vortices possess vorticity. Vorticity is a mathematical concept related to the amount of "circulation" or "rotation" in a fluid and expresses the circulation per unit area at a point in the flow field. It is a vector quantity, whose direction is along the axis of the swirl. The vorticity of a free vortex is zero everywhere except at the centre, whereas the vorticity of a forced vortex is non-zero. Vorticity is approximately conserved, therefore, flows starting with minimal vorticity, such as water in a basin, create vortices with minimal vorticity, such as the characteristic swirling and approximately free vortex structure when it drains. By contrast, fluids that initially have vorticity, form vortices with vorticity, exhibited by the much less pronounced low pressure region at the centre of this flow. The movement of a fluid is assumed to be vortical if the fluid moves around in a circle, or in a helix, or

if it tends to spin around some axis. Such motion can also be called solenoidal. Vorticity is defined as the curl of the fluid velocity :

$$\omega = \nabla \times u \quad (40)$$

d) Stagnant

Stagnant delineates a flow of a quite small velocity. The fluid behaves as static tissue, thus is depicted as stable flow. Stagnant flow occurs precisely after narrowing, near the vessel walls.

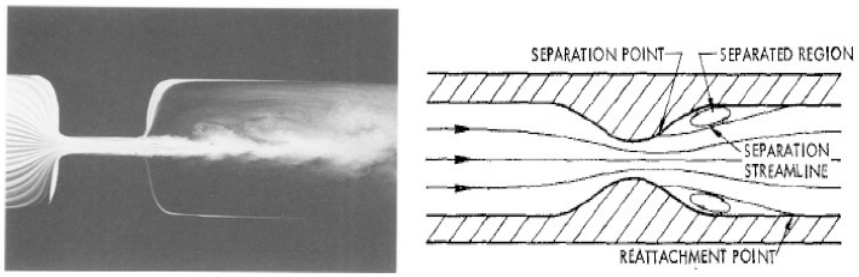

Fig.7 *Photograph of flow through a stenosis taken using the author's flow model (based on the Hele-Shaw theory). The laminar flow in the prestenotic segment remains laminated through the stenosis. At the outlet, a disturbed flow pattern is noted immediately distal to the stenosis. In the post-stenotic segment the energy loss (i.e. expansion loss) through eddies is obvious. [5]*

1.7 Flow parameters - effects in blood flow

Blood Pressure

Actually, *blood pressure means the force exerted by the blood against any unit area of the vessel wall.* Blood pressure almost always is measured in millimeters of mercury (mm Hg) because the mercury manometer has been used since antiquity as the standard reference for measuring pressure. A value of pressure in a vessel of 50 mm Hg, means that the force exerted is sufficient to push a column of mercury against gravity up to a level 50 mm high. If the pressure is 100 mm Hg, it will push the column of mercury up to 100 millimeters. Occasionally, pressure is measured in centimeters of water (cm H_2O). A pressure of 10 cm H_2O means a pressure sufficient to raise a column of water against gravity to a height of 10 centimeters. One millimeter of mercury pressure equals 1.36 cm water pressure because the specific gravity of mercury is 13.6 times that of water, and 1 centimeter is 10 times as great as 1 millimeter.

Resistance to Blood Flow

Resistance is the impediment to blood flow in a vessel, but it cannot be measured by any direct means. Instead, resistance must be calculated from measurements of blood flow and pressure difference between two points in the vessel. If the pressure difference between two points is 1 mm

Hg and the flow is 1 ml/sec, the resistance is 1 peripheral resistance unit, usually abbreviated *PRU*. Occasionally, a basic physical unit called the CGS (centimeters, grams and seconds) unit is used to express resistance. This unit is dyne seconds/centimeters. Resistance in these units can be calculated by the following formula:

$$R \text{ (in dyne sec) } /cm^5 = 1333 \text{ mmHg sec/ ml}$$

Conductance

Conductance is a measure of the blood flow through a vessel for a given pressure difference. This is generally expressed in terms of milliliters per second per millimeter of mercury pressure, but it can also be expressed in terms of liters per second per millimeter of mercury or in any other units of blood flow and pressure. It is evident that conductance is the exact reciprocal of resistance in accord with the following equation:

$$\text{Conductance} = 1/\text{ Resistance } (41)$$

Vascular Distensibility

A valuable characteristic of the vascular system is that all blood vessels are *distensible*. For instance: When the pressure in blood vessels is increased, this dilates the blood vessels and therefore decreases their resistance. The result is increased blood flow not only because of increased pressure but also because of decreased resistance, usually giving at least twice as much flow increase for each increase in pressure as one might expect. Vascular distensibility also plays other important roles in circulatory function. For example, the distensible nature of the arteries allows them to accommodate the pulsatile output of the heart and to average out the pressure pulsations. This provides smooth, continuous flow of blood through the very small blood vessels of the tissues. The most distensible by far of all the vessels are the veins. Even slight increases in venous pressure cause the veins to store 0.5 to 1.0 liter of extra blood. Therefore, the veins provide a *reservoir function* for storing large quantities of extra blood that can be called into use whenever required elsewhere in the circulation. Vascular distensibility normally is expressed as the fractional increase in volume for each millimeter of mercury rise in pressure, in accordance with the following formula: That is, if 1 mm Hg causes a vessel that originally contained 10 millimeters of blood to increase its volume by 1 milliliter, the distensibility would be 0.1 per mm Hg, or 10 per cent per mm Hg.

Difference in Distensibility of the Arteries and the Veins.

Anatomically, the walls of the arteries are far stronger than those of the veins. Consequently, the arteries, on average, are about eight times less distensible than the veins. That is, a given

increase in pressure causes about eight times as much increase in blood in a vein as in an artery of comparable size. In the pulmonary circulation, the pulmonary vein distensibilities are similar to those of the systemic circulation. But, the pulmonary arteries normally operate under pressures about one sixth of those in the systemic arterial system, and their distensibilities are correspondingly greater, about six times the distensibility of systemic arteries.

Vascular Compliance (or Vascular Capacitance)

Compliance and distensibility are quite different. A highly distensible vessel that has a slight volume may have far less compliance than a much less distensible vessel that has a large volume because compliance is equal to distensibility times the volume. The compliance of a systemic vein is about 24 times that of its corresponding artery because it is about 8 times as distensible and it has a volume about 3 times as great (8 * 3 = 24).

1.8 Interactions of flow parameters and effects in flow

Diameter of a Vessel – Conductance

Slight changes in the diameter of a vessel cause tremendous changes in the vessel's ability to conduct blood when the blood flow is streamlined. The results of an experiment for three vessels with relative diameters of 1, 2, and 4, having the same pressure difference of 100 mm Hg between the two ends of the vessels, indicate that: although the diameters of the vessels increase only fourfold, the respective flows are 1, 16, and 256 ml/mm, which is a 256-fold increase in flow. Thus, the conductance of the vessel increases in proportion to the fourth power of the diameter, in accordance with the following formula:

$$\text{Conductance} \propto \text{Diameter}^4 \quad (42)$$

Poiseuille's Law

Concerning the concentric rings of large vessel large, indicate that the velocity of flow in each ring is different from that in the adjacent rings because of laminar flow. Consequently, as the diameter increases there will be great increase in conductance in the large vessel contrary to the smaller vessels. Thus, the blood in the ring touching the wall of the vessel is barely flowing due to its adherence to the vascular endothelium. The next ring of blood toward the center of the vessel slips past the first ring and, therefore, flows more rapidly. The third, fourth, fifth, and sixth rings likewise flow at progressively increasing velocities. Thus, the blood that is near the wall of the

vessel flows extremely slowly, whereas that in the middle of the vessel flows extremely rapidly. In the small vessel, essentially all the blood is near the wall, so that the extremely rapidly flowing central stream of blood simply does not exist. By integrating the velocities of all the concentric rings of flowing blood and multiplying them by the areas of the rings, one can derive the following formula, known as Poiseuille's law:

$$F= (\pi \Delta P r^4) / (8\eta l) \quad (43)$$

Where, F is the rate of blood flow, DP is the pressure difference between the ends of the vessel, r is the radius of the vessel, l is length of the vessel, and h is viscosity of the blood.

In this equation the rate of blood flow is directly proportional to the fourth power of the radius of the vessel, which demonstrates once again that the diameter of a blood vessel (which is equal to twice the radius) plays by far the greatest role of all factors in determining the rate of blood flow through a vessel.

Effects of Pressure on Vascular Resistance and Tissue Blood Flow

From the discussion thus far, one might expect an increase in arterial pressure to cause a proportionate increase in blood flow through the various tissues of the body. However, the effect of pressure on blood flow is greater the one would expect. The reason for this is that an increase in arterial pressure not only increases the force that pushes blood through the vessels but also distends the vessels at the same time, which decreases vascular resistance. Thus, greater pressure increases the flow in both of these ways. Therefore, for most tissues, blood flow at 100 mm Hg arterial pressure is usually four to six times as great as blood flow at 50 mm Hg instead of two times as would be true if there were no effect of increasing pressure to increase vascular diameter. The large changes in blood flow that can be caused by either increased or decreased sympathetic nerve stimulation of the peripheral blood vessels. Thus, *inhibition of* sympathetic activity g*reatly dilates* the vessels and can increase the blood flow twofold or more. Conversely, very strong sympathetic stimulation *can constrict* the vessels so much that blood flow occasionally decreases to as low as zero for a few seconds despite high arterial pressure.

Volume-Pressure Curves of the Arterial and Venous Circulations

A convenient method for expressing the relation of pressure to volume in a vessel or in any portion of the circulation is to use the so-called volume-pressure curve. The volume-pressure curves of the normal systemic arterial system and venous system, show that when the arterial system of the average adult person (including all the large arteries, small arteries, and arterioles) is filled with about 700 ml of blood, the mean arterial pressure is 100 mm Hg, but when it is filled with only 400

ml of blood, the pressure falls to zero. In the entire systemic venous system, the volume normally ranges from 2000 to 3500 ml, and a change of several hundred millimeters in this volume is required to change the venous pressure only 3 to 5 mm Hg. This mainly explains why as much as one half liter of blood can be transfused into a healthy person in only a few minutes without greatly altering function of the circulation.

Arterial Pressure Pulsations

With each beat of the heart a new surge of blood fills the arteries. Were it not for distensibility of the arterial system, all of this new blood would have to flow through the peripheral blood vessels almost instantaneously, only during cardiac systole, and no flow would occur during diastole. However, normally the compliance of the arterial tree reduces the pressure pulsations to almost no pulsations by the time the blood reaches the capillaries; therefore, tissue blood flow is mainly continuous with very little pulsation. A typical record of the pressure pulsations at the root of the aorta is shown in figure 8a**.** In the healthy young adult, the pressure at the top of each pulse, called the systolic pressure, is about 120 mm Hg. At the lowest point of each pulse, called the diastolic pressure, it is about 80 mm Hg. The difference between these two pressures, about 40 mm Hg, is called the pulse pressure. Two major factors affect the pulse pressure: (1) the stroke volume output of the heart and (2) the compliance (total distensibility) of the arterial tree. A third, less important factor is the character of ejection from the heart during systole. In general, the greater the stroke volume output, the greater the amount of blood that must be accommodated in the arterial tree with each heartbeat, and, therefore, the greater the pressure rise and fall during systole and diastole, thus causing a greater pulse pressure. Conversely, the less the compliance of the arterial system, the greater the rise in pressure for a given stroke volume of blood pumped into the arteries. For instance as demonstrated by the middle top curves in figure 8b**,** the pulse pressure in old age sometimes rises to as much as twice normal, because the arteries have become hardened with arteriosclerosis and therefore are relatively noncompliant. In effect, then, pulse pressure is determined approximately by the ratio of stroke volume output to compliance of the arterial tree. Any condition of the circulation that affects either of these two factors also affects the pulse pressure.

Abnormal Pressure Pulse Contours

Some conditions of the circulation also can cause abnormal contours of the pressure pulse wave in addition to altering the pulse pressure. Especially distinctive among these are aortic stenosis, patent ductus arteriosus, and aortic regurgitation. In aortic stenosis, the diameter of the aortic valve opening is reduced significantly, and the aortic pressure pulse is decreased significantly because of diminished blood flow outward through the stenotic valve. In patent ductus arteriosus, one half or more of the blood pumped into the aorta by the left ventricle flows immediately backward through the wide-open ductus into the pulmonary artery and lung blood vessels, thus allowing the diastolic pressure to fall very low before the next heartbeat. In aortic regurgitation, the

aortic valve is absent or will not close completely. Therefore, after each heartbeat, the blood that has just been pumped into the aorta flows immediately backward into the left ventricle. As a result, the aortic pressure can fall all the way to zero between heartbeats. Also, there is no incisura in the aortic pulse contour because there is no aortic valve to close.

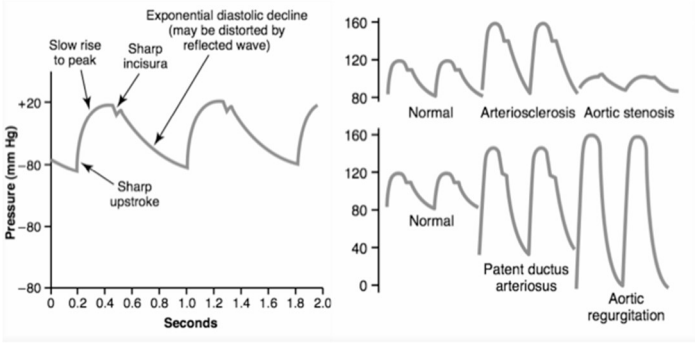

Fig.8 *Pressure pulse contour recorded from the ascending aorta and aortic pressure pulse contours in arteriosclerosis, aortic stenosis, patent ductus arteriosus, and aortic regurgitation* [6]

Transmission of Pressure Pulses to the Peripheral Arteries

When the heart ejects blood into the aorta during systole, at first only the proximal portion of the aorta becomes distended because the inertia of the blood prevents sudden blood movement all the way to the periphery. However, the rising pressure in the proximal aorta rapidly overcomes this inertia, and the wave front of distention spreads farther and farther along the aorta. This is called transmission of the pressure pulse in the arteries. The velocity of pressure pulse transmission in the normal aorta is 3 to 5 m/sec; in the large arterial branches, 7 to 10 m/sec; and in the small arteries, 15 to 35 m/sec. In general, the greater the compliance of each vascular segment, the slower the velocity, which explains the slow transmission in the aorta and the much faster transmission in the much less compliant small distal arteries. In the aorta, the velocity of transmission of the pressure pulse is 15 or more times the velocity of blood flow because the pressure pulse is simply a moving wave of pressure that involves little forward total movement of blood volume.

Effect of the Gravitational Factor on Arterial and Other Pressures

The gravitational factor also affects pressures in the peripheral arteries and capillaries, in addition to its effects in the veins. For instance, a standing person who has a mean arterial pressure of 100 mm Hg at the level of the heart has an arterial pressure in the feet of about 190 mm Hg. Therefore,

when one states that the arterial pressure is 100 mm Hg, this generally means that this is the pressure at the gravitational level of the heart but not necessarily elsewhere in the arterial vessels. [3]

CHAPTER 2

Nuclear Magnetic Resonance

2.1 General Concepts

Nuclear spin

Hydrogen nuclei (protons) have magnetic properties, called nuclear spin. They behave like tiny rotating magnets, represented by vectors. The sum of all the tiny magnetic fields of each spin is called net magnetization or macroscopic magnetization. Normally, the direction of these vectors is randomly distributed. Thus, the sum of all the spins gives a null net magnetization. Within a large external magnetic field (called B_o), nuclear spins align with the external field. Some of the spins align with the field (parallel) and some align against the field (anti-parallel). Main nuclei imaged in human MRI In clinical MRI, Hydrogen is the most frequently imaged nucleus due to its great abundance in biological tissues. Other nuclei such as $_{13}C$, $_{19}F$, $_{31}P$, $_{23}Na$ have a net nuclear spin and can be imaged in MRI. However, they are much less abundant than hydrogen in biological tissues and require a dedicated RF chain, tuned to their resonance frequency.

Precession, Larmor frequency

Spins wobble (or precess) about the axis of the Bo field so as to describe a cone. This is called precession. Spinning protons are like dreidles spinning about their axis. Precession corresponds to the gyration of the rotating axis of a spinning body about an intersecting axis. The resonance frequency, called Larmor frequency (ω_o) or precessional frequency, is proportional to the main magnetic field strength:

$$\omega_o = \gamma B_o \quad (44)$$

Net magnetization

The magnetic vector of spinning protons can be broken down into two orthogonal components: a longitudinal or z component, and a transverse component, lying on the xy plane. Precession corresponds to rotation of the transverse component about the longitudinal axis. Within the B_0 magnetic field, there are more spins aligned with the field (parallel - low energy state) than spins aligned against the field (anti-parallel - high energy state). Due to this slight excess of parallel spins, net magnetization (macroscopic magnetization) has a longitudinal component (along the z axis) aligned with B_o. As spins do not rotate in phase, the sum of all the

microscopic transverse magnetizations of each spin is a null transverse macroscopic magnetization.

Resonance

Exchange of energy between two systems at a specific frequency is called resonance. Magnetic resonance corresponds to the energetic interaction between spins and electromagnetic radiofrequency (RF). Only protons that spin with the same frequency as the electromagnetic RF pulse will respond to that RF pulse. There is a modification of spin equilibrium and absorption of electromagnetic energy by atomic nuclei, which is called excitation. When the system returns from this state of imbalance to equilibrium (relaxation), there is an emission of electromagnetic energy.

Excitation

Excitation modifies energy levels and spin phases. At the quantum level, a single proton jumps to a higher energy state (from parallel to anti-parallel). The consequence on the macroscopic net magnetization vector is a spiral movement down to the xy plane. In a rotating frame of reference, the net magnetization vector tips down during excitation. The flip angle is function of the strength and duration of the electromagnetic RF pulse. The net magnetization vector can be broken down into a longitudinal component (along the z axis, aligned with B_o), and a transverse component, lying on the xy plane. During excitation, longitudinal magnetization decreases and a transverse magnetization appears (except for a 180° flip angle). Longitudinal magnetization is due to a difference in the number of spins in parallel and anti-parallel state. Transverse magnetization is due to spins getting into phase coherence. If we consider an excitation with a 90° flip angle, when the RF transmitter is turned off: There is no longitudinal magnetization (equal proportion of parallel and anti-parallel spins). A transverse magnetization exists (all spins are in phase: complete phase coherence).

Relaxation

Return to equilibrium of net magnetization is called Relaxation. During relaxation, electromagnetic energy is retransmitted: this RF emission is called the NMR signal. Relaxation combines two different mechanisms:

Longitudinal relaxation corresponds to longitudinal magnetization recovery. Transverse relaxation corresponds to transverse magnetization decay. Longitudinal relaxation is due to energy exchange between the spins and surrounding lattice (spin-lattice relaxation), re-establishing thermal equilibrium. As spins precess from a high energy state back to a low energy state, RF energy is released back into the surrounding lattice. The recovery of longitudinal magnetization follows an exponential curve. The recovery rate is characterized by the tissue-specific time

constant T_1. After time T_1, longitudinal magnetization has returned to 63 % of its final value. With a 1.5 T field strength, T_1 values are about 200 to 3000 ms. T_1 values are longer at higher field strengths. Transverse relaxation results from spins getting out of phase. As spins move together their magnetic fields interact (spin-spin interaction), slightly modifying their precession rate. These interactions are temporary and random. Thus, spin-spin relaxation causes a cumulative loss in phase resulting in transverse magnetization decay. Transverse magnetization decay is described by an exponential curve, characterized by the time constant T_2. After time T_2, transverse magnetization has lost 63% of its original value. T_2 is tissue-specific and is always shorter than T_1. Transverse relaxation is faster than longitudinal relaxation. T_2 values are unrelated to field strength.

2.2 Instrumentation

Characteristics of the main magnet

The main characteristics of a magnet are: Type (superconducting or resistive electromagnets, permanent magnets). Strength of the field produced, measured in Tesla (T) and homogeneity. In current clinical practice, this varies from 0.2 to 3.0 T. In research, magnets with strengths of 7 T or even 11 T and over are used.

Gradients

They produce a linear variation in magnetic field intensity in a direction in space. This variation in magnetic field intensity is added to the main magnetic field, which is far more powerful. The variation is produced by pairs of coils, placed in each spatial direction. The direction of the magnetic field is not modified. By adding them to B_o, a linear variation is produced in the total magnetic field amplitude, in the direction to which they are applied. Their action is considered as homogeneous on a plane perpendicular to the direction of application. This modifies resonance frequency, in proportion to the intensity of the magnetic field to which they are submitted (in accordance with Larmor's equation: the stronger the field, the faster they precess). This variation in Larmor frequency also causes a variation and dispersion of spin phases.

Gradient characteristics

Gradient performances are linked to: their maximal amplitude (magnetic field variation in mT/m), which determines maximal spatial resolution (slice thickness and field of view) their slew rate, corresponding to their switching speed: high slew rates and low rise time are required to switch gradients quickly and allow ultra-fast imaging sequences such as echo planar (EPI) their linearity, which must be as perfect as possible within the scanning area.

Eddy currents

The rapid switching of the gradients induces currents in the conducting materials in the vicinity of the gradient coils (cryogenic envelope, electric wires, antennas, homogenization coils, etc.). These induced currents (Eddy current) will oppose the gradient fields and cause a decay in their profile. There are several methods to reduce the effects of these induced currents: Active gradient coil shielding, optimizing the electric current profile sent to the gradient coils while ascending and descending to offset the Eddy currents. Moreover, gradient switches produce Lorentz forces causing vibrations in the gradient coils and their supports. These vibrations are the main source of the characteristic MRI noise.

Radiofrequency system

The radiofrequency system comprises the set of components for transmitting and receiving the radiofrequency waves involved in exciting the nuclei, selecting slices, applying gradients and in signal acquisition. Coils are a vital component in the performance of the radiofrequency system. In transmission, the goal is to deliver uniform excitation throughout the scanned volume. On reception, the coils must be sensitive and have the best possible signal to noise ratio. An MR scanner generally contains a «whole body» coil, located in the cylinder of the machine, homogeneously covering the entire scan volume. The sensitive volume of surface coils, being placed in direct contact with the zone of interest, has less depth and is more heterogeneous. However, surface coils offer a better signal to noise ratio and imaging capacity with higher spatial resolution. The homogeneity and sensitive volume of surface coils can be improved by combining them into a phased array. They still have the advantage of a better signal to noise ratio, but at the cost of more complex signal processing. Quadrature RF coils (circularly polarized coils) consist of at least two coils that are oriented orthogonal to each over (and both are othogonal to B_o axis). They have a better signal to noise ratio than linear RF coils. Depending on the manufacturers and the type of coil, certain coils can be transmitters, receivers or both. The radiofrequency channel also comprises analog-digital converters and a spectrometer to receive and analyze the signal.

Optimizing the radiofrequency channel

Optimization of the radiofrequency channel is automated and carried out in several stages prior to an imaging sequence: the exact Larmor frequency is set, this being slightly modified by the patient's presence in the magnetic field, transmission power is adjusted according to the weight of the patient and the transmit coil, to obtain the desired flip angles, the receiver gain is adjusted to avoid signal saturation or conversely, weak amplification resulting in a deteriorated signal to noise ratio.

Faraday cage

As the resonance frequency of protons is very close to that of the radio waves used in radio broadcasting and the FM band, the MR device is placed in a Faraday cage to insulate it from external RF signals which could alter the signal. The copper Faraday cage completely encases the MR scanner. Openings through this cage need to be carefully designed to avoid canceling out the shielding effect.

Computer system

Coordination of the various stages of the examination and sequences, the spectrometer, image reconstruction and post-processing are all controlled by an internal computer system and by data acquisition and post-processing consoles. The main performance criteria for computer equipment for an MRI device are processing speed and ergonomics.

2.3 MR Signal

A magnet is a magnetic dipole that can be represented by a magnetic vector. A moving magnetic field induces a current in a loop of wire that can be recorded. MRI coils can be used for transmitting and/or receiving. As it is not possible to receive RF signal in the same axis as B_o, coils are only sensitive to variations of transverse magnetization vector. Quadrature RF coils (circularly polarized coils) consist of at least two coils that are oriented orthogonal to each over (and both are orthogonal to B_0 axis). They have a better signal to noise ratio than linear RF coils.

Signal recording

After a 90° RF pulse, net magnetization tips down, thus longitudinal magnetization has disappeared and transverse magnetization has appeared. Once the RF transmitter is turned off, relaxation happens: transverse magnetization decays, longitudinal magnetization recovers, protons re-radiate the absorbed energy. Coils can receive the signal in the transverse plane due to variations of transverse magnetization vector. This signal is oscillating at resonance frequency and signal envelope is a decay curve described as an exponential curve. In absence of any magnetic gradient, this signal is called Free Induction Decay (FID). FID signal decays faster than T_2 would predict and decreases exponentially at characteristic time constant T_2^*. T_2^* takes into account: tissue specific spin-spin relaxation (random interactions between spins) responsible for pure T_2 decay static inhomogeneities in magnetic fields which accelerate spins dephasing.

80° RF pulse

A 180° RF pulse can rephase spins and reverse static field inhomogeneities. After a 90° RF pulse, spins dephase and transverse magnetization decreases. Due to a 180° RF pulse, spins rephase and transverse magnetization reappears. The 180° RF pulse restores phase coherence: After the 90° RF pulse spins dephase (during a time defined as TE/2). After the 180° RF pulse, spins are back in phase at time TE after the 90° RF pulse. Afterwards, spins dephase again. At time TE (Echo Time), the signal is not as high as the initial transverse magnetization intensity. As the 180° RF pulse reverses dephasing due to static field inhomogeneities but not spin-spin relaxation, the signal loss is due to pure T_2 effect. The signal envelope joining maximums of echoes after 180° RF pulses is corresponding to the pure T_2 decay curve.

Spin echo, TR, TE

Spin Echo sequence is based on repetition of 90° and 180° RF pulses. Spin Echo sequence have two parameters: Echo Time (TE) is the time between the 90° RF pulse and MR signal sampling, corresponding to maximum of echo. The 180° RF pulse is applied at time TE/2. Repetition Time is the time between 2 excitations pulses (time between two 90° RF pulses). Each tissue has a specific proton density, T_1 and T_2 time. The NMR signal depends on these three factors. After time T_1, longitudinal magnetization has returned to 63 % of its final value. T_1 defines the recovery rate of longitudinal magnetization. After time T_2 , transverse magnetization has returned to 37 % of its initial value. T_2 defines the decay rate of transverse magnetization. On purpose of understanding the modification of tissue signals by TR and TE, let's consider two tissues A and B with different T_1 s. If TR is very long, even if tissue A has a longer T_1 than tissue B, the longitudinal magnetization of both tissues will recover completely before the next excitation. Thus, the transverse magnetization amplitude will be the same for both tissues after each excitation.

TR and T1-weighting

If TR is short and if tissue A has a longer T_1 than tissue B, the longitudinal magnetization of tissue A will recover less than the longitudinal magnetization of tissue B. Thus, the transverse magnetization amplitude of tissue B will be higher after the next excitation. By setting the TR to short values, tissue contrast will depend on differences in longitudinal magnetization recovery (T_1).

TE and T2-weighting

By setting the TR to long values, the T_1 effect on tissue contrast will be reduced. If TE is long enough, differences in transverse relaxation will alter tissue contrast (the T_2 effect) (If TE is too long, the signal will have disappeared).

Tissue contrast

To distinguish different tissues, we need to obtain contrast between them. Contrast is due to differences in the MR signal, which depend on the T_1, T_2 and proton density of the tissues and sequence parameters. The higher the signal is, the brighter it will appear on the MR image. Interpretation is based on analysis of tissue contrast, for given signal weightings (T_1, T_2, T_2* or PD). MR image could be compared to the representation of a painting with only 2 colors. For example, red would correspond to the T_1 effect, yellow to the T_2 effect, and pigment density to proton density. If we change the TR and TE, we can see better the red or yellow part of the painting better.

Signal weighting (T_1, T_2, PD) and sequences parameters: TR, TE

A long TR and short TE sequence is usually called Proton density –weighted. A short TR and short TE sequence is usually called T_1-weighted. A long TR and long TE sequence is usually called T_2-weighted. Nearly all MR image display tissue contrasts, that depend on proton density, T_1 and T_2 simultaneously PD, T_1 and T_2 weighting will vary with sequence parameters, and may differ between different tissues in the same image. The following table shows T_1 and T_2 relaxation times for various tissues at 1.5 T. For example: A tissue with a long T_1 and T_2 (like water) is dark in the T_1-weighted image and bright in the T_2 -weighted image. A tissue with a short T_1 and a long T_2 (like fat) is bright in the T_1-weighted image and gray in the T_2-weighted image. Gadolinium contrast agents reduce T_1 and T_2 times, resulting in an enhanced signal in the T_1-weighted image and a reduced signal in the T_2-weighted image.

	T_1 *(ms)*	T_2 *(ms)*
Water	3000	3000
Gray matter	810, 1,09-2,15 s	61-109
White matter	680, 0,76-1,08 s	61-100
Liver	420	45
Fat	240	85
Gadolinium	Reduces T1	Reduces T2
CSF	0,8-20 s	110-2000
Meninges	0,5-2,2 s	50-165
Muscle	0,95-1,82 s	20-67
Adipose	0,2-0,75 s	53-94

In clinical practice: TE is always shorter than TR

A short TR = value approximately equal to the average T_1 *value, usually lower than 500 ms*

A long TR = 3 times the short TR, usually greater than 1500 ms

A short TE is usually lower than 30 ms

A long TE = 3 times the short TE, usually greater than 90 ms . [7]

2.4 Spatial encoding

To localize the voxels (single volume elements containing protons), spatial information needs to be encoded into the NMR signal. Three steps are required: First of all, the desired slice must be selected, Then, spatial information is encoded along the rows, Finally, spatial information is encoded along the columns Decoding of spatial information, included in the NMR signal as modifications of frequency and phase, is performed by an inverse Fourier Transform.

Magnetic field gradients

Spatial encoding relies on successively applying magnetic field gradients. First of all, a slice selection gradient (GSS) is used to select the anatomical volume of interest. Within this volume, the position of each point will be encoded vertically and horizontally by applying a phase encoding gradient (GPE), and a frequency-encoding gradient (GFE). The different gradients used to perform spatial localization have identical properties but are applied at distinct moments and in different directions. Gradient equivalence in the three directions of space means that slices can be selected on any spatial plane.

Slice selection

The first step of spatial encoding consists in selecting the slice plane. Eventually, a magnetic field gradient, the Slice Selection Gradient (GSS), is applied perpendicular to the desired slice plane. This is added to B_0, and the protons present a resonance frequency variation proportionate to GSS (Larmor equation). An RF wave is simultaneously applied, with the same frequency as that of the protons in the desired slice plane. This causes a shift in the magnetization of only the protons on this plane. As none of the hydrogen nuclei located outside the slice plane are excited, they will not emit a signal. The RF wave associated with the slice selection gradient and the adapted resonance frequency is called the selective pulse. These protons located in the slice plane will again be stimulated by the magnetic field gradients to encode their position in horizontal and vertical directions. Selecting a slice plane and spatially encoding each voxel involves the use of magnetic field gradients. Magnetic field intensity varies regularly along the gradient application axis. Each gradient is characterized by its strength (greater or lesser field variation for the same unit of distance), direction and the moment and time of application. The slice selection gradient modifies the precession frequency of the protons such that an RF pulse with the same frequency will cause them to shift (resonance). The slice selection gradient is simultaneously applied to all the RF pulses. Through the intermediary of the slice selection gradient, RF pulse frequency corresponds to selectivity in space. RF pulse bandwidth and waveform determine slice thickness and profile.

Phase encoding

The second step in spatial encoding consists in applying a phase encoding gradient, which for instance can be applied in the vertical or horizontal direction. Supposing the application in the vertical direction: The phase encoding gradient (GPE) intervenes for a limited time period. While it is applied, it modifies the spin resonance frequencies, inducing dephasing, which persists after the gradient is interrupted. This results in all the protons precessing in the same frequency but in different phases. The protons in the same row, perpendicular to the gradient direction, will all have the same phase. This phase difference lasts until the signal is recorded. On receiving the signal, each row of protons will be slightly out of phase. This translates as their signals being more or less out of phase. To obtain an image, it is necessary to multiply the different dephased acquisitions, which are regularly incremented. For a spin echo sequence with «n» rows, we make «n» acquisitions each with a different phase encoding gradient. Each phase encoding step acts as a kind of sieve letting through regularly spaced horizontal signals. This filter is sensitive to the vertical spatial distribution of the signals in the slice plane. The greater the phase difference, the thinner and finer the filter. In the absence of phase encoding, the signal will come from the whole slice. This is why multiple phase encoding steps are needed to acquire enough data to reconstruct the image. By analyzing the signals obtained with hundreds of different profiles, corresponding to as many fine combs, an image can be reconstructed (not only composed of horizontal bands, but

of more complex contours). To carry out the different phase encoding steps, the gradient is applied with different, regularly incremented values. It is bipolar, that is to say gradients are used with positive and negative values that are symmetrical to 0. In terms of the « filter size » range, a bipolar gradient is equivalent to a gradient that is only positive, for instance, and of the same absolute variation amplitude. However this requires positive amplitudes that are twice as high (causing greater dephasing and a poorer quality signal).

Frequency encoding

The final step in spatial encoding consists in applying a frequency-encoding gradient, when the signal is received, in the last direction (horizontal in our example). This modifies the Larmor frequencies in the horizontal direction throughout the time it is applied. It thus creates proton columns, which all have an identical Larmor frequency. Frequency encoding can be interpreted in the same way, in the horizontal direction. When the frequency-encoding gradient is applied, the signal is digitized at regular intervals in time. Each signal sample corresponds to a given accumulation of the gradient effect on the whole splice signal: the longer the time, the longer the effect of the gradient on the spins, and the greater their phase modification. We see the same filter effect, sensitive to spatial distribution in the horizontal direction (the direction in which the gradient is applied). To obtain the equivalent of a bipolar effect, a frequency encoding gradient half-lobe is applied but in the opposite direction (dephasing lobe) prior to signal recording. All the signals from the same slice are recorded in k-space then processed to form an image of the slice plane. While frequency spatial encoding only takes a few milliseconds of signal reading, phase spatial encoding involves repeating the imaging sequence. In a classic spin echo sequence, a single phase encoding step is performed during each repetition time (TR). As TR values can be of up to 3 seconds, phase encoding is therefore much longer than frequency encoding.

3D spatial encoding

The particularities of 3D acquisitions are: excitation of a complete volume at each repetition (volume = «thick slice »), rather than one thin slice spatial encoding in 3D by adding phase encoding in the 3rd dimension in relation to the phase and frequency encodings used in 2D imaging multiplication of the number of repetitions of a factor equal to the number of « slices» (partitions) in the third dimension to fill all the 3D k-space reconstruction by 3D Fourier transform.

All these have consequences for: acquisition time: given the large amount of acquired data needed to fill the 3D k-space, either very short TR sequences (echo gradient type) are used, or faster k-space filling methods. The amount of signal: at each repetition, the signal comes from the whole volume, rather than a single slice. Therefore more signal is recorded, with fewer noise. The partitions can be finer than the classic 2D slices, because the signal to noise ratio is better compared to a slice of the same thickness acquired in 2D. Spatial resolution: the entire volume of interest is

explored, with no interval between partitions, allowing fine section and multiplanar reconstructions. Artifacts: because of the two phase encodings, wraparound and truncation artifacts can be seen in two different directions.

Duration of a 3D imaging sequence

$$\text{Duration} = TR \cdot NPy \cdot NPz \cdot Nex \quad (45)$$

Where,

TR = Repetition time

NPy = Number of encoding steps in the y-axis

NPz= Number of encoding steps in the z-axis

Nex= Number of excitations

Image formation

The readout MR signal is a mix of RF waves with different amplitudes, frequencies and phases, containing spatial information. This signal is digitized and raw data are written into a data matrix called K-space. K-space data are equivalent to a Fourier plane. To go from a k-space data to an image requires using a 2D inverse Fourier Transform.

2.5 Sequences

Characteristics

The architecture of a sequence consists of the essential components on one hand, and the various options, on the other. The building blocks of the sequence are radiofrequency pulses and gradients. The essential components for any imaging sequence are: An RF excitation pulse, required for the phenomenon of magnetic resonance, gradients for spatial encoding (2D or 3D), whose arrangement will determine how the k-space is filled, asignal reading, combining one or a number of echo types (spin echo, gradient echo, Hahn echo, stimulated echo). Determining the type of contrast (the varying influence of relaxation times T_1, T_2 and T_2*). The options consist of other radiofrequency pulses, gradients or variable reconstruction methods to: Either modify the contrast (preparing magnetization by inversion-recovery, fat saturation, magnetization transfer) or accelerate the sequence (partial Fourier plane filling, parallel acquisition, fast magnetization

restoration) or to reduce artifacts (flow compensation, synchronisation, presaturation bands). Finally, the user must choose the sequence parameters (TR, TE, flip angle, turbo factor, field of view matrix) to find the best compromise between contrast, spatial resolution and speed.

Classification

There are two main sequence families, depending on the type of echo recorded: spin echo sequences, characterized by the presence of a 180° rephasing RF pulse, gradient echo sequences. Numerous variations have been developed within each of these families, mainly to increase acquisition speed: Fast spin echo sequences, Single shot FSE and Haste Gradient echo sequences with spoiling of residual transverse magnetization (spoiled gradient echo and ultrafast gradient echo), a group of gradient echo sequences with steady state residual transverse magnetization (Steady state gradient echo) and its derivatives (Contrast enhanced steady state gradient echo) and with balanced gradients (Balanced steady state gradient echo), echoplanar (EPI). Some sequences are hybrid, mixing spin echo and gradient echo (GRASE, SE-EPI). In addition, Magnetic resonance angiography sequences (FBI, contrast-enhanced MRA, TOF, PC) perfusion imaging, diffusion imaging (DW) and MR spectroscopy.

Gradient echo

The gradient echo sequence differs from the spin echo sequence in regard to: the flip angle usually below 90° and the absence of a 180° RF rephasing pulse. As there is no 180° RF pulse, a bipolar readout gradient (which is the same as the frequency-encoding gradient) is required to create an echo. The gradient echo formation results from applying a dephasing gradient before the frequency-encoding or readout gradient. The goal of this dephasing gradient is to obtain an echo when the readout gradient is applied and the data are acquired. The dephasing stage of the readout gradient is in the inverse sign of the readout gradient during data acquisition. Moreover, its dephasing effect is designed so that it corresponds to half of the dephasing effect of the readout gradient during data acquisition. Consequently, during data acquisition, the readout gradient will rephase the spins in the first half of the readout (by reversing the dephasing effect of the dephasing lobe), and the spins will dephase in the second half (due to the dephasing effect of the readout gradient). The time during which the peak signal is obtained is called Echo Time (TE).

A flip angle lower than 90° (partial flip angle) decreases the amount of magnetization tipped into the transverse plane. The consequence of a low-flip angle excitation is a faster recovery of longitudinal magnetization that allows shorter TR/TE and decreases scan time. The advantages of low-flip angle excitations and gradient echo techniques are faster acquisitions, new contrasts between tissues and a stronger MR signal in case of short TR. The flip angle determines the fraction

of magnetization tipped in the transverse plane (which will produce the NMR signal) and the quantity of magnetization left on the longitudinal axis. If the flip angle decreases, the residual longitudinal magnetization will be higher and the recovery of magnetization for a given T_1 and TR will be more complete. On the other hand, the result of a lower flip angle excitation is a lower tipped magnetization. The actual decay of the transverse magnetization is due to several factors: spin-spin tissue-specific relaxation (T_2) Which is random, B_0 field inhomogeneities and magnetic susceptibility, which are static.

As GE techniques use a single RF pulse and no 180° rephasing pulse, the relaxation due to fixed causes is not reversed and the loss of signal results from T_2* effects (pure T_2 + static field inhomogeneities). The signal obtained is thus T_2*-weighted rather than T_2-weighted. These sequences are thus more sensitive to magnetic susceptibility artifacts than are spin echo sequences.

Steady state

In gradient echo, TR reduction may cause permanent residual transverse magnetization in TR below T_2: the transverse magnetization will not have completely disappeared at the onset of the following repetition and will also be submitted to the flip caused by the excitation pulse. Two main classes of gradient echo sequence can be distinguished, depending on how residual transverse magnetization is managed: gradient echo sequences with spoiled residual transverse magnetization, steady state gradient echo sequences that conserve residual transverse magnetization and therefore participate in the signal.

2.6 Image quality and artifacts

MRI image quality

The quality of an MR image depends on several factors: Spatial resolution and image contrast, Signal to noise ratio (and contrast to noise ratio), Artifacts. An MR exploration is a compromise between scan time and image quality. An MR exploration protocol and its sequence parameters will have to be optimized in function of the organs and pathology.

Signal and Noise

Noise is like interferences, which present as an irregular granular pattern. This random variation in signal intensity degrades image information. The main source of noise in the image is the patient's body (RF emission due to thermal motion). The whole measurement chain of the MR scanner (coils, electronics. etc) also contributes to the noise. This noise corrupts the signal coming

from the transverse magnetization variations of the intentionally excited spins (on the selected slice plane). The signal to noise ratio (SNR) is equal to the ratio of the average signal intensity over the standard deviation of the noise. The signal to noise ratio depends both on some factors that are beyond the operator's control (the MR scanner specifications and pulse sequence design) and on factors that the user can change: Fixed factors: static field intensity, pulse sequence design, tissue characteristics factors under the operator's control, RF coil to be used, Sequence parameters: voxel size (limiting spatial resolution), number of averagings, receiver bandwidth.

In literature as reported above, SNR is used for quality assurance and validation of different MRA techniques:

In a report SNR is assessed, by taking the signal (S) to be the mean pixel intensity value in a region of interest (ROI), and the noise to be the standard deviation (σ) in pixel intensity one or multiple ROIs in background air (free of ghosting artifacts), and is calculated using SNR = 0.655·S/σ. The 0.655 factor is due to the Rayleigh distribution of the background noise in a magnitude image (which arises because noise variations, which can be negative and positive, are all made positive which artificially reduces σ a bit). If the image homogeneity is not considered to be good, then the SNR may be derived more accurately using the following (NEMA) method. Two images should be acquired by consecutive scans with identical receiver and transmitter settings. The images should then be ssubtracted one from the other, to generate a third pixel-by-pixel difference image. The only difference between the two original images should be due to noise, provided the image has not suffered from ghosting or any other instability, acquiring two original images, and a subtracted image. Using either of the original images the signal (S) is again defined as the mean pixel intensity value in a ROI. The noise is the standard deviation (σ) in the same ROI on the subtracted image. The signal to noise ratio is determined using SNR = √2·S/σ, where the factor of √2 arises due to the fact that the standard deviation is derived from the subtraction image and not from the original image.

In their study Firbank et al. [8], on purpose of proposing guidelines for quality assurance in MRI they measured SNR and image uniformity. Thus, they report after all that SNR is temperature dependent, affected by the resistive loading of the receiver coil. The resistive loading is dependent on the conductance of the fluid within the annulus, which falls with increasing temperature. Variation of SNR with temperature was then calculated: SNR= 94.1-0.766 T. The SNR is sensitive to most changes in system parameters. Change I slice thickness will affect the SNR, since the measured signal is proportional to the slice thickness. Errors in slice position will either be due to non-uniformity in the gradient field or main magnetic field. These errors should also cause distortion in the SNR phantom. Changes in the pixel resolution should also lead to variation in SNR and distortion. In as similar previous study Firbank et al. [9], they compared a single acquisition method, which estimates the noise from background pixels, with a dual acquisition method which estimates the noise from the subtraction of two sequentially acquired images, methods aforementioned. The dual acquisition method is more exact, but is slower to perform and requires image manipulation.

A comparison between the two methods gave a good correlation, and a regression equation of $SNR_{single} = 1.1 + 0.94\ SNR_{dual}$. The single acquisition method is therefore appropriate for use in a quality assurance programme, since it is quicker and simpler to perform and is a good indicator of the more exact measure.

Goerner et al [10], assess in their study five different methods of signal-to-noise ratio (SNR) measurement for partially parallel imaging (PPI) acquisitions. Measurements were performed on a spherical phantom and three volunteers using a multichannel head coil a clinical 3T MRI system to produce echo planar, fast spin echo, gradient echo, and balanced steady state free precession image acquisitions. Two different PPI acquisitions, generalized autocalibrating partially parallel acquisition algorithm and modified sensitivity encoding with acceleration factors (R) of 2–4, were evaluated and compared to nonaccelerated acquisitions. Five standard SNR measurement techniques were investigated and Bland–Altman analysis was used to determine agreement between the various SNR methods. The estimated g-factor values, associated with each method of SNR calculation and PPI reconstruction method, were also subjected to assessments that considered the effects on SNR due to reconstruction method; phase encoding direction, and R-value. Results showed that only two SNR measurement methods produced g-factors in agreement with theoretical expectations ($g \geq 1$). Bland–Altman tests demonstrated that these two methods also gave the most similar results relative to the other three measurements. R-value was the only factor of the three considered that showed significant influence on SNR changes. Thus they concluded that non-signal methods used in SNR evaluation do not produce results consistent with expectations in the investigated PPI protocols. Two of the methods studied provided the most accurate and useful results. Of these two methods, it was recommended, when evaluating PPI protocols, the image subtraction method be used for SNR calculations due to its relative accuracy and ease of implementation.

In another study Mascaro et al. [11], report the preliminary results of a multicenter trial aimed at defining methods, reference values and frequency of measurements for an MR quality assurance program. In particular, they stress the definition of two attention levels (investigation and intervention) for image uniformity and signal-to-noise ratio (SNR) by means of short- and long-term measurements. The short-term protocol results allowed absolute comparison of system performance. Uniformity and SNR were significantly different among centers ($p < 0.05$), also in the statistical comparison of two MR units of the same model. Overall, three 1.5 T systems provided similar SNR values, while the results obtained for the 1 T system were markedly lower (51% of the maximum). This result was explained by the dependence of the analytical expression of SNR on the magnetic field. The other 1.5 T system performed more poorly than the others operating at the same magnetic field. This difference was explained by the specific characteristics of the coil and by technological aging. Because of the small sample size (5 units), the maximum variation coefficients (3% for the first echo and 3.5% for the second one) were assumed as a reference value for the both parameters (SNR and uniformity). These values were used for the long-term analysis: at every measurement the evaluated parameter was statistically compared with

the result of the previous month. They proposed to set an investigation level at $p = 0.05$: when the newly measured parameter differs from the previous value ($p < 0.05$), so as to investigate if this was due to a normal long-term variation or to a system fault. The intervention level was then defined as the 95% prediction interval of the evaluated parameter regression vs time. Measurements that did not fall within the prediction interval will not be used for future statistics.

RF coil

The smaller the sensitive volume of a coil, the lower the noise from the adjacent structures of the selected slice plane which it can detect, and the better the signal to noise ratio will be. A local coil, or better, a surface coil have a higher signal to noise ratio than a body coil.

2.7 Parameters of sequences

Voxel volume

The signal comes from the excited protons on the selected slice plane. The number of spins in parallel state in excess is proportional to the static magnetic field intensity. The larger the field intensity is, the higher the excess number of spins in parallel state (available to make the MR signal) will be. Thus, the signal intensity varies almost linearly with the main field intensity. Assuming a uniform proton density, the number of excited spins is proportional to the voxel size and so is the signal intensity. The signal goes up linearly with the voxel size.

Number of excitations

When the number of excitations (or averagings) for the same slice increases: The signal is identical for each measure, the noise is random and is not the same for each measure. Therefore, the signal sum goes up linearly with the number of excitations but the noise only goes up with the square root of the number of excitations. In other words, the average signal remains constant, but the average noise goes down with the square root of the number of excitations. The signal to noise ratio goes up with the square root of the number of excitations.

Receiver bandwidth

Given a voxel size and static field strength, the number of excited spins is defined and so is the amount of MR signal. The readout of the MR signal can take more or less time, depending on the receiver bandwidth. The relation between the receiver bandwidth and the strength of the readout gradient is such that: a broad bandwidth corresponds to a fast sampling of the MR signal and a high-intensity readout gradient, a narrow bandwidth corresponds to a slow sampling of the

MR signal and a low-intensity readout gradient. Background noise has a constant intensity at all frequencies (white noise). Therefore, the larger the receiver bandwidth is, the more noise is recorded (and the higher is the readout gradient intensity and the faster the MR signal is sampled).

Artifacts

Artifacts appear in MRI for a variety of reasons. Potential sources of artifacts include nonideal hardware characteristics, intrinsic tissue properties and biological behavior, assumptions underlying the data acquisition and image reconstruction process, and poor choice of scanning parameters. Careful study design and scanning protocols can prevent certain artifacts from occurring, but some are unavoidable. Numerous correction methods have been developed to mitigate the corruptive effects of artifacts and improve image diagnostic quality. These methods include special pulse sequence designs, improved scanning procedures and equipment, and advanced postprocessing algorithms. Recognizing artifacts and understanding their underlying causes are important when interpreting images and choosing a correction approach. Understanding the causes of MRI artifacts will lead to more accurate image interpretation, better scanning protocol designs and proper selection of a correction method. MRI arifacts occur because one or more of the assumptions underlying the imaging principles have been violated. Artifact correction methods usually involve one or more of the following:

- Hardware calibration

- Scanning parameter optimization

- Special pulse sequence design

- Signal and image postprocessing

Artifact correction is an active area of research today, and will continue to be in the future as advances in MRI technology reveal new image information and new kinds of artifacts. Smith et al. [12]

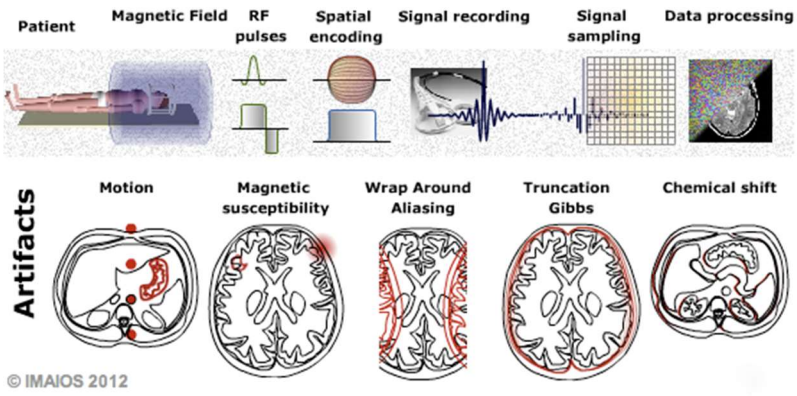

Fig 9. *'Overall, MRI is a compromise between: Spatial resolution: limited by the voxel size which is determined by the matrix size, the field of view and slice thickness, Signal to noise ratio: depending on the voxel size, the number of averagings and the receiver bandwidth, Total scan time Which also modify the available sequence parameters (TE) and the artifacts.'*

2.8 MRA

MR Angiography

Flow, like any movement in MRI, is at the origin of spatial encoding perturbations and artifacts. This MRI sensitivity has been harnessed to develop vascular imaging using the physical modifications linked to flow (non-contrast MRA): time-of-flight, phase contrast, fresh blood imaging (FBI). Contrast-enhanced MR Angiography exploits the relaxivity properties of contrast agents to visualize vascular structures. Whatever the principle employed, these sequences implement a strategy to suppress the background signal represented by the stationary tissue. All these techniques can be adapted to 3D, and later post-processed (reconstruction by maximum intensity projection MIP). They can all benefit from the progress brought by parallel imaging, in terms of speed and enhanced image quality.

Flow phenomena in MRI

Endogenous vascular contrast can be obtained by 3 different techniques: either by using modifications linked to blood volume displacement, which will not be subjected to all the radiofrequency pulses, unlike the stationary tissue: time-of-flight phenomenon or by exploiting the transverse magnetization dephasing of moving spins subjected to a gradient: phase contrast or by optimizing spatial encoding and the duration of an ultrafast spin echo sequence, synchronized to

ECG: FBI. In all three techniques, the signal and resulting image are produced by physiological flow. Depending on the underlying physical phenomenon, these methods will be more or less sensitive to certain flow velocities or types of flow. They will often come into difficulty, namely when faced with complex or turbulent flows. In the case of contrast-enhanced angiography, it is more a question of morphological imagery: the distribution of the contrast agent in the vascular sector is imaged. The main criterion is thus to acquire data at the right moment, during the passage of the contrast agent bolus. Except for FBI, these MR angiography techniques use sequences derived from T1-weighted echo gradient sequences.

Vessel signals in spin echo sequences

Vessels generally appear as hyposignals in spin echo sequences due to the outflow effect. The spins in the blood are excited during the slice selection pulse. At time TE/2 some of these spins move out of the slice and so are not subjected to the 180° pulse: therefore there is a reduction in the signal from their initial region. This signal is even lower when blood velocity is high. There will be a complete vascular signal void if all the spins have moved out of the slice at time TE/2.

Flow compensation

In all classic and angiographic imaging sequences, aside from phase contrast MRA, phase is designed to relate to spatial information only (determined by phase encoding). A bipolar gradient, whose positive and negative lobes are of equal importance, will have no effect on the phase of stationary spins. On the other hand, if a spin is moving on the gradient axis, its gradient effect will be subject to its position. Consequently, moving spins will be poorly located and a motion artifact will be seen in vascular structures and moving fluids. To correct this artifact, a third lobe is added to the slice selection and readout gradients. The gradient lobe surface ratio is 1: -2: 1, which will not induce dephasing in the stationary spins and avoids dephasing in flows at constant velocity. To compensate the dephasing of flows at variable velocity (non-null acceleration), gradient lobes again have to be added on, resulting in longer TE and a reduced signal. Flow compensation gradients can be used in any sequence requiring the suppression of these artifacts, except for phase contrast MRA.

Time-of-flight MR angiography

In time-of-flight MR angiography, the flow compensated gradient-echo sequences will be optimized to favor the vascular signal over that of the surrounding tissues by: saturating the stationary tissue signal with very short TR: thus the longitudinal magnetization of these tissues does not have time to regrow and their signal weakens favoring the inflow effect: because the blood flowing into explored zone has not been saturated, its longitudinal magnetization is maximal.

The signal from the blood flow is thus stronger than that of the saturated tissues. The strength of the vascular signal depends on: flow velocity and type, the length and orientation of the explored vessel (the vascular signal will be better if the slice is perpendicular to the axis of the vessel), the sequence parameters: TR, flip angle, TE, slice thickness.

Limitations

The main limitations of time-of-flight MRA are: Signal loss linked to spin dephasing when flows are complex or turbulent (stenosis), when flows are too slow or oriented parallel to the slice plane, Poor signal suppression of the stationary tissues with short T_1 relaxation time (fat, atheroma, hematoma, thrombus).

Optimization

Vascular contrast can be improved by suppressing the static tissue signal, by means of: a magnetization transfer preparation pulse, selective excitation of the water or fat saturation. The direction of the flows to visualize can be selected by placing a presaturation band upstream of the volume of interest, to suppress unwanted arterial or venous flows.

2D TOF imaging

In 2D acquisition, time-of-flight imaging uses a set of fine slices that are stacked up to reconstruct a pseudo-volume. The advantage of fine slices is better sensitivity to slow flows (which do not remain in the slice for long and will therefore not be saturated), with the possibility of using high flip angles (giving better stationary tissue saturation and an increased vascular signal). But the drawback with 2D acquisition is poor spatial resolution along the axis of the slice stack.

3D TOF imaging

Contrary to 2D TOF, 3D TOF volumetric imaging gives good spatial resolution in the 3 spatial directions, with a better signal-to-noise ratio. Each repetition excites the volume, producing a progressive saturation of the flows, even more so when they are slow. The slowest flows may even disappear entirely. Flow saturation can be reduced as it passes through the explored volume by: dividing 3D acquisition into «slabs», using a variable excitation angle that is weaker as the flow enters the volume and stronger as it leaves the volume thus compensating relaxation of short T_1 tissues.

Phase-contrast MRA

Phase contrast angiography relies on dephasing the moving spins submitted to a bipolar gradient. For a bipolar gradient of a given intensity and time, the moving spins will dephase in proportion to their velocity. Similar to spatial encoding in the phase direction, the possible phase values range from $-\pi$ to $+\pi$. Beyond this range of values, aliasing occurs, causing poor velocity encoding. The encoding gradient characteristics are thus defined in order to encode flows within a certain velocity range from $-V_{enc}$ to $+V_{enc}$ to be determined by the user. Any velocity outside this range will be poorly encoded (similar to what happens in pulsed and color Doppler with PRF).

(PC) Phase contrast sequences are the basis of MRA techniques utilizing the change in the phase shifts of the flowing protons in the region of interest to create an image. Spins that are moving along the direction of a magnetic field gradient receive a phase shift proportional to their velocity. In a phase contrast sequence two data sets with a different amount of flow sensitivity are acquired. This is usually accomplished by applying gradient pairs, which sequentially dephase and then rephase spins during the sequence. Both 2D and 3D acquisition techniques can be applied with phase contrast MRA. The first data set is acquired with a flow compensated sequence, i.e. without flow sensitivity. The second data set is acquired with a flow sensitive sequence. The amount of flow sensitivity is controlled by the strength of the bipolar gradient pulse pair, which is incorporated into the sequence. Stationary tissue undergoes no effective phase change after the application of the two gradients. Caused by the different spatial localization of flowing blood to stationary tissue, it experiences a different size of the second bipolar gradient compared to the first. The result is a phase shift. The raw data from the two data sets are subtracted. By comparing the phase of signals from each location in the two sequences the exact amount of motion induced phase change can be determined to have a map where pixel brightness is proportional to spatial velocity. Phase contrast images represent the signal intensity of the velocity of spins at each point within the field of view. Regions that are stationary remain black while moving regions are represented as grey to white. The phase shift is proportional to the spin's velocity, and this allows the quantitative assessment of flow velocities. The difference MRI signal has a maximum value for opposite directions. This velocity is typically referred to as V_{enc}, and depends on the pulse amplitude and distance between the gradient pulse pair. For velocities larger than V_{enc} the difference signal is decreased constantly until it gets zero. Therefore, in a phase contrast angiography it is important to correctly set the V_{enc} of the sequence to the maximum flow velocity, which is expected during the measurement. High V_{enc} factors of the PC angiogram (more than 40 cm/sec) will selectively image the arteries (PCA - arteriography), whereas a V_{enc} factor of 20 cm/sec will perform the veins and sinuses (PCV or MRV-venography).

Bipolar gradient and the dephasing of moving spins

In a bipolar gradient, the dephasing of the spins moving along the gradient axis is proportionate to their velocity, gradient intensity and the square of the application time of a

gradient lobe: Intuitively: the further the spin moves (velocity * time), the more it will be submitted to high gradient effect variation. The more intense the gradient and the longer it is applied (intensity * time), the greater the effect on phase.

2D PCA imaging

Phase contrast imaging from a thick 2D slice can be compared to projection angiography. Sequence adjustments are needed to suppress the stationary tissue signal and to calculate the phase difference. The advantage of 2D single-slice acquisition is that it is fast, which is useful for testing different encoding speeds. This technique can also be employed in vascular flow cine imaging, using pulse or ECG synchronization. For the quantitative study of flows, the slice plane must be perpendicular to flow direction. Thus a flow velocity curve can be obtained as a function of time, which, when coupled with morphologic data (vascular section) will calculate the flow rate.

3D PCA imaging

In phase contrast volumetric acquisition, each partition is encoded in 3 directions. To reduce acquisition time, the number of phase encoding steps must be reduced. The images are then reconstructed in maximum intensity projection (MIP). The finesse of the acquisition volume partitions gives better quality images than in 2D single-slice acquisition. Moreover, this technique is more sensitive than time-of-flight for slow flows (which are saturated in time-of-flight). Its applications namely concern 3D cerebral venous imaging (thrombosis of cerebral veins, fistula) and may also be used after injection of a contrast agent (particularly in cases of defective bolus and contrast-enhanced MRA acquisition). The scan time of these sequences can be greatly reduced by parallel imaging.

Contrast-enhanced MR Angiography

These techniques are faster and offer a better signal-to-noise ratio than methods without contrast agent injection. The benefits linked to shortening T1 induced by the Gadolinium chelates are numerous: Increase in the vascular signal which becomes predominant in relation to the inflow effect, avoidance of blood signal saturation, enabling large volumes to be explored, and better turbulent flow imaging.

2.9 Cardiac MRI

Heart exploration in MRI is faced with numerous technical difficulties as it concerns organs with mobile structures: heartbeats, respiratory motion and blood flow. These motions are sources

of artifacts and a range of strategies have had to be developed to deal with these. Recent advances in MRI technique have nevertheless made cardiac exploration possible using MRI in routine clinical practice, with indications in numerous diseases: ischemic, infectious and inflammatory, congenital, valvular, tumoral.

Cardiac MRI sequences basics

Various strategies exist to scan an organ in motion: Fast acquisition sequences, Synchronization with the motion, Containing or stopping the motion. The third strategy can only be applied to respiratory motion if the length of breath-hold is compatible with the patient's clinical state. If breath-hold is not possible, respiratory or echo-navigator gating can be used to synchronize with respiratory motion - the drawback being an increase in acquisition time.

Optimization of cardiac MRI sequences: general principles

Fast MRI sequences will be the technique of choice in cardiac exploration (ultrafast spin echo, fast gradient echo). As well as the RF pulse and gradient sequence, other options can be associated which also accelerate acquisition: Single-shot sequences, Parallel imaging with phased array coils, in some cases dedicated to cardiac imaging, optimized k-space filling: segmented k-space, k-space data sharing, partial k-space. On the other hand, sequences of the echo planar type fail to yield good results due to magnetic susceptibility (pulmonary air, calcifications).

ECG gating

The methods used to synchronize with cardiac motion essentially rely on the electrocardiogram (ECG). The peripheral pulse is only used as a last resort. ECG recording during an MRI examination is perturbed by: The magneto-hydrodynamic effect: the motion of the blood (electric conductor) in the magnetic field produces an electric current which adds on to the cardiac conduction signal. This effect appears on the trace as an increase in the T wave. Currents induced by gradient variation, RF pulses and breathing, which alter the ECG trace. ECG signal degradation will result in a lack of synchronization, lack of diagnostic value of the ECG monitoring trace during MRI, and the need for greater care in placing the electrodes. Indeed it is vital to have an R wave that clearly stands out from the rest of the trace to be machine-detectable. Once this prerequisite is obtained, ECG synchronization can be carried out in two ways: prospective gating, retrospective gating.

Prospective gating

In prospective gating, the R wave serves to trigger MRI acquisitions, which will then all occur at the same moment in the cardiac cycle. The TR is a multiple of the length of the cardiac cycle (1 or 2 cardiac cycles).

Retrospective gating

In this case: MRI acquisition is continuous, with a simultaneous ECG recording to reorganize the data during image reconstruction. With each R wave, the phase encoding gradient changes.

Cardiac synchronization limits the artifacts linked to the motion of the heart and blood flow, thus enabling the different phases of the cardiac cycle to be sampled. The advantage of retrospective gating is the possibility of imaging the entire cardiac cycle, whereas in prospective gating, there is a lapse of time at the end of the diastole. In cine imaging with prospective gating, the first image has a stronger signal, (flash artifact) because longitudinal magnetization has had an added interval in which to recuperate. Partial saturation and the balancing of longitudinal magnetization only occur in the subsequent images. This drawback can be overcome by continuing to apply radiofrequency pulses and gradients during the lapse of free time at the end of the diastole, without recording a signal, to keep longitudinal magnetization in equilibrium. Retrospective gating is not subject to flash artifacts as there is no lapse of free time in the cardiac cycle.

Phase contrast velocity imaging

Quantifying flow in cardiac MRI calls on the same principles as those set out for phase-contrast MR angiography. Phase-contrast flow imagery gives access to quantifying blood velocities and flows. Phase-contrast acquisition comprises sequences with and without encoding of the flows that produce the images in magnitude (“anatomical” aspect of flows) and in phase (“quantitative” aspect: flow direction and velocity). A suitable encoding speed must be chosen beforehand to avoid an aliasing source of errors in high speed measurement. Cardiac gating of these sequences is retrospective, with continuous gradient echo acquisition and phase encoding changes for each R wave. To quantify the flows, the acquisition plane must be perpendicular to the vessel of interest (through-plane). To qualitatively visualize the flow lines, the slice plane must follow the flow axis (in-plane). The number and orientation of the velocity-encoding gradients are adapted to the direction of the flow considered and the type of image (through-plane or in-plane). Accurate flow quantification demands sufficient spatial resolution to accurately measure the diameter of the vessel, precise temporal resolution covering the whole cardiac cycle, an angle close to 90° between the slice plane and the flow axis, an adapted encoding speed, slightly above the maximum velocity of the studied flow.

2.10 Cardiovascular diseases

Cardiovascular diseases are leading causes of morbidity and mortality. In the United States alone, 16.8 million people have coronary heart disease and 6.5 million experience strokes. Imaging techniques to detect atherosclerotic lesions likely to cause myocardial infarction or stroke can help reduce morbidity and mortality rates. Stenotic assessment by luminography techniques such as x-ray angiography, computed tomographic (CT) angiography, or MR angiography has been the mainstay of diagnosis in atherosclerotic disease. However, symptomatic plaque accumulation in the vessel wall can be angiographically invisible owing to the phenomenon of Glagovian remodeling. In recent years, vessel wall imaging has become synonymous with atherosclerosis imaging in comparison with angiographic techniques that can only probe the luminal manifestations of atherosclerosis. Many cardiovascular events are caused by rupture of vulnerable atherosclerotic plaques and subsequent thromboembolic events. In addition to luminal stenosis, plaque burden, plaque composition, neovasculature, and inflammation have been implicated as factors related to plaque vulnerability. Thus, imaging modalities with the ability to interrogate the vessel wall to detect and quantify all biomarkers of atherosclerotic plaques offer the best prospects of identifying vulnerable plaques. Imaging biomarkers of atherosclerosis can be classified into morphological, plaque compositional, and plaque activity indices. Plaque morphology indices include plaque size measurements such as volume, thickness, and area. Plaque compositional measurements pertain to quantitative measures of lipid core, fibrous cap, hemorrhage, thrombus, and loose matrix components. Plaque activity measurements are measures of plaque neovasculature, inflammation, and other cellular and molecular processes. It remains an active research area whether an imaging modality that only quantifies one group of biomarkers can identify the subject at risk, or whether the combination of all aspects of plaque vulnerability should be targeted.

Atherosclerosis is a systemic disease primarily affecting large arteries and is manifested by ischemic complications. Atherosclerotic plaques formed in the coronary circulation, carotid, aortic, and peripheral arteries share similarities in pathogenesis, risk factors, and morphological appearance. Imaging of atherosclerotic plaque in various vascular beds can help study the pathogenesis of atherosclerosis and identify the root causes of stroke, myocardial infarction, or peripheral artery disease. Thus, an imaging modality validated for vessel wall imaging in all vascular beds is ideal for the study of atherosclerosis as a systemic disease. Several imaging modalities that can visualize the vessel wall have been investigated in recent years for imaging of atherosclerosis. Ultrasound (US), CT, MRI, near-infrared spectroscopy, optical coherence tomography, and positron emission tomography have been used for studying vessel wall disease. Of these US, CT, and MRI have found the most favor because they are better suited to in vivo high-resolution imaging of atherosclerosis and can be used in population studies to study plaque

morphology. Ultrasound and MRI are more favored for serial imaging studies because they can be used noninvasively without radiation risk. Magnetic resonance imaging has been validated against histological findings as the criterion standard for identification of major imaging biomarkers of atherosclerosis [13]

Stroke is a serious public health problem and is one of the leading causes of morbidity and mortality worldwide. Ischemic stroke accounts for the majority of all strokes. Patients with substantial carotid narrowing are at increased risk for major stroke; however, the degree of stenosis alone is a relatively poor prediction of neurological events. A great deal of research has been dedicated to investigating and identifying plaque instability: the so-called "vulnerable plaque." However, to understand the mechanisms behind vulnerable plaque, a reliable in vivo imaging method, which can monitor both plaque progression and components, is needed. Because of its proximity to the skin and the availability of atherosclerotic specimens from carotid endarterectomy, the carotid artery provides an excellent location for imaging arterial plaques and study of disease progression or regression. Beyond overall luminal stenosis (the current clinical standard for measuring disease severity), recent pathological studies of both coronary and carotid specimens confirm that large necrotic core with thin fibrous caps, plaque neovasculature, and increased inflammation are all features associated with vulnerable plaques. Pathological classification of atherosclerotic plaque has shown some unique features of carotid plaque morphology due to the high flow rates and the shear forces caused by the bifurcation of the common carotid artery into the internal and external carotids. Plaque ulceration, intraplaque hemorrhage, and calcified nodules may occur more frequently in the carotid than the coronary vascular beds. Another feature of carotid atherosclerosis is the infrequency of total occlusion compared to the coronary beds. In order to detect and further study the increasingly complex findings on atherosclerotic plaques, a robust, reproducible, high-resolution imaging method which can quantify plaque morphology, distinguish tissue components, and detect other pathological features associated with vulnerable plaque is needed. [14]

The ideal clinical imaging modality for atherosclerosis should be safe, inexpensive, noninvasive or minimally invasive, accurate, and reproducible, thus allowing longitudinal studies in the same patients. Additionally, the results should correlate with the extent of atherosclerotic disease and have high predictive values for clinical events. In vivo, high-resolution magnetic resonance imaging (MRI) has recently emerged as one of the most promising techniques for the noninvasive study of atherothrombotic disease in several vascular beds such as the aorta, the carotid arteries, and the coronary arteries. Most importantly MRI can be used to characterize plaque composition as it allows the discrimination of lipid core, fibrosis, calcification, and intra-plaque hemorrhage deposits. MRI findings have been extensively validated against pathology in ex vivo studies of carotid, aortic, and coronary artery specimens obtained at autopsy and using experimental models of atherosclerosis. In vivo MRI of carotid arteries of patients referred for endarterectomy has shown a high correlation with pathology and with previous ex vivo results. A recent study in patients with plaques in the thoracic aorta showed that compared with

transesophageal echocardiography plaque composition and sizes are more accurately characterized and measured using in vivo MRI. The composition of the plaque rather than the degree of stenosis determines the patient outcome. Therefore, a reliable noninvasive imaging tool able to detect early atherosclerotic disease in the various regions and identify the plaque composition is clinically desirable. MRI has potential in the detection arterial thrombi and in the definition of thrombus age. MRI has been used to monitor plaque progression and regression in several animal model of atherosclerosis and more recently in human. Advances in diagnosis prosper when they march hand-in hand with advances in treatment. Thus, MRI opens new strategies ranging from screening of high-risk patients for early detection and treatment as well as monitoring the target areas for pharmacological intervention. Corti et al.[15]

Ultimately, the imaging metho4 should have the potential to not only be used as a screening tool for the presence of atherosclerosis but also to distinguish stable from vulnerable plaques and distinguish patients with high risk of cardiovascular complications. High-resolution magnetic resonance imaging (MRI) is one of the most promising modalities for visualizing the carotid atherosclerotic plaque, as MR allows direct visualization of the diseased vessel wall, has excellent soft tissue contrast, is capable of characterizing plaque morphology, and can potentially monitor progression of the disease. MR imaging is non-invasive, does not involve ionizing radiation, and is highly reproducible. [14]

2.4.2 Carotid disease and MRI techniques

The carotid arteries are the main conduits for blood flow from the heart to the brain. The left common carotid artery (CCA) typically arises directly from the aortic arch, the right from the brachiocephalic artery off the arch. Both eventually bifurcate into an internal carotid artery (ICA), which feeds the brain, and an external carotid artery (ECA), which feeds the rest of the head. [16]

Studies observed that morphological manifestations of the disease are found at some well-defined locations: certain vessel bifurcations (as carotid bifurcation) and in curvatures. The flow in these regions is characterized by unsteadiness and often separation. Atherosclerosis, which develops right at the bifurcation, causes the majority of strokes in patients.[17]. Several studies demonstrated that atherosclerotic lesions are more frequent in the proximal portions of the three major coronary arteries than in the distal segments and in their branches and that carotid disease leads to an ischemic stroke accounting for 15–20%. [18]

Traditionally, therapeutic efforts in carotid disease have been aimed at identifying carotid stenosis in symptomatic patients and treating high-grade stenosis. Stroke recurrence in patients with symptomatic carotid stenosis can be prevented by carotid endarterectomy (CEA) with an absolute risk reduction of up to 17%. Although there is irrefutable evidence that CEA is beneficial in patients with >70% symptomatic stenosis, identifying other patients who may benefit from CEA

continues to be a significant challenge. Based on multiple observational and controlled studies, it is clear that some patients with less severe stenosis and without symptoms may benefit from CEA. In addition, there are patients with severe stenosis in whom CEA is probably not beneficial. In recent years, there has been growing interest in evaluating the carotid plaque in a different manner, placing less emphasis on the severity of the stenosis and more emphasis on the morphology and functional characteristics of the plaque. The term plaque vulnerability has been used to describe the propensity of the plaque to induce local thrombosis and/or embolize distally and cause stroke. New research suggests that identifying the vulnerable plaque in symptomatic or asymptomatic patients may be a more rational approach for the prevention of ischemic events. Identification of the vulnerable carotid plaque using different imaging modalities as carotid ultrasound, computed tomography, and magnetic resonance angiography can help identify plaque features associated with the vulnerable plaque. A multimodal approach to studying the carotid plaque appears to be a promising tool in identifying vulnerable carotid plaques. [18]. Ultrasound examination of the carotid artery is increasingly being used as a surrogate marker of atherosclerosis and is a strong predictor of future vascular events. However, evaluation of the regression of subclinical atherosclerosis by carotid arterial ultrasound examination following treatment of risk factors takes time (ie, more than 1 year is required in most cases to confirm such regression), and therefore more sensitive markers to assess the effect of treatment of risk factors on vascular damage are proposed. Risk factors for CVD cause not only structural, but also functional vascular damage. Several non-invasive methods are currently used to assess functional vascular damage, including measurement of flow-mediated vasodilatation (FMD) of the brachial artery induced by reactive hyperemia, pulse wave velocity (PWV), augmentation index (AI), central blood pressure (BP), etc and these vascular function tests have attracted attention as new tools for determining CVD risk. [19]

Multi-Contrast MRI

A technique well established for plaque characterization is a multi-contrast MRI, which utilizes several MR contrast weightings at a single location to identify and characterize plaque components. For carotid MRI, the multi-contrast approach includes three basic contrast weightings (T1, PD, T2) obtainable with black blood imaging and complementary bright blood imaging, producing angiographic data. In addition, contrast enhancement (CE) of carotid atherosclerosis can quantify vessel wall morphology and key plaque components with excellent accuracy and reproducibility. By using multi-contrast MRI we can image key features of carotid plaques, including differentiating between American Heart Association (AHA) classification of lesion types, intraplaque hemorrhage, fibrous cap and other plaque components and vessel wall thickness.

Contrast Enhancement MRI

Contrast-enhanced MR has also demonstrated its usefulness in distinguishing certain plaque tissues. A gadolinium contrast agent can improve the accuracy of MR in differentiating the lipid-rich necrotic core from surrounding fibrous tissue. The lipid-rich necrotic core shows little if any enhancement on post-contrast T1-weighted images, facilitating differentiation from the surrounding enhancing fibrous tissue. Using pre- and post-contrast T1-weighted images, Cai et al. [20] showed that the lipid-necrotic core, measured as proportion of the vessel wall, was similar on MR images and histological specimens, with values of 30.1% ± 12.5 (standard deviation) and 32.7% ± 12.3, respectively. Furthermore, the area measurements were strongly correlated (r = 0.85; P < .001). Two independent studies also pointed to the importance of CE MRI in characterizing the fibrous cap. Kramer et al. [21] demonstrated that contrast enhancement improved the delineation of the fibrous cap, which was found to be hyper intense relative to the lipid-necrotic core on T2-weighted images. In another study, it was found that gadolinium-enhanced T1-weighted images helped differentiate the fibrous cap from the lipid-necrotic core, with a contrast-to-noise ratio as good as or better than that of T2-weighted MR images but with approximately twice the signal-to-noise ratio. Furthermore, Cai et al. [20], demonstrated that the use of a gadolinium contrast agent not only allows for the identification of the intact fibrous cap, but, more importantly, also allows for the accurate morphological measurements of the fibrous cap. The authors used un-enhanced T1- weighted and contrast-enhanced T1-weighted images to measure the intact fibrous cap, and showed a moderate to good correlation between the MR findings and the excised histological specimen for the maximal thickness length and area measurements of the intact fibrous cap. Quantitative measurement of cap thickness is a promising step towards better identifying plaques with weakened fibrous caps.

2.11 Current Applications of carotid MRI of Atherosclerosis

Carotid Lesion features and their association with neurological symptoms

MRI of carotid artery affords bilateral data acquisition, which provides an opportunity to study atherosclerotic lesion features of both carotids at the same time. Using bilateral acquisition, Saam et al. [22] showed significant differences between symptomatic and asymptomatic plaques in the same patient. Compared with asymptomatic plaques, symptomatic plaques had a higher incidence of fibrous cap rupture (P = .007), juxtaluminal hemorrhage or thrombus (P = .039), type I hemorrhage (P = .021), and complicated AHA type VI lesions (P = .004), and a lower incidence of uncomplicated AHA type IV and V lesions (P = .005). Symptomatic plaques also had larger hemorrhage (P = .003) and loose matrix (P = .014) areas and a smaller lumen area (P = .008).

Plaque progression

Noninvasive imaging of carotid plaque has proven to be particularly powerful in longitudinal studies designed to evaluate the natural history of disease progression and its association with patient symptoms or the response to pharmacological interventions.

Plaque regression

Because of the comprehensive information provided by carotid MRI, this technique is also ideal for monitoring vessel wall changes under treatment. Carotid MRI has been extensively validated for its ability to monitor plaque regression.

Flow and stress

Another application of carotid MRI is to extract quantitative vessel wall morphology and composition information from MRI to be used for hemodynamic and tissue mechanical analysis. Biomechanical stress is also considered to be a major determinant of plaque vulnerability. The fibrous cap rupture of atherosclerotic plaque can be considered to be a structural failure when the structure of plaque cannot resist the pressure and hemodynamic shear stress. From several studies, the feasibility of using combined finite element analysis and high resolution MR imaging to perform stress analysis on carotid plaques is shown. Tang D et al [23] has developed a 3D model of vessel wall strain /stress analysis method based on carotid MRI data and a preliminary study indicates that lipid rich necrotic cores covered by thin plaque caps are associated with both extreme maximum (stretch) and minimum (compression when negative) stress/strain levels, adding to the evidence that fibrous cap is an indicator of vulnerable plaque. Furthermore very recently, it was demonstrated that there is an association between biomechanical stress and USPIO (paramagnetic iron oxide), enhanced MR-defined inflammation within carotid plaque, both known risk factors for plaque vulnerability. This underlines the complex interaction between physiological processes and biomechanical mechanisms in the development of carotid plaques. Groen H et al. [24], provided further evidence that plaque rupture may be linked to flow stress in their study which used MRI to locate a ruptured fibrous cap within an area of high wall shear stress. The ability of MRI to visualize different plaque components and morphology make it a promising candidate to test models of flow and biomechanical stress on carotid plaque.

2.12 Phase-contrast flow and velocity imaging in cardiovascular blood flow

The accurate evaluation of blood flow through the major vessels is an essential aspect of cardiovascular health care. Many conventional techniques for assessing blood flow are invasive or

involve ionizing radiation, and thereby pose significant health risks. Noninvasive alternatives such as Doppler ultrasound, on the other hand, suffer inherent limitations due to their limited depth of penetration and attenuation caused by intervening gas and bone. The sensitivity of MR imaging to fluid motion renders it a potentially superior modality for use in clinical blood flow analysis. (Kraft et al) [25]. MRI is usually displayed as magnitude (modulus) images: brighter pixels contain more signal. The signal is from the rotating transverse magnetization in the pixel, which is a vector quantity (two properties: size and direction). Although the direction is rotating, MRI detects how far it is running ahead or behind a reference-rotating source (oscillator) in the scanner electronics. This ahead or behind quantity is known as phase (phase shift), used for position encoding in MRI because the magnetic field gradients cause phase shifts depending on position-and also on velocity. Phase has a 360° range, beyond which the same values repeat, causing wraparound (aliasing). The phase of each pixel is affected by uncontrolled factors like main field no uniformity and chemical shift, so the phase reconstruction (phase image) is not normally displayed.

2.13 Phase-contrast velocity measurement

Velocity-encoding

For phase-contrast, two opposing gradient pulses known as velocity encoding are added to the imaging sequence of pulses. In pixels containing static tissue, the effects of the two pulses cancel, but if the tissue moves in the time between the pulses, they leave a phase shift in that pixel accurately proportional to velocity along the gradient's direction. The uncontrolled phase errors must be removed to detect only the velocity phase shift; so two scans [typically "reference" and "velocity-encoded (sensitized)"] are usually acquired together. Subtracting the reference phase image from the velocity-encoded phase image makes the phase-contrast image (velocity map). The sensitivity and direction of velocity encoding is flexible and can be repeated for multi-directional velocity imaging. Stationary material is mid-grey (zero-value pixels), with increasing velocities in opposite directions shown brighter (positive pixels) and darker (negative pixels), with an accurate linear relationship to velocity, i.e. velocity in pixel= V_{ENC} x(pixel phase shift/180°), and labelled with direction rather than the ± sign. The velocity encoding value V_{ENC} should be available as an adjustable sequence parameter. A small V_{ENC} represents a highly velocity-sensitive image.

Velocity aliasing or wraparound

If the velocity phase shift exceeds ±180°, it cannot be distinguished from one within the ±180° range, which is displayed instead and known as velocity aliasing (wraparound). Although the measurable range of velocity phase shifts is always 360°, i.e. 2xV_{ENC}, it can be offset in post-processing so that aliasing does not affect the region of interest (ROI). If the true range of velocities

in the ROI exceeds $2xV_{ENC}$, they cannot all be correctly displayed simultaneously; peak velocity may still be found, but mean velocity and flow will be more difficult. Some inaccuracy in V_{ENC} amount and direction occurs in distorted gradient fields. After acquisition, V_{ENC} cannot be changed, so on-line assessment of the velocity images is necessary, and if aliasing appears excessive, repeated with larger V_{ENC}. Unhelpful software often forces users to avoid any aliasing, by using excessively large V_{ENC}, at less obvious cost of lower velocity-noise ratio. Quicker low-resolution images can be helpful for optimization. (Narrowing the display grayscale "window width" does not alter V_{ENC} range, and "window level" is often not linked to V_{ENC} offset, but causes high-velocity pixels to "saturate" the display grayscale full black and white. Note that velocity pixel values may be uncalibrated in images displayed other than by using the dedicated flow processing software).

Pulse sequences for phase-contrast

Phase-contrast requires a strong signal from fast-moving blood, using spoiled gradient-echo sequences with velocity- compensation (even-echo rephasing) and short echo time (TE), running with cardiac gating as a cine acquisition using reduced flip angle. For imaging within a single breath-hold, the sequence usually collects multiple raw data lines per cardiac cycle (i.e. segmented acquisition). The repeated RF pulses for multiple raw data lines per cardiac cycle require further reduced flip-angle and therefore lower signal-to-noise ratio. On some systems, high strength gradient pulses worsen eddy-current effects on the stationary offset, improved by repositioning the patient for each vessel measured to be as near isocentre as possible, and using lower gradient performance (with consequential spatial and temporal resolution losses). A smaller VENC value requires more velocity-encoding strength and duration within the TE, which can conflict with the short TE required in turbulent flow and the short repeat time for segmented imaging. Using the ECG, images are usually repeated at each cardiac-phase for phase-contrast cines. Reference magnitude images show bright systolic blood, enhanced by inflow of unsaturated blood, with little ghosting from blood, due to the velocity-compensation. In the velocity-encoded measurement, the velocity-encoded direction is clearly not completely velocity-compensated. Magnitude images from the velocity-encoded measurement may therefore show signal loss or flow ghosting artifacts in complex or time-varying flows. The earliest cardiac cine image may be delayed by the ECG filtering and communication of R-wave trigger detection through the MRI system to the sequence, and also, in segmented imaging, acquisition of central raw-data after typically half of the cine frame time. For faster imaging, data sampling may best use "centre-out" EPI or spiral , with short sampling durations after each RF excitation for turbulent flow. Phase-contrast sequences can also be accelerated by parallel RF and shared-cine-phase methods. The re-use of transverse magnetization in balanced SSFP does not combine easily and flexibly with velocity encoded phase shifts, but the bright blood signal has attracted some initial investigations for phase contrast.

Phase-contrast image processing

Truly empty pixels appear as "speckle", since the phase shift of low-amplitude noise is random. Ghosting along the phase-encode direction in phase-contrast images, sometimes with a large phase shift, corresponds to even a very weak ghost in the magnitude image. Both effects in phase-contrast images can be zeroed in pixels whose magnitude image value falls below a user-specified "magnitude threshold" in post processing. If the flow of interest in the magnitude image is bright, its phase is not significantly affected by ghosting with relatively weak signal magnitude. However, especially in slow flow where signal magnitude is low, ghosting may become problematic, and random noise also causes phase deviations which appear as noise on pixel velocity values ("velocity-to-noise ratio"); V_{ENC} should be small so that the velocity phase shift is large relative to the random noise, but a small V_{ENC} also tends to increase flow ghosting in the velocity-encoded image. For various reasons (uncorrected Maxwell, eddy currents, small gradient waveform errors), all tissue may show a small erroneous velocity, which may be uniform or vary (linearly or curvedly) across the image. Processing software may allow users to place a correction ROI in stationary tissue, preferably near the vessel being measured; the correction ROI value is subtracted from the vessel velocity. Another approach requires the user to identify stationary tissue all over the FOV (avoiding phase encode wraparound!) and fits a correction slope, which is then subtracted from all pixels for a corrected velocity image. Low SNR in limited amounts of nearby stationary tissue can make background correction difficult to achieve accurately. Phase-contrast images should correct Maxwell (concomitant) errors.

Spatial resolution and image plane alignment

For mean velocity in a vessel, accurate lumen area delineation demands high in-plane resolution. At least four true pixels are needed (not interpolated or zero-filled) across the vessel diameter in both directions for 10% accuracy. The situation is complicated by varying partial volume effects at the edges of the flow, due to surrounding tissue signal level, the type of flow near the vessel boundary (laminar or plug flow), and misalignment of the usually thicker slice than in-plane resolution, so high spatial resolution and thin slice thickness are important. Volume flow measurement is not affected by including zero-velocity pixels, allowing easier ROI definition if magnitude thresholding is used. If velocity encoding is misaligned by angle θ from the flow direction, the measurement gives the true velocity * $\cos(\theta)$. However, this error is small, e.g. 6% at 20° misalignment, and for flow measurements is cancelled by $1/\cos(\theta)$ increase in apparent cross-sectional area. The voxel dimensions and their alignment with flow are also important where a voxel may contain a range of velocities. In the velocity encoded measurement, such a voxel contains a range of phase-shifts and its total signal can be inaccurate or lost altogether, even if it is strong in the reference magnitude image. This effect is concealed when the velocity-encoded

images are not available. It may be improved by larger V_{ENC} to reduce intra-voxel velocity phase dispersion, but this worsens velocity-to-noise ratio.

Temporal resolution

Breath-hold imaging collects multiple lines of raw data for each cine frame in each cardiac cycle, and the cine frame is extended further for velocity mapping by the collection of reference and velocity-encoded data within the same cycle, as opposed to sequential collection on successive cardiac cycles, which extends breath-hold time. Highly pulsatile velocity waveforms may be smoothed, but cine frames retain accuracy less than 60-70 ms, longer if the flow is less pulsatile, and smoothing might sometimes have less effect on mean flow measurements. Flow in smaller vessels also loses accuracy because the breath-hold time limits spatial resolution and further if they move during the cine frame. Breathing patterns can alter cardiac function and flow. Using slower non-breath hold imaging may average such variations, but introduces respiratory artifacts.

Misregistration of flow data

Time differences of a few milliseconds occur between the measurements of position and velocity in the phase-contrast scan, which can misregister oblique flow compared with static tissue. Although partly correctable in sequence design, the remaining "encoding time scatter" can also distort accelerating flow. In velocity maps, phase errors caused by changing velocity reduce with shorter TE, but acceleration into stenoses requires caution. Gatehouse et al. [26]

2.14 Phase velocity mapping - Methods of application

Volume flow measurements

The volume of blood flow in a vessel per cardiac cycle is measured using through-plane velocity encoding in a cine acquisition. The measurement should avoid temporal smoothing of flow pulses (i.e. use fine temporal resolution). If late diastolic flow is negligible, ECG-triggered cine MRI may be used. "Retrospective ECG" or "retrogating" acquires the whole cardiac cycle, and may stabilize stationary offset error. The flow volume per cardiac cycle is the sum of the velocities of the pixels within the ROI multiplied by the area at each cine frame. The ROI around the blood vessel in each frame may require re-drawing for motion and vessel compliance during the cycle. If pixels surrounding the vessel contain so little signal that they show random phase speckle, their inclusion causes errors. The stationary offset error is more significant in comparison to the slower flow often occurring during large fractions of the cardiac cycle, which can be

improved by varying V_{ENC} for those frames, a method infrequently used, perhaps due to its extra complexity [26].

Stenotic flow

The aim is to measure the severity ("hemodynamic significance") of a stenosis. Subject to several assumptions, this appears as a pressure drop through the stenosis (in medicine called a pressure gradient, confusingly). Blood leaves the stenosis in a narrow systolic "jet" of fast flow, which disperses downstream. The stenotic pressure gradient (in mmHg)=4x peak jet velocity (m/s) squared, by the "modified Bernoulli equation", assuming that the upstream velocity is small compared with the jet peak velocity, and that the stenosis obstructs about 70–80% by diameter of the vessel. The factor 4 can be varied according to stenosis diameter measurement Oshinski et al. [27]. Reliable jet signal requires short echo time (TE<4 ms) and velocity compensation. Signal loss around the jet is expected, but the peak velocity in the jet can be measured in a small ROI of only a few pixels-with careful positioning, because the jet velocity varies along and across the jet. Cross-sectional imaging perpendicular to the jet using through-plane velocity encoding should be located correctly along the jet for the peak. For in-plane velocity encoding along the jet using a thin slice, preferably narrower than the jet, the selected slice must be aligned with the jet axis to avoid underestimation. Typically, several "cross-cutting" in-plane and through-plane velocity images are obtained to ensure peak detection. Avoiding pixels affected by signal loss or misregistration, especially by viewing the velocity-encoded magnitudes, overestimating the peak velocity is unlikely. As well as flow, signal loss in magnitude images is used to assess stenosis, since turbulent signal loss is small in normal circulation.

Flow as a source of image contrast

Fresh inflow of fully magnetized blood enhances signal brightness in short TE spoiled gradient-echo cine images, while the magnetization of static or slow-moving material is reduced by the repeated RF pulses ("saturation"). Either this flow enhancement or through-plane velocity images can be used to assess the cross-sectional area of a flow, such as an atrial septal defect or valve opening area. When using magnitude image signal loss to assess turbulence, the robust signal at short TE becomes a drawback, which can be specially adapted for this purpose. In balanced-SSFP imaging, fresh-inflow enhancement is not expected, and spurious flow-brightening and signal loss effects are less well-controlled than in spoiled gradient echo imaging. Phase contrast provides image contrast by differing flow patterns and timings, e.g. the true and false lumina in aortic dissection.

Velocity waveforms and flow patterns

At sufficiently fine temporal resolution, phase-contrast MRI detects abnormal blood velocity waveforms during the cardiac cycle, e.g. the shorter acceleration time caused by increased pulmonary vascular resistance. In renal artery stenosis, the reduced systolic peak in the velocity waveform may be a useful addition to mean flow measurement. Velocity waveforms contain information about vessel compliance and the returning pressure wave from downstream, a topic of great complexity possibly affecting coronary artery flow. Complete acquisition of a complex pulsatile flow requires cine phase contrast in three directions and three dimensions. Ideally using respiratory gating, the acquisition time is at least 20 min accepting some resolution loss. Dedicated acquisition and display software is usually needed. Complete flow acquisitions improve understanding of the asymmetries and some circulatory "tuning" or for computational fluid dynamics.

CHAPTER 3

IN-VIVO

3.1 Wall shear stress measurements in the arterial tree using PC-MRI

Although atherosclerosis is a disease affecting the vascular system as a whole, it has uneven distribution with substantial differences in the localization and progression of different plaques. There are well-known predisposition sites for atheromatic plaques to develop, such as the outer wall of vessel bifurcations and the inner wall of curved arteries[28-31]. On the other hand, it is unclear why some plaques remain quiescent for many years, while others progress rapidly. These considerations suggest that independently of genetic predisposition and cardiovascular risk factors, the presence of local hemodynamic factors play a major role in the generation, progression and destabilization of atherosclerotic plaques. These local hemodynamic factors include flow-generated wall shear stress (WSS) and blood pressure derived tensile stress, with WSS playing the most fundamental role in atherosclerosis[32].

The molecular mechanisms that mediate the effects of WSS are under intensive investigation and exciting data are emerging on this issue. A dysfunctional endothelium, characterized by decreased NO synthesis, facilitates vessel wall entry and oxidation of circulating lipoproteins, monocyte entry and internalization or inflammation, smooth cell proliferation and extracellular matrix deposition, vasoconstriction, as well as a prothrombotic state within the vessel lumen[33-34]. Endothelial dysfunction, traditionally recognised as the earliest manifestation of atheromatosis, is often the result of disturbances in the physiological pattern of blood flow which result in WSS alterations[35-36]. Atherogenesis is promoted by decreased WSS because it is associated with a reduction in several vascular wall functions including endothelial NO synthase (eNOS) production, vasodilatation and endothelial cell repair[37]. These are coupled with increases in reactive oxygen species (ROS), endothelial permeability to lipoproteins, leukocyte adhesion, apoptosis, smooth muscle cell proliferation and collagen deposition[38]. Interestingly, it has been demonstrated that WSS can regulate gene expression, thus modulating endothelial biology[38-40].

Therefore, measurement of WSS may be of clinical significance. However, data of WSS measured in vivo are scarce due to the difficulty in obtaining accurate non-invasive flow data[41]. We reviewed the existing literature on in vivo WSS measurements in healthy humans using PC-MRI, since this technique appears as one of the most promising for non-invasive in-vivo determination of various blood flow characteristics, including WSS.

Wall shear stress definition

When a liquid is flowing inside a straight tube, the velocity of flow is not equal at all points in the tube[42]. The velocity is highest at the center of the tube and drops at points towards the tube wall. This velocity gradient that exists inside the tube is due to frictional forces that are exerted between the adjacent layers of the flowing fluid and between the fluid and the walls of the tube[43]. The frictional forces arise from the viscous properties of the fluid, as defined by the viscosity of the fluid. In the case of blood circulation, the flow of blood induces a "drag" between the outermost layer of blood and the vessel wall due to the viscosity of blood. This drag applies mainly to the inner layer of the vascular wall in contact with blood, the vascular endothelium. The magnitude of wall shear stress depends on the velocity gradient near the tube wall, in other words how fast the flow velocity increases when moving from the tube wall towards the center of the tube. This velocity gradient near the wall is termed wall shear rate (WSR). Wall shear stress is defined as [43-45]:

$$WSS = \mu \frac{du}{dr} = \mu \cdot WSR \qquad (\textbf{3.1.1})$$

In Equation 3.1 , μ is the dynamic viscosity of the liquid, u is the flow velocity and r is the radial position. The derivative of velocity ($\frac{du}{dr}$) is the WSR. WSS is measured in pressure units, $\frac{N}{m^2}$ or $\frac{dyn}{cm^2}$ ($1\frac{N}{m^2} = 10\frac{dyn}{cm^2}$), the dynamic viscosity is measured in poise (1 poise equals 1 $\frac{dyn \cdot s}{cm^2}$) and the shear rate is measured in reciprocal seconds (s^{-1}).

Equation 3.1.1 implies that viscosity is an inherent physical property of the fluid showing how easily the fluid is sliding[44]. It also implies that the velocity gradient at the vessel wall is a linear function of the applied shear stress and vice versa. Water and many other liquids exhibit such behavior and are for that reason called Newtonian or ideal fluids[44-45]. A Newtonian fluid has, by definition, constant dynamic viscosity at all rates of shear[45]. ***When the dynamic viscosity depends on the shear rate, the fluid is termed "non-Newtonian"***. The latter often occurs when the fluid contains sizable particles, as in the case of blood, which is essentially a suspension of erythrocytes, leukocytes and platelets in blood plasma.

The flow under steady (non-pulsatile) conditions of a Newtonian fluid in a cylindrical tube with rigid walls is fully developed into a parabolic velocity profile where the velocity is highest at the center of the tube and zero at the tube walls. This type of flow is usually referred to as ***Poiseuille flow.*** In Poiseuille flow the wall shear stress can be mathematically derived by the Hagen-Poiseuille formula[44-45]:

$$WSS = \frac{4\mu Q}{\pi R^3} \qquad (\textbf{3.1.2})$$

In Equation 3.2, Q is the volume flow, μ is the dynamic viscosity of the liquid and R is the inner radius of the conduit cylindrical tube. Two useful expression of WSS that derive from the Hagen-Poiseuille formula flow are the following[46]:

$$WSS = \frac{2\mu u_M}{R} \quad (\underline{\textbf{\textit{3.1.3}}})$$

and

$$WSS = \frac{4\mu u_{ave}}{R} \quad (\underline{\textbf{\textit{3.1.4}}})$$

In Equations 3.1.3 and 3.1.4 u_M and u_{ave} is the highest velocity (velocity at the center of the tube) and the average flow velocity respectively.

It is obvious that the last three expressions of WSS are only valid under specific assumptions, such as steady conditions of laminar flow, and blood resembling a Newtonian fluid that is flowing inside a straight cylindrical tube with rigid walls. This is hardly the case in arterial circulation where flow is pulsatile and it occasionally becomes turbulent. Additionally, blood vessels are distensible and their cross-section is tapered. Finally, blood can be considered as a Newtonian fluid only under specific conditions. Given these considerations, it is obvious that the values of WSS obtained from equations (3.1.2)-(3.1.4) can only be considered as approximates

The most straight-forward methods of WSS measurement that do not require sophisticated calculations are based on the Hagen-Poiseuille's formula (Equation 3.1.2), which requires the measurement of the blood volume flow rate and the radius of the vessel lumen at the site of flow measurement. Equivalently, WSS can be expressed in terms of the maximum flow velocity (Equation 3) or the average velocity (Equation 4) and thus the determination of WSS may require the measurement of vessel radius, and either the maximum or average flow velocity

More precise but yet more complex methodologies require the determination of shear rate near the vessel wall and the derivation of WSS by its definition given in Equation 3.1.1 ($WSS = \mu \frac{du}{dr}$). In that case velocity measurements have to be obtained adjacent to the vessel wall at a discrete number of points and then use the measured values to 'build' the velocity profile using an interpolation algorithm [47]. The wall shear rate calculation requires an estimate of the slope of the velocity profile near the vessel wall [48]. The accuracy of the calculated value of wall shear stress by this method is a function of the spatial resolution of the velocity measurements, which is the ability of the used measurement method to define accurately the varying velocities of adjacent points [49] and the interpolation algorithm used to 'build' the velocity profile [47].

Phase-contrast MRI (PC-MRI) is a powerful tool for in vivo measurement of blood flow, non-invasively, without ionizing radiation that can measure flow accurately[50-52], with flexibility of image spatial and temporal resolution to suit the application , and has access to all

directions of flow at any location in the body[53]. From the measured velocity profiles, shear rates and shear stress values can be obtained. PC-MRI the velocity data can be precisely matched with anatomic pictures, providing an integrated anatomic and functional examination[54]. However there are also several limitations involved to PC-MRI blood flow velocity measurements. One important limitation when using MR velocity measurements for the calculation of shear stress is the identification of the blood - vessel wall boundary within the image pixel since that pixel may be partially covered with moving blood and partially covered by the stationary vessel wall [54]. This problem arises from the low spatial resolution of the technique (0.5 - 1mm)[46,55]. For reliable blood flow velocity measurements, the information of four pixels has to be collected, limiting the true spatial resolution of velocity assessment to about 1 - 2 mm [46]. Due to the limited spatial resolution, blood flow velocities cannot be measured closer to the wall than 1000 – 1200 μm [46], and as a consequence the wall shear stress values are underestimated. Another limitation of the method is its low temporal resolution, since MR imaging measurements are obtained every 25 – 30ms [46,55], hence special precautions are required to be able to study dynamic processes. Finally, accurate velocity profiles can only be obtained in relatively straight vessels [46]. Therefore, WSS assessment by PC-MRI is particularly challenging for small vessels such as the coronary arteries. Additionally to their small size, it is difficult to obtain WSS by PC-MRI due their tortuous pathways and motion with both the cardiac and respiratory cycles [53]. Therefore, although the coronaries are particularly susceptible to atherosclerosis, no in vivo WSS data obtained by PC-MRI currently exist for the coronary tree.

Apart from the spatial resolution of velocity measurement, WSS calculations also depend on the method that is used to 'build' the velocity profile based on the obtained velocity data since WSS values result as the 'slope' or the 'derivative' of that velocity profile at the vessel wall [47]. Various methods of diverse complexity have been used, from simple linear extrapolation methods that approximate the slope of the curve by assuming that it is a line, to advanced methods that assume parabolic velocity distribution at the whole circumference of the vessel. Some investigators instead of calculating WSS as the gradient of velocity near the vessel wall assume that blood flow at the site of WSS measurement can be approximated as Poiseuille flow and use single average or maximum velocity measurements or average flow rate measurements to estimate WSS. The utilization of various methodologies results in deviations at the measured WSS values. Indeed, the comparison of different methods to estimate shear rate from velocity measurements has revealed a statistically significant difference for the main effect of the method (i.e., the method of shear rate calculation from the same velocity data) [56].

We reviewed the existing literature on in vivo WSS measurements using PC-MRI techniques. Only studies on healthy volunteers have being included and studies on patients without vascular disease at the site of WSS measurement. We have tabulated relevant data from studies that have been published up to April 2007. In the following sections we present the key features of the methodology followed at each study whereas the image sequence parameters of each study are presented in Table 1. The studies are ordered according to the arterial site of measurement.

Carotid Arteries

Oyre et al [57] included in their study seven healthy young volunteers (mean age 26.4 years, 4 men). WSS was measured at the common carotid artery, 2 cm below the carotid bifurcation. A 1.5 T whole body MR scanner was used with a standard 8-cm diameter circular surface coil positioned over the carotid artery inside a standard head coil. Initially, visualization of the morphology of the common carotid artery was performed by spin echo based sagittal, transverse and coronal scout images. Perpendicular flow measurements were based on an ECG-gated gradient-echo pulse sequence with bipolar velocity encoding gradients. The WSS calculation methodology of this study is based on a priori knowledge of the parabolic blood velocity distribution within a thin boundary layer at the vessel wall. The parabolic distribution is applied to the velocity data from the whole circumference of the vessel. By this technique a three dimensional paraboloid (3DP) model can be fitted to the velocity data. This model is valid for Poiseuille flow in rigid tubes. WSS was calculated by means of Equation 3.1.1 ($WSS = \mu \frac{du}{dr}$). Wall shear rate was calculated by differentiating the 3DP model at the wall. Peak systolic, end-diastolic and average WSS over the cardiac cycle were calculated. For comparison, WSS was also calculated using the central peak velocity and applying Equation 3.1.3 ($WSS = \frac{2\mu u_M}{R}$) of Poiseuille flow.

Masaryk et al [56] studied five healthy young volunteers. WSS was measured at the cervical segment of the internal carotid artery. The primary purpose of the study was to investigate the accuracy and establish the feasibility of three methods for calculating shear rate from PC-MR data. These methods are linear extrapolation, linear extrapolation with correction for wall position and quadratic extrapolation. All three methods approximate the slope of the velocity profile. Linear extrapolation and linear extrapolation with correction for wall position approximate the slope of the curve by assuming that it is a line and the two measured velocities near the wall are used to calculate the slope of the line assumed to pass through them. Quadratic extrapolation consists of fitting a quadratic or a parabolic curve to three points and then calculating the slope of this curve at the wall. Quadratic extrapolation was found to be the most accurate of the three tested. Wall shear rate values obtained by this method were used to calculate WSS by means of Equation 3.1.1 ($WSS = \mu \frac{du}{dr}$). Peak systolic and average WSS over the cardiac cycle were calculated.

In a study by Wu et al [58], ten healthy young volunteers were included (mean age 23.6 years, 5 male). Wall shear rate (WSR) was estimated using a multi-sectored three dimensional paraboloid (3DP) method and then converted to WSS using the Casson Equation (Whitemore, 1968): $\sqrt{WSS} = \sqrt{\mu \cdot WSR} + \sqrt{\tau_0}$, where τ_0 is the yield stress assumed to be 0.01 N/m^2. Whole blood Casson viscosity was measured individually from each volunteer at blood samples taken after the MR examination using a Brookfield cone/plate viscometer. Maximum, mean and minimum WSS values were calculated.

In a second study by Wu et al [59], twenty healthy young volunteers were included (mean age 23.9 years, 10 male). Wall shear rate (WSR) was estimated using a multi-sectored three dimensional paraboloid (3DP) method. The WSR values estimated by this study were the mean WSR, the maximum WSR and the minimum WSR during the cardiac cycle. Since this study provided only WSR data we converted them to WSS data by means of Equation 3.1.1 ($WSS = \mu \frac{du}{dr}$).

In a study by Stokholm et al [60], eight healthy volunteers were included (mean age 26.8 years, 5 male). WSS was measured at the flow divider and the lateral wall of the carotid artery bifurcation. Wall shear rate (WSR) was determined using a three-dimensional paraboloid (3DP) fitting technique. WSS throughout the cardiac cycle was derived by means of Equation 3.1.1 ($WSS = \mu \frac{du}{dr}$) by differentiating the polynomial of the 3DP model at the vessel wall to obtain the WSR. WSS was calculated for the flow divider and the lateral wall of the bifurcation.

Oshinski et al [41] included eight healthy volunteers were (mean age 63.6 years, 6 female). WSS was calculated by means of Equation 3.1.4 ($WSS = \frac{4\mu u_{ave}}{R}$). The mean value of WSS over the cardiac cycle was calculated.

Aorta

In a study by Oshinski et al [48], eight healthy volunteers (six men, age range 22- 35 years) included. The method for calculating the WSS was based on the slope of the velocity profile using two pixels, the one that included stationary tissue (i.e. lumen wall) and the first pixel adjacent to it. Application of Equation 3.1.1 ($WSS = \mu \frac{du}{dr}$) yielded the maximum, minimum and mean WSS values throughout the cardiac cycle for the posterior and anterior walls of the aorta.

In a study by Oyre et al [60] eight subjects (mean age 26.4 years) were considered. WSS measurement at the anterior and posterior walls were based on the determination of the derivative of the velocity profile from two velocity measurements at and near-to the vessel wall, similarly to the previous study. Application of Equation 3.1.1 ($WSS = \mu \frac{du}{dr}$) yielded the maximum, minimum and mean WSS values throughout the cardiac cycle for the posterior and anterior walls of the aorta.

Pedersen et al [61] measured WSS in a sample of eight volunteers (mean age 26.4 years). The method was the same as the one in the previous study; based upon two velocity measurements

and using Equation 3.1.1 ($WSS = \mu \frac{du}{dr}$). Mean WSS values were calculated at four wall locations (anterior, posterior, right and left).

Cheng et al introduced a novel method for the calculation of WSS and applied it in one healthy subject (age 20 years) at the abdominal aorta. WSS was quantified by differentiating velocity interpolation functions on a band of elements in the neighbourhood of the vessel. The mean value of WSS was calculated.

Taylor et al [64] studied WSS variation between rest and during lower limb exercise in a sample of eleven healthy normal subjects that consisted of six males (mean age 22.5 years) and five females (mean age 24 years). Following the work of Cheng [63], they used a cardiac-gated cine PC-MRI to monitor WSS levels in the human abdominal aorta during rest and lower limb exercise in an open 0.5 T magnet unit. Mean WSS values were calculated by the method of the Langrangian interpolation polynomials described in the work of Cheng et al [63]. The mean value of WSS was calculated at rest and during exercise.

Cheng et al [65] continued their study of the effect of lower limb exercise on the levels of WSS in the abdominal aorta by considering the differences in these levels between men and women. Six male subjects (mean age 22.3 years) and five female subjects (mean age 25.2 years) underwent PC MRI study at the supraceliac and infrarenal levels of the abdominal aorta. In this work, again an open 0.5 T magnet unit was used with a MR-compatible bicycle. For the WSS calculation a threshold set method to segment the aortic lumen was used and the velocity profile of the blood near the vessel wall was represented with third order Lagrangian interpolation. The mean value of WSS was calculated at rest and during exercise for the male and the female populations.

Cheng et al [66] in another work presented WSS variations at rest and during lower limb exercise for a particular age group. The group consisted of 8 subjects (7 male, aged range 50-70 years). WSS was calculated at the supraceliac and infrarenal arteries during rest and during light exercise in an open 0.5 T magnet with a MR-compatible bicycle. WSS was computed by means of velocity measurements and segmentation of the aortic lumen using third order Lagrangian interpolation functions. The mean value of WSS was calculated at rest and during exercise

Wentzel et al [67] studied WSS in the human descending thoracic aorta in a group of eight healthy asymptomatic patients. Wentzel et al used a 1.5 T MRI unit to study plague progression as a function of WSS levels in the descending aorta. Measurements were taken at 4 locations (segments) of the thoracic aorta with a separation of 2 cm starting from the arch, and each segment was divided into 4 quadrants. WSS was determined through the two dimensional derivative of the velocity profile (SR) in the x and y direction. The maximum, minimum and mean WSS values throughout the cardiac cycle were calculated.

Femoral arteries

Wu et al [59] studied twenty healthy young volunteers (mean age 23.9 years, 10 male). The same scanning procedure and identical scanning parameters were used as in the same study of Wu at al [58] at the carotids described earlier. Wall shear rate (WSR) was estimated using a multi-sectored three dimensional paraboloid (3DP) method. The WSR values estimated by this study were the mean WSR, the maximum WSR and the minimum WSR during the cardiac cycle. Since this study provided only WSR data we converted them to WSS data by means of Equation 3.1.1 ($WSS = \mu \frac{du}{dr}$). Maximum, mean and minimum WSS values were calculated.

Silber et al [68] included twenty-four healthy volunteers (age range 21 – 41 years, 15 female). WSS was measured at the superficial femoral artery. For the WSS calculation the velocity pixels were fit by a least-square method to a parabola with the assumption that blood flow velocity at the lumen is zero. Wall shear rate was calculated as the slope of the velocity profile at the lumen-wall interface. Wall shear rate values obtained by this method were used to calculate WSS by means of Equation 3.1.1 ($WSS = \mu \frac{du}{dr}$). The peak systolic WSS was calculated.

Amann-Vesti et al [69] studied 9 healthy volunteers (mean age 36.8 years, 5 female). A simplified approach of velocity data fitting by three-dimensional paraboloid was used in which WSS measurements where performed only at the site with the maximum velocity gradient along the circumference of the vessel. The point of maximum shear rate at the vessel was identified and WSS was calculated by means of Equation 3.1.1 ($WSS = \mu \frac{du}{dr}$). Whole blood viscosity was determined individually for each volunteer using a rotational viscometer. The maximum WSS was calculated.

Brachial arteries

Wu et al [57] included twenty healthy young volunteers in their study (mean age 23.9 years, 10 male). The same scanning procedure and identical scanning parameters were used as in the same study of Wu at al [58] at the carotids described earlier. Wall shear rate (WSR) was estimated using a multi-sectored three dimensional paraboloid (3DP) method. The WSR values estimated by this study were the mean WSR, the maximum WSR and the minimum WSR during the cardiac cycle. Since this study provided only WSR data we converted them to WSS data by means of Equation 3.1.1 ($WSS = \mu \frac{du}{dr}$). The calculated maximum, mean and minimum WSS values were calculated.

Silber et al [68] studied twenty-four healthy volunteers (age range 21 – 41 years, 15 female). WSS was measured at the brachial artery. For the WSS calculation the velocity pixels were fit by a least-square method to a parabola with the assumption that blood flow velocity at the

lumen is zero. Wall shear rate was calculated as the slope of the velocity profile at the lumen-wall interface. Wall shear rate values obtained by this method were used to calculate WSS by means of Equation 3.1.1 ($WSS = \mu \frac{du}{dr}$). Peak systolic WSS was calculated.

3.2 Wall shear stress calculation in the human aorta.

The study population consisted of twenty subjects (13 male, range 22-71 years, mean 39.25 years) submitted to cardiac MRI examination at our institution. All procedures were performed in accordance with institutional guidelines, and all patients gave informed consent. The study was approved by our ethics committee.

MR imaging was performed on a 1.5T scanner (Intera 1.5T, Philips Medical Systems, Best, The Netherlands) using a 5-element phased array cardiac coil for signal reception. As part of our cardiac MRI protocol, a breath-hold phase contrast gradient echo sequence with retrospective cardiac gating was obtained at a level perpendicular to the long axis of the aorta approximately 2cm above the aortic valve. Sequence parameters were as follows: TR=4.2ms, TE=2.6ms, FA=15º, image acquisition matrix=144x142 (frequency x phase encoding steps), reconstruction matrix=256x256, FOV=39cm x 39cm, percentage FOV=0.86, ST=10mm, 1 NSA, VENC=150cm/s.

Methodologies that have been previously used for the estimation of WSS at the arterial tree using blood flow velocity measurements by phase contrast MRI were employed. All methodologies require the value of dynamic viscosity for the estimation of WSS. We have used the constant value of $0.035 \frac{\text{dyn} \cdot \text{s}}{\text{cm}^2}$, considering blood as a Newtonian fluid.

Average Flow method (AFM)

This method of WSS estimation is based on Poiseuille's theory of flow and the resulting Hagen-Poiseuille formula. Poiseuille flow describes the type of laminar flow under steady (non-pulsatile) conditions of a Newtonian fluid in a cylindrical tube with rigid walls. Under these conditions flow is fully developed into a parabolic velocity profile where the velocity is highest at the center of the tube and zero at the tube walls. It can be derived that in Poiseuille flow, WSS can be mathematically derived by the Hagen-Poiseuille formula[67-69]:

$$WSS_{systolic} = \frac{4\mu Q}{\pi R^3} \qquad (3.2.1)$$

In equation *50*, μ is the dynamic viscosity of the fluid, Q is the volume flow and R is the inner radius of the conduit tube at the site of flow measurement. Using phase contrast MRI velocity

measurements blood volume flow can be calculated as $Q = Au_{mean}$ where A is the arterial cross-sectional area and u_{mean} is the mean blood velocity across the cross section measured at peak systole. Systolic WSS can then be estimated by Equation 2 using the calculated volume flow Q and measuring the corresponding inner radius R of the artery.

Average Velocity and Maximum Velocity Methods (AVM and MVM)

In Poiseuille flow, the maximum flow velocity (the flow velocity at the centre of the tube) is double the average flow velocity. Systolic WSS can be estimated by measuring the maximum flow velocity (u_{max}) or the average flow velocity (u_{ave}) and the inner radius (R) of the conduit tube according to the equations[70]:

$$WSS_{systolic} = \frac{4\mu u_{ave}}{R} \quad (3.2.2)$$

$$WSS_{systolic} = \frac{2\mu u_{\max}}{R} \quad (3.2.3)$$

Using phase contrast MRI the maximum and average flow velocities and the inner radius of the artery can be obtained at peak systole, thus systolic WSS can be estimated by substituting these values to equations 51 and 52.

Linear Method (LM)

This method of WSS estimation has been previously described [71] and it is based on the definition of WSS given by equation 3.1. It utilizes the estimation of the velocity gradient near the vessel wall, namely the wall shear rate (WSR). The simplest way to estimate WSR using phase contrast MRI velocity measurements is to use the two velocity measurements at points (locations) closest to the vessel wall and then calculate the ratio $\frac{u_2 - u_1}{r_2 - r_1}$ where u and r denotes the measured blood flow velocity and the measured distance from the vessel wall at the selected points. WSS can be then estimated as the product of dynamic viscosity and WSR (Equation 3.1). Four blood velocity profiles were considered at maximum systole in each patient on MRI phase contrast images (Figure 1). These profiles were determined along four directions with a step of 45 degrees in the clockwise direction starting from the anterior aortic wall. Image analysis and statistical feature extraction as well as the definition of Line of Interest (LOI) on the selected images were performed with the Image J software [72]. A cross-check analysis of the obtained statistical

features – ROI area, minimum, mean and maximum velocities - was performed using the accompanied Philips 1.5 Tesla Magnet workstation software, which revealed complete agreement.

Consequently, an elliptical region of interest (ROI) was manually defined (Figure 2). Wall position was determined with the aid of an experienced radiologist at the magnitude images and then was transferred on the corresponding phase contrast images. Statistical features such as minimum, maximum and mean pixel values were extracted from all the images in the selected image sequence. The phase image that exhibited the highest mean value of pixel intensity from the image-stack was selected, highlighted and was considered to be the one corresponding to the moment of maximum flow. Following the image selection step, the next step involved the LOI definition. The LOI was taken as a linear ROI drawn across the aorta on the magnitude image and was transferred on the corresponding phase contrast velocity image (Figure 2). For each patient, four such LOI were selected in order to obtain four velocity profiles inside the vessel.

The determination of ROI and LOI was performed with the help of an experienced radiologist. Consequently, in order to obtain the velocity values in units of $\frac{\text{cm}}{\text{s}}$ we used the rescale slope and rescale intercept values provided by the appropriate DICOM image header tags which in the particular case of phase contrast images correlate pixel intensity values to velocity values. The first two pixels inward the vessel wall were chosen at each LOI and the corresponding velocity values were extracted. Shear rate at the wall and subsequently WSS was calculated using the aforementioned velocity values. Thus two WSS values were obtained for each LOI and a total of 8 WSS values were obtained at each systolic image. The average of these 8 values was then calculated and considered as the circumferential systolic WSS. Using the obtained velocity profiles, we fitted a parabolic curve using the Levenberg-Marquardt method to the velocity data. The curve was described by a quadratic function of the form $u = ar^2 + br + c$.

3.3 Wall shear stress calculation throughout the cardiac cycle

Having established a clearer view of how the physical and the mathematical formalism of the WSS parameter presents itself and causes it to vary spatially depending on the mathematical formalism and the respective methodology, the next logical and scientific step was to examine – for the same cohort of patients-the WSS variation within the cardiac cycle using once again the quantities that apply to the three ‘equivalent’ equations.

Blood flow measurements were performed retrospectively at MRI scans of 20 patients (range 22-71 years, 13 male) that have undergone routine cardiac MRI examination at our department. The population of the study was randomly selected among non-atherosclerotic patients. As part of our cardiac MRI protocol a breath-hold phase contrast gradient echo sequence

with retrospective cardiac gating was obtained at a level perpendicular to the long axis of the aorta approximately 2cm above the aortic valve. MR imaging was performed on a 1.5T unit (Intera 1.5T, Philips Medical Systems, Best, the Netherlands) using a 5-element phased-array cardiac coil for signal reception. Sequence parameters were as follows: Time Repetition-TR=4.2ms, Time Echo-TE=2.6ms, Flip Angle-FA=15º, image acquisition matrix=144×142 (frequency × phase encoding steps), reconstruction matrix=256×256, Field of View-FOV=39cm×39cm, percentage FOV=0.86, Slice Thickness-ST=10mm, Number of scan acquisitions-NSA=1, Velocity Encoding - VENC=150cm/s. 40 images per patient were reconstructed covering the entire cardiac cycle with a temporal resolution of 13-29 ms depending on heart rate.

All patient images were transferred to MRI system's workstation (ViewForum, Philips, The Netherlands) and segmentation of the aorta was performed using the anatomical images. Elliptical ROIs were defined by an expert radiologist which included the aorta lumen, and excluded the aortic wall (Figure 1a). The software of the workstation automatically provided the following parameters: ROI area (cm^2), aortic lumen diameter (cm), blood volume flow (ml/s), mean and maximum blood flow velocities (cm/s).

Velocity profiles were acquired in radial directions across the arterial lumen with a 45° step clockwise from the A-P direction (Figure 1b). A parabolic curve using the Levenberg-Marquardt method was fitted to the velocity data. The curve was described by a quadratic function which was selected so that for each velocity profile the fitted curve matched exactly the measured velocity values near the vessel wall (Figure 2).

Three well-established methodologies that have been previously used for the estimation of WSS at the arterial tree using blood flow velocity measurements were employed [73][74][75][76]. Figure 2
These methods of WSS estimation are based on Poiseuille's theory of flow and the resulting Hagen-Poiseuille formula. Poiseuille's theory of flow describes the type of laminar flow under steady (non-pulsatile) conditions of a Newtonian fluid in a cylindrical tube with rigid walls. Under these conditions, flow is fully developed into a parabolic velocity profile where the velocity is highest at the center of the tube and zero at the tube walls.

Systolic WSS values were estimated on the image that exhibited maximum flow, whereas the diastolic WSS values were estimated on the last image of the sequence (before the next R-wave). For each methodology the image of maximum WSS was defined as the image that exhibited the highest value of flow, average velocity and maximum velocity respectively. Similarly, minimum WSS values were obtained by the images of the cardiac cycle that exhibited minimum values of volume flow, mean and max flow velocity.

Average Flow (AF) method

It can be derived that according to Poiseuille's theory of flow, WSS is given by the Hagen-Poiseuille formula [77,78]:

$$WSS = \frac{4\mu Q}{\pi R^3} \quad (3.3.1)$$

In Equation (1), μ is the dynamic viscosity of the fluid measured in poise (P), Q is the volume flow measured in ml/sec and R is the inner radius of the conduit tube at the site of flow measurement measured in cm. WSS throughout the cardiac cycle was estimated by Equation (1) using the calculated volume flow Q and the inner radius R of the artery. The radius of the aorta was measured at the magnitude images along four directions with a step of 45 degrees in the clockwise direction starting from the anterior aortic wall. The radius used in Equation (1) was the average of the four diameters. Intra-class correlation coefficients (ICCs) were used to assess the degree of agreement among four measurements performed in each subject regarding diastolic and systolic diameter. The ICCs was calculated by arranging an n×k table for each one measure (i.e. diastolic diameter, systolic diameter), where n was the number of subjects (n = 20) and k was the number of measurements (k = 4). In particular, we used the single measure, two-way mixed model ICC. Moreover, ICC was used to evaluate whether there is any agreement between vessel's diameter measured during systole and diastole. Calculations were conducted through Reliability Analysis using SPSS for Windows (v13, SPSS Inc, Chicago, IL). The results regarding the degree of agreement among four measurements for diastolic and systolic diameter, separately, are presented in Table I. The ICC values were > 0.9, suggesting a high degree of agreement among 4 measurements. Therefore, in order to evaluate the degree of agreement between vessel diameter during systole and diastole, we used the average of four measurements for each measure. The ICC was high (ICC = 0.771, $p<0.001$), indicating a satisfactory agreement between the diameter in systole and diameter in diastole. Therefore for each patient, the radius of the artery measured at maximum systole was used for all WSS calculations. Regarding the dynamic viscosity of blood, we have used a constant value of 3.5cP, considering blood as a Newtonian fluid.

Average Velocity (AV) and Maximum Velocity (MV) methods

According to Poiseuille's theory of flow, maximum flow velocity (the flow velocity at the centre of the tube) is double the average flow velocity. WSS can be estimated by measuring the average flow velocity (u_{ave}) or the maximum flow velocity (u_{max}) and the inner radius (R) of the conduit tube according to the following equations[74]:

$$WSS = \frac{4\mu u_{ave}}{R} \quad (3.3.2)$$

$$WSS = \frac{2\mu u_{max}}{R} \quad (3.3.3)$$

Average flow velocity (u_{ave}) and maximum flow velocity (u_{max}) were measured throughout the cardiac cycle. WSS was calculated by Equations (2) and (3) using the measured velocities, the

corresponding inner radius R of the artery measured at maximum systole as described previously and the constant value of dynamic viscosity μ (μ=3.5cP).

Oscillating Shear Index (OSI)

Oscillating Shear Index (OSI) is an important parameter of pulsatile blood flow which is used to quantify the variation of WSS over the cardiac cycle. OSI is defined as [79]:

$$OSI = \frac{1}{2}\left[1 - \frac{\left|\int_0^T WSS \cdot dt\right|}{\int_0^T |WSS| dt}\right] \quad (3.3.4)$$

OSI is a dimensionless parameter that describes the degree of deviation of WSS from the antegrade flow direction. Small OSI values (close to 0) indicate small variations of WSS during the cardiac cycle. Conversely, OSI values close to 0.5 indicate that WSS is subject to large variations and can take zero or negative values at parts of the cardiac cycle which means that at those time instances flow is stopped or reversed. OSI was calculated for the derived WSS values calculated by the three methodologies throughout the cardiac cycle.

Statistical analysis

Results obtained by the three considered methodologies were compared using one-way analysis of variance (ANOVA) followed by Bonferroni method of post-hoc analysis when statistical significant difference was obtained. Probability values less than 0.05 were considered statistically significant.

CHAPTER 4

IN VITRO

The present part of the thesis deals with the blood flow estimation by means of Magnetic Resonance Imaging. The MR imaging system used, was a 1.5 Tesla scanner (Intera 1.5T, Philips Medical Systems, Best, the Netherlands) of Attikon Hospital (Second Department of Radiology). The experimental set up consists of a flow phantom, simulating blood flow through blood vessels under chosen conditions. Gradient echo (phase contrast) sequences used, precisely: SQ flow and QFP sequences. MR phase-contrast technique quantifies and displays flow velocities in real times. The sequence uses a two-dimensional selective radiofrequency pulse followed by flow-sensitizing gradients with an echo planar readout. It provides the simultaneous display in real time of both an anatomic image for positioning and the through plane flow-velocity data. By controlling scan position and orientation interactively, one can optimize flow signal. The retrospective search of measurements is carried out with the database of a software used, called EVORAD. The software of the workstation automatically provided the following parameters: ROI area (cm^2), vessel lumen diameter (cm), blood volume flow (ml/s), mean and maximum blood flow velocities (cm/s).

4.1 Flow phantom Components

The flow phantom developed by our laboratory consists of the following main components as seen in figures 10-11.More specifically:

The pump

The human heart can be considered to be the pump of the circulatory system. The atrioventricular valves (AV valves), which separate the atria from the ventricles, allow blood to flow from the atria to the ventricles, but prevent flow in the opposite direction. The right AV valves is called the tricuspid valve. The left AV valve is called the mitral valve. The opening and closing of the AV valves is dependent on pressure differences between the atria and ventricles. When the ventricles relax, atrial pressure exceeds ventricular pressure, the AV valves are pushed open and blood flows into the ventricles. However, when the ventricles contract, ventricular pressure exceeds atrial pressure causing the AV valves to snap shut. On purpose of simulation the aforementioned circulation, the flow phantom incorporates a single-head positive displacement diaphragm pump (Grundfos DMX 321-6, Grundfos, Denmark) to simulate heart function (fig.?). The employed pump can provide varying flow rates to simulate blood flow at small arteries such as the coronaries, medium sized vessels such as the carotids and large vessels such as the

pulmonary arteries and the aorta. The pump consists of two separate valves, the suction valve and the release valve (fig.?). The suction valve is equivalent to the human atrioventricular (AV) and the release valve is equivalent to the semilunar valves (pulmonary valve and aortic valve) that supply blood to the circulatory system. The pump valves, similarly to the heart valves, maintain the unidirectional flow of blood by prohibiting fluid backflow. The dosing head of the pump and the attached moving diaphragm simulate the ventricle of the myocardium. An eccentric moves the diaphragm, by means of a spring-loaded plunger, to create a vacuum into which the fluid from a reservoir beneath the pump enters the dosing head through the suction valve. When the fluid enters the dosing head, the valve immediately closes to prohibit backflow. Next, the diaphragm moves in the opposite direction compressing the fluid and causing the release valve to open. The fluid is then ejected into the circulatory system and the release valve closes to prohibit further backflow. The amount of fluid ejected to the circulatory system can be adjusted by a flow adjustment knob which controls the diaphragm movement length (fig.9). The operation of the pump is controlled by an electrocardiogram (ECG) generator.

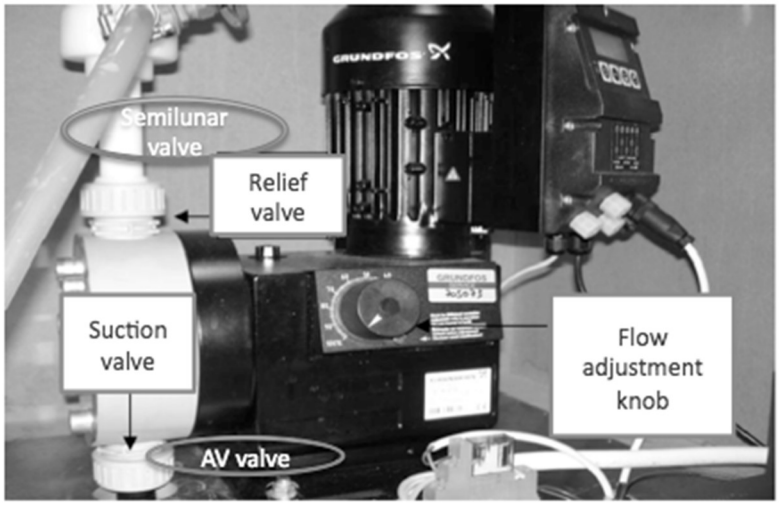

Fig10. *The positive displacement pump. Valves and flow adjustment knob are visible*

ECG Signal Gating

In order to achieve a realistic pump operation, an ECG generator (MediCal 430B, Medi Cal Instruments Inc., Ohio, USA) is connected to the pump through an electronic converter and a Programmable Logic Controller (PLC) as seen in figure 10. The ECG generates a realistic P-QRS-T waveform, which is converted to a 24 Volt square pulse by an electronic set-up. The PLC introduces an adjustable time delay to the pulse. The signal is then driven to a relay, which is configured, to close anytime it receives the signal thus triggering pump operation. Through ECG signal gating the pump can accurately simulate the pulsatile nature or arterial blood flow.

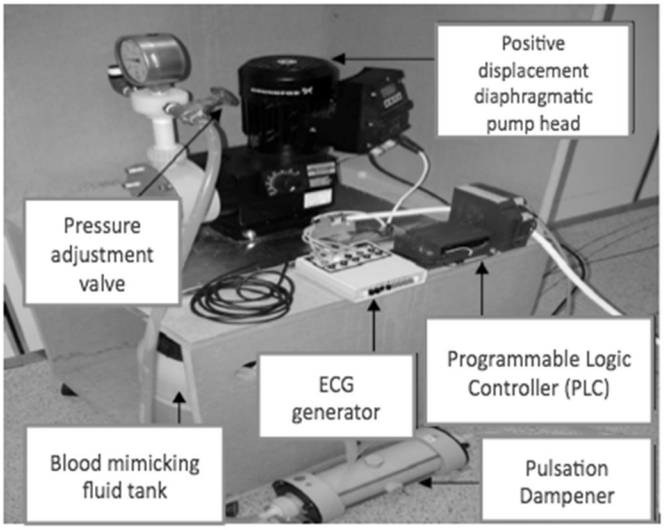

Fig.11 *The pump and the connection with the ECG and PLC*

Tubing

The circulation continues to the simulated circulatory via the tubes. At the exit of the pump, the fluid enters the main supply tube, which is a transparent elastic tube, made of PVC with an inner diameter of 1inch and wall thickness of 2mm. The fluid distributor is a robust 30 cm long plastic tube of 2,54 cm (1 inch) inner diameter with multiple side branches that drive flow of various diameters, or the respective tube if one tube is used. Appropriate switches have been embodied to the distributors that enable the user to specify which tube(s) will be used. In this work a tube of one diameter was used for each set of measurements. The nominal inner diameter of the output tubes are: 6 mm for the straight PVC tube and 8mm for the glass stenotic tube, (corresponding to healthy carotid vessel and unhealthy peripheral artery respectively). The output tube lay on a wooden base to avoid movement due to flow and to ensure the mechanical stability of the system. The tube is 'sandwiched' between two layers of gelatin used to simulate tissue material. The lower gelatin layer is placed on the bottom of the wooden base and the upper layer covers the upper side of the tubes. This set up is seen in figures ?,?. The dimensions of the gelatin layers are 4cm thick and their length and width is equal to that of the wooden base (30cm by 30cm). Additionally to the fixed PVC diameter tube, as aforementioned one stenotic glass tube was constructed in our laboratory in order to study flow in the presence of a stenosis. The glass tube is 50 cm in length and the stenosis is introduced at the center of the tube to provide adequate inlet length to ensure a fully developed laminar flow at the entrance of stenoses. The nominal inner diameter of the glass tube at its non-stenotic part is 8mm. The introduced constriction is axisymmetric of 90.2% diameter stenosis (99% area stenosis) as measured from CT scans.

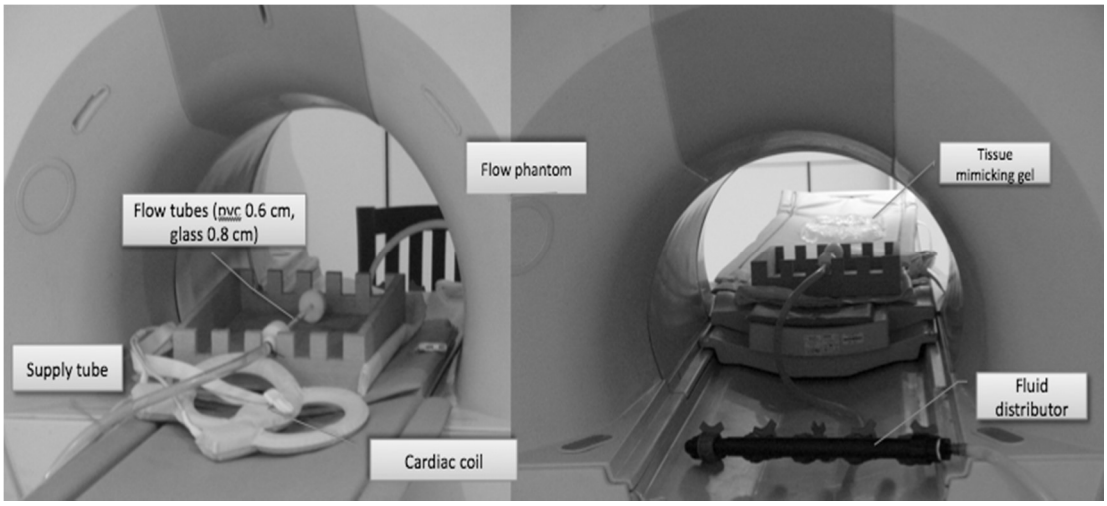

Fig.12 *Image of the flow tube, the wooden base and the tissue mimicking gel*

Blood mimicking fluid

In order to simulate in vitro the complex properties of blood without the problems associated with handling real blood, a blood mimicking fluid (BMF) is usually used. Distilled water is used for simplicity in this work as BMF. Its dynamic viscosity equals 1 cP and its density equals 1.0 g/ml. the relaxation times T1 and T2 of the BMF at 1.5 Tesla are 3000 ms. Approximately 15 liters of fluid are needed in each experiment in order to adequately fill the reservoir and the tube system.

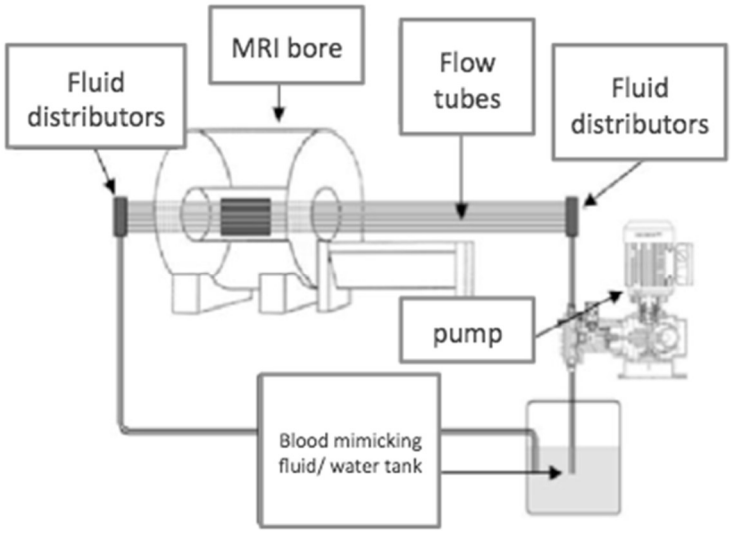

Fig.13 *Schematic diagram of the MRI flow phantom*

Experimental setup in the MR imaging room

The MR imaging system is a 1.5 Tesla scanner (Intera 1.5T, Philips Medical Systems, Best, the Netherlands), as mentioned above. The complete set-up can be seen in fig 14. The reservoir and the pump are mounted on a mobile wooden platform that is located approximately 3 meters away from the scanner to ensure absence of interference between the magnetic field (static or gradients) and the electronics of the pump. The wooden base with the stabilized tube is placed at the center of the scanner bore. Tissue equivalent medium in the form of gelatin is placed above and below the tube in order to achieve good MR signal strength. The tube is connected to the 2,5cm supply tubes through custom made adaptors to avoid fluid leakage. Finally, the main tube is connected to the two distributors, which are placed on either side of the MRI scanner bore as well as to the pump and the reservoir to ensure a closed circuit fluid circulation.

MR imaging

Flow measurements are performed with the use of gradient-echo phase contrast MR sequences with a magnetization-prepared phase-contrast gradient echo sequence with retrospective ECG gating. The SQ **flow** sequence parameters varied for each sequence. Parameters of the QFP sequence were: time Repetition (TR) =20 ms, Time Echo (TE) =6, 45 ms, Flip Angle (FA) =30, percentage FOV=84,375, Acquisition matrix=128x96, Slice Thickness (ST)=6mm, the Velocity Encoding (VENC)=100-200cm/s in AP (perpendicular to the imaged slice) direction (depending on the tubing considered). Images are then transferred to a workstation (ViewForum, Philips Medical Systems, the Netherlands) and analyzed with the flow evaluation software package.

The primary goal is to study the following parameters and characteristics of flow. Firstly the fact that all images do not present any artifact that could be attributed to any of the assembled components (collectors, tubing, wooden box, tissue equivalent material, BMF, stenosis etc.) is established. The next step includes the measurement of maximum flow velocity in each set-up (straight, inclined and stenotic tube), pump output, pulse rate selection, sequence and different ROIs, in order to establish the correct velocity encoding (VENC) parameter for the correct measurement of volume flow and to avoid aliasing effects. Additionally, besides maximum velocity and volume flow, mean flow velocity was recorded, for each set-up. Measurements are additionally carried out for inclined straight tube mounted at a stable angle of 18,58°.

Volume flow rate is measured and recorded concerning the straight tube, for 5%, 10% 20% of available pump outputs to ensure that a wide variety of set-ups can be simulated with accuracy and for ECG pulse rate of 60 and 75 bpm. Concerning the glass tube, a 10% pump output is used for 60, 75,100 and 120bpm flow rates. Various parameters are estimated. Of the latter are the pressure change across stenosis, the percentage of stenos is (co estimated by CT scanning), and

SNR in order to estimate the signal loss across the stenosis. The aforementioned results gave an indication of all the possible set-ups that can be simulated with the presented flow phantom.

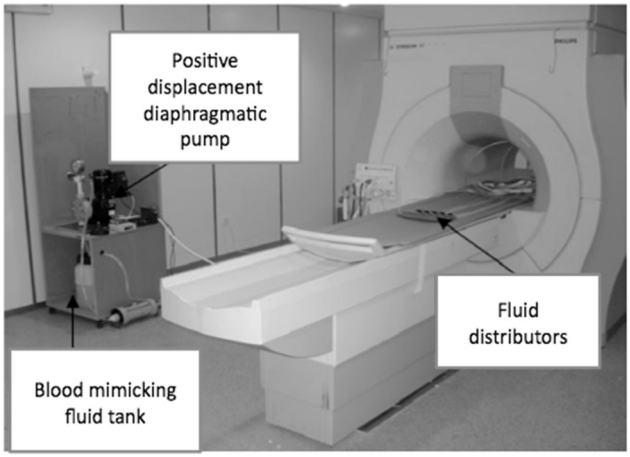

Fig.14 *the MRI flow phantom inside the MRI room*

4.2 Measurements: The process

Since we ensure an appropriate simulation of blood in arterial circulation; no leakage at point of component connections, maintenance of constant pump counter-pressure (relief valve) as monitored by an analog manometer, measurements are extracted. Perhaps at this point is important to mention that the smallest available subdivision to obtain for pump output, corresponds to 5% (as used later for the MRI values). All the aforementioned values for adjustments and the resulting measurements are noted as follows in the tables; by means of the aforementioned set up, measurements are then saved and extracted and processed as follows:

4.2.1 Volumetric VFR measurements of the straight tube

The first set of measurements concerns VFR values, measured volumetrically at regular intervals. A titration containerized was used and the flow was measured at time intervals of 15 seconds with a countdown timer. There are 20 values of VFR for each pump output and 6 different pump outputs for each pump rate. VFR values are calculated per second and then averaged. In this set up, the tube of PVC measuring of 6mm internal diameter is used (tape measured). In terms of the pulse rates, the latter are set to 60 and 75 bpm. The adjustment nob, provides various values of pump flow output; namely from 10% up to 60% per 10%.

4.2.2. MRI acquisitions and parameters calculation

For both tubes VFR values are obtained using elliptical ROIs and V_{max} values using both elliptical and linear ROIs. For the stenotic tube additional parameters are estimated as aforementioned and further analyzed later. The.

A) S<u>traight tube and inclined tube</u>: Concerning the first set of measurements, this relates to the plastic tube, in a straight and inclined position (18,75°). Pump outputs of 5%, 10%, 20% are used and pulse rates of 60 and 75 bpm. Two different PC sequences (SQflow and QFP in accordance to the protocol) are used only for the case of 20% pump output.

A.1) <u>Acquiring values from elliptical ROIs</u>:

Subsequently instituted for the MRI performed measurements, the sets of them are retracted via the database of EVORAD. EVORAD is an RIS-PACS accountancy program that enables the management of the patients' appointments. Via the database further study and processing of examinations is available. Thus, after searching for the examination namely, the icon named "images" is selected. Afterwards, the phase contrast sequence is selected and uploaded using the "process" icon. As mentioned above, velocity encoded MRI scan provides two sets of images for each time point in the cardiac cycle. An anatomical image and an image where the signal intensity in each pixel is directly proportional to the through-plane velocity. Thus, the process continues with the identification and definition of the region of interest ROIs (elliptical), on the anatomical images. In particular, the image of maximum systole is chosen. Anatomical images have higher spatial resolution providing better definition of ROI, i.e. including the vessel lumen, and excluding the vessel wall. In this way, each ROI is designed in the borders of vessel flow. It is important that the cross section is perpendicular to the vessel so as the vessel to be imaged as circular. A bigger or smaller vessel would attribute to poor flow estimation.

Pettigrew et al.(1987), in their study they report significant errors in the measurement of flow in vessels oblique to the image plane. To determine the relative accuracy and practicality of quantitatively measuring flow in oblique vessels, they used standard sequence gradients with (i) routine orthogonal plane imaging and (ii) direct compound oblique plane imaging. Phantom studies of flow in a vessel aligned along the z axis showed a significant linear correlation ($r = .999$; $p < .05$) between the spin phase and spin velocity. The flow phantom was a plastic tube with an inside diameter of 0.9 cm through which distilled water doped with copper sulfate (0.7 g/l) was gravity driven at variable rates.

Volumetric flow rates were determined from timed collections in a graduated cylinder. Studies of flow at relatively low physiologic rates (12-17 cm/s) in vessels angled 0-30° off axis showed that obliquities of as little as 10° resulted in significant quantification errors (profile showed irregular phase distribution, skewed, and inconsistent with laminar flow). Error in calculation of flow velocity from this image was 50%. At 20° obliquity, prominent phase-image irregularities were readily apparent and graphically depicted by phase profile. With this degree of tube obliquity, effects of in-plane flow and intravoxel phase variation were more significant, yielding a phase image from which neither in-plane nor through-plane flow components to be

retrieved. The error was attributed to a larger phase shift per unit velocity along the frequency-encoding direction vs along the slice-select direction and to a mixture of velocities within a voxel that is oblique to the flow direction. Electronic plane rotation with compound oblique angulation, resolve these errors so that the image plane and vessel are perpendicular.

The acquired images extracted from EVORAD, provide statement of sequences parameters (TE, TR, FA, slice thickness, slice separation, acquisition matrix, FOV). Provided that the ROI is accurately defined, it is then transferred on the corresponding phase contrast image (image of flow). Measurements are performed during the time of a cardiac cycle, by a 25msec of interval, so a number of 120 images are acquired. The software of the workstation automatically provides the following parameters: ROI area (cm^2), vessel lumen diameter (cm), blood volume flow (ml/s), mean and maximum blood flow velocities (cm/s). Data is then extracted to Excel files including: in sequence: series, image, acquisition time, trigger time, TE, TR, V_{min}, $V_{max,}V_{mean}$, standard deviation, variance, area and volume. Blood flow **VFR** is then calculated by multiplying mean velocity times area for each table value. Integration over the cardiac cycle for VFR follows.

In addition, for velocity profiles the maximum value among Vmax values, lead to the respective anatomical image for the LOIs design. The LOI is then copied to the velocity images. The latters result in data concerning the plot of the velocity profile. The procedure is shown in figures 14a,b.

A.2) Acquisitions from lines of interest (LOIs):

After uploading the set of images for each sequence, a linear line of interest (LOI) is manually defined on the anatomical image. The definition of Line of Interest (LOI) on the selected images is performed by means of the ImageJ software. the definition of the anatomical image proceeds. This is the image corresponding to the velocity image of highest maximum value. The LOI is taken as a linear ROI drawn across the tube on the magnitude image and is then transferred on the corresponding phase contrast velocity image. In order to obtain the velocity values in units of cm/s the rescale slope is used and rescale intercept values provided by the appropriate DICOM image header tags that in the particular case of phase contrast images correlate pixel intensity values to velocity values. The pixels of the lumen are chosen at each LOI and the corresponding velocity values are extracted. Using the obtained velocity profiles, a parabolic curve is fitted. The curve is described by a polynomial function of the form $V= ar^2 + br + c$. The latter procedure is shown in fig.14b.

B) **Stenotic tube:** In this case the glass tube of 8mm inner diameter is used. The pump output is maintains constant to 10%**,** whereas pulse rates range in 60, 75, 100, and 20 bpm. MRI scans are performed at in plane and transverse direction to the tube. Towards the aim of the flow estimation across the stenos is in regard to the position, images are acquired at transverse scans of

1cm step, upstream and downstream the stenosis, reaching up to 4cm at each side. Transverse scans provide the VFR and Vmax estimations, whereas inplane to the SNR estimation.

B.1) Measurements of **VFR** and $\mathbf{V_{max}}$ are obtained as aforementioned for the straight tube, devoided of any changes in the procedure. LOIs provide the velocity profile across the stenosis for qualitative and quantitative estimation of flow, thus estimation of the profile's variation across the stenosis compared to the ideal parabolic.

B.2) The severity of stenosis (percentage of stenosis) is calculated as the percentage result of the pre and post stenosis V_{max} to $V_{max\ in\ stenosis}$ ratio, minus the unity. Four values are acquired for each region-line of interest per bpm, resulting in 12 values.

B.3) **In plane acquisitions:**

This procedure has the purpose to estimate the signal loss in accordance to the BMF flow across the stenosis. At first, the in plane images are uploaded in EVORAD. Then, a rectangular ROI is manually designed at the anatomical images. Data is then extracted to Excel files as mentioned above. After identifying the image of maximum flow, the corresponding anatomic image is defined. The later provides the values of mean and standard deviation intensity. By dividing those values, **SNR** is defined.

CT scan measurement:

The percentage of the stenosis is also calculated by the images resulting from CT scans. The CT imaging system is a Philips Brilliance 64. Imaging parameters are as follows: slice thickness: 2mm, kVp: 120, spacing between slices: 1, matrix:512x512 and resolution: 10,240 pixels/mm. Procedure includes the uploading of CT images in ImageJ program and the choice of images corresponding to the maximum tube area upstream and downstream the stenosis and also to the minimum area at the center of stenosis. Elliptical and linear ROIs are designed and information concerning length ant tube area are extracted. Elliptical ROIs provide values of the lumen area, thus lead to calculation of area stenosis, calculated as the ratio of areas upstream (or downstream) the stenosis to the area in the stenosis minus the unity. Lines of interest LOIs provided respectively the percentage of diameter stenosis.

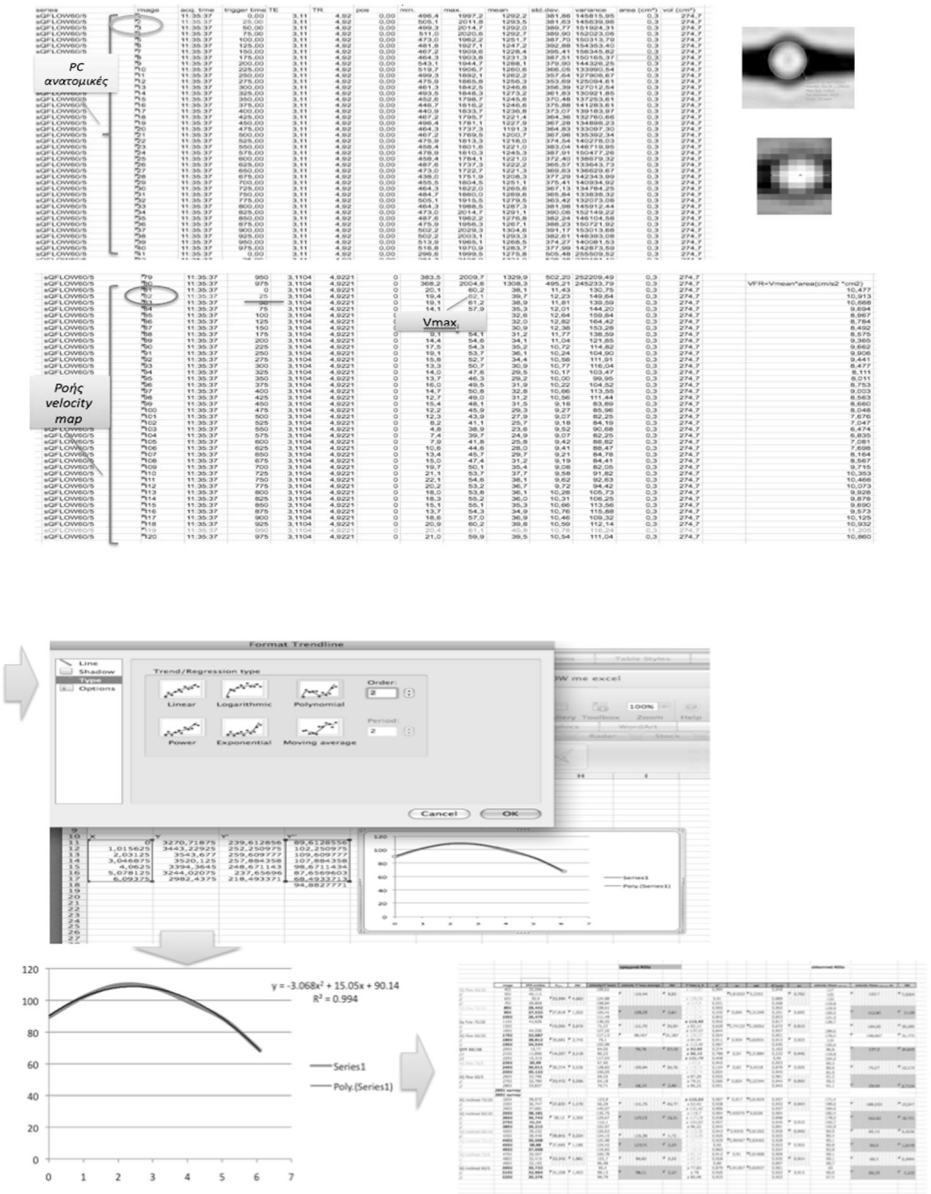

Fig.15 *Process for Vmax estimation using linear ROIs*

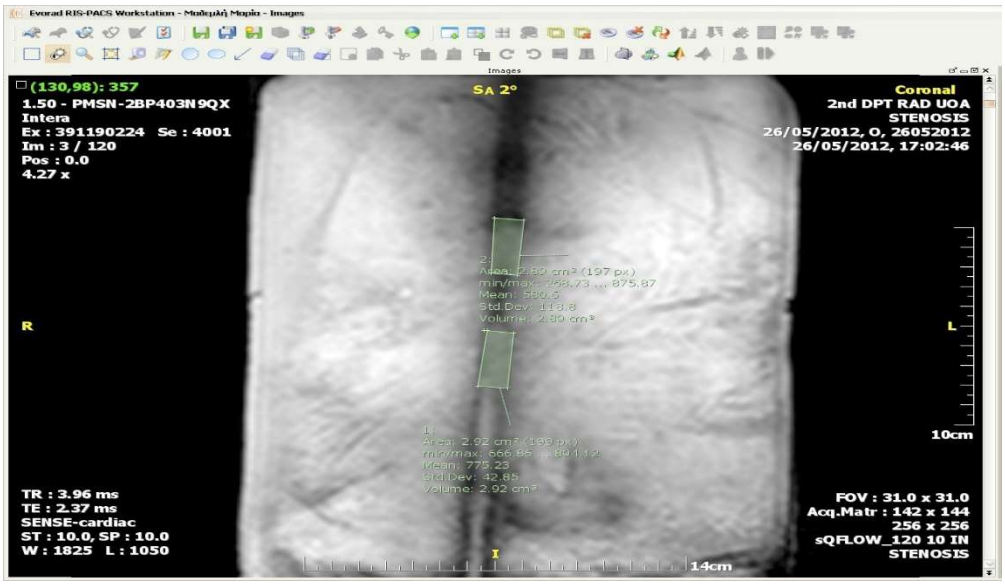

Fig16. *Image in EVORAD showing rectangular ROIs designed upstream and downstream of the stenosis*

CHAPTER 5

IN VIVO RESULTS

5.1 Tabulated results of WSS values in the arterial tree using PC-MRI

The calculated WSS values at various sites of the arterial tree are tabulated in Tables1 and 2. The results are ordered according to the vessel studied. For each study the exact location and method of WSS measurement are stated. The measured values of WSS that are tabulated are the mean WSS over the entire cardiac cycle and the maximum (systolic) and minimum (diastolic) WSS values. Only studies performed on healthy humans where included since vascular disease frequently results at remodeling of the affected arteries that leads to alterations of the physiological WSS values.

Vessel	Study	Measurement location	WSS calculation method	Measured value of WSS (N/m^2)		
				Mean	Max / Systolic	Min / Diastolic
Carotid artery	Oyre et al (1998)	2 cm below the carotid bifurcation	Three dimensional paraboloid (3DP)	0.95 (0.67-1.29)	2.56 (1.82-3.29)	0.63 (0.38-0.93)
			Hagen-Poiseuille formula	0.78 (0.49-1.02)	1.71 (1.46-2.04)	0.56 (0.35-0.82)
	Masaryk et al (1999)	Cervical segment of the internal carotid artery	Quadratic extrapolation (QE)	0.81	1.32	
	Wu et al (2004)	1.4 cm upstream of the flow divider	Three dimensional paraboloid (3DP)	1.02 ± 0.22	2.80 ± 0.53	0.14 ± 0.27
	Wu et al (2004)	3 cm upstream of the flow divider	Three dimensional paraboloid (3DP)	1.17 ± 0.21	3.32 ± 0.43	0 .41 ± 0.38
	Stokholm et al (2004)	Flow divider and the lateral wall of the carotid artery bifurcation.	Three dimensional paraboloid (3DP	3.10 ± 0.67 (flow divider) 0.24 ± 0.16 (lateral wall)		
	Oshinski et al (2006)	1 cm below the carotid bifurcation	Hagen-Poiseuille formula	0.80 ± 0.41		
Femoral artery	Wu et al (2004),	3 cm downstream of the common femoral artery bifurcation	Three dimensional paraboloid (3DP)	0.46 ± 0.20	2.58 ± 0.51	-0.79 ± 0.27
	Silber et al (2005)	Femoral artery	Two dimensional parabolic fit		1.3 ± 0.3	
	Amann-Vesti et al (2004)	15cm distal to the femoral bifurcation	Simplified three dimensional paraboloid (3DP)		1.88 ± 0.34	
Brachial artery	Wu et al (2004)	6 cm above the elbow trochlea humerus	Three dimensional paraboloid (3DP	0.68 ± 0.35	3.20 ± 0.68	-0.28 ± 0.52
	Silber et al (2005)	Brachial artery	Two dimensional parabolic fit		1.2 ± 0.4	

Table 1 *WSS values measured at different parts of the arterial tree*

Vessel	Study	Measurement location	WSS calculation method	Measured value of WSS (N/m^2)					
				Mean		Max / Systolic		Min / Diastolic	
Aorta (abdominal)	Oshinski et al (1995)	suprarenal above renal ostia	Linear extrapolation with wall correction	1.04±0.29 Posterior wall (P)	0.86±0.32 Anterior wall (A)	5.4±1.1 (P)	4.8±0.6 (A)	-0.23 ±0.23 (P)	-0.43 ±0.45 (A)
		infrarenal aorta 2 cm below renal ostia		0.47±0.26 (P)	0.61±0.26(A)	3.0±0.7 (P)	3.3±1.1 (A)	-0.75±0.29 (P)	-0.69±0.4 (A)
	Oyre et al (1997)	suprarenal aorta 1.5 cm above celiac trunk	Linear extrapolation with wall correction	0.71±0.02 (P)	0.54±0.02 (A)	4.3 ± 0.64 (P)	3.84±0.25 (A)	-0.46 ±0.02 (P)	-0.96 ±0.27(A)
		infrarenal aorta 3.5 cm below celiac trunk		0.18 ±0.00(P)	0.38±0.00 (A)	2.54 ±0.15 (P)	2.90±0.10 (A)	-1.25 ±0.06 (P)	-0.76 ±0.09 (A)
	Pedersen et al (1999)	suprarenal aorta	Linear extrapolation with wall correction	0.62		4.11		-0.71	
		infrarenal aorta		0.27		2.69		-1.07	
	Cheng et al (2002)	immediately superior to the celiac artery supraceliac	Lagrangian polynomials	0.34		N.A		N.A.	
		immediately inferior to the renal arteries infrarenal	Lagrangian polynomials	0.23		N.A		N.A	
	Taylor et al (2002)	supraceliac	Lagrangian polynomials	**During rest (mean)** 0.35 ±0.08			**During exercise (mean)** 0.62 ±0.05		
		infrarenal	Lagrangian polynomials	**During rest (mean)** 0.13 ±0.06			**During exercise (mean)** 0.52±0.13		
	Cheng et al (2002)	supraceliac	Lagrangian polynomials	**During rest (Men-mean)** 0.36±0.09	**During exercise (Men-mean)** 0.72±0.05	**During rest (Women-mean)** 0.34±0.07	**During exercise (Women-mean) 0.61±0.04**		
		infrarenal	Lagrangian polynomials	**During rest (Men-mean)** 0.12±0.05	**During exercise (Men-mean)** 0.51±0.08	**During rest (Women-mean)** 0.14±0.07	**During exercise (Women-mean) 0.54±0.21**		
	Cheng et al (2003)	supraceliac	Lagrangian polynomials	**During rest (mean)** 0.20±0.07			**During exercise (mean)** 0.73±0.24		
		infrarenal	Lagrangian polynomials	**During rest (mean)** 0.14±0.08			**During exercise (mean)** 1.65±0.51		
Aorta (Thoracic)	Wentzel et al (2005)	Thoracic aorta	2D velocity field derivative	0.36±0.17		0.79		-0.05	

Table 2 *WSS values measured at different segments of the aorta*

5.2 Wall shear stress calculation in the human ascending aorta

In order to validate the applicability of the Hagen-Poiseuille expressions for WSS calculation we had to evaluate the shape of the derived velocity profiles by parabolic fitting. Table 3 shows the corresponding values of the coefficient of determination (R^2) derived by the application of parabolic fit on blood velocity values for each patient, which is a quantitative measure of the goodness of the parabolic fit. It can be derived by the resulted R^2 values that the experimental velocity data distribution is described by a parabolic curve of the form $u = ar^2 + br + c$. All 20 patients presented parabolic blood velocity distributions with R^2 ranging from 0.65 to 0.97 with an average value of 0.83, yielding a fairly good agreement with the predictions of the fluid dynamics theory concerning laminar flow at straight tubes under steady (non-pulsatile) conditions.

Figure 17 presents the four parabolic fits for one of the patients. From Figure 17 it is evident that the interpolating parabolic curves do not reach the zero values at the vessel wall positions as expected by theory. This is because the aortic vessel wall is not stationery due to cardiac and, to a lesser extent, respiration motion. This effect could have been corrected by applying a background phase correction technique. However this was not possible since we retrospectively evaluated aortic flow from patients that underwent cardiac MRI examination.

Table 4 shows the obtained systolic WSS values calculated by all four methods. The average systolic WSS values for all study group were the following:: 4.04 ± 2.35 dynes/cm^2 using the average flow method (AFM), 4.17 ± 2.59 dynes/cm^2 using the average velocity method (AVM), 4.24 ± 1.82 dynes/cm^2 using the maximum velocity method (MVM) and 3.52 ± 1.71 dynes/cm^2 using the linear method (LM).

The intra-class correlation coefficient (ICC) was used to estimate the reliability among the four different methods for measuring WSS at ascending aorta. Comparing the agreement of all methods simultaneously, we observed that ICC was 0.782 (95% CI: 0.628, 0.894, $p<0.001$). Thereinafter, we calculated ICC for all possible combinations of 4 methods (Table 5). We observed that ***all methods are in statistical agreement with each other***.

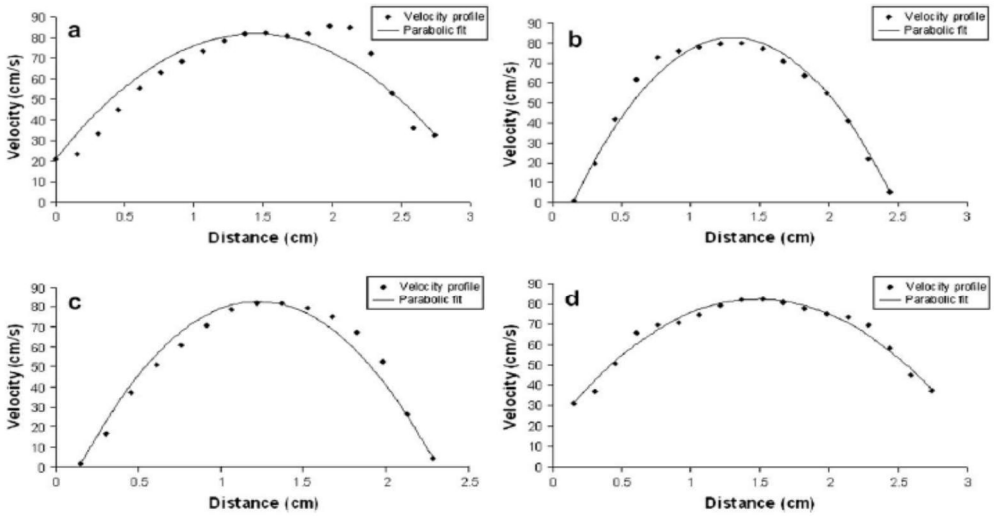

Figure 3 Parabolic fitting of blood velocity measurements inside the ascending aorta for one of the patients for the four directions mentioned in Fig. 2. The coefficient of determination (r^2) for each direction are: (a) $r^2 = 0.89$, (b) $r^2 = 0.98$, (c) $r^2 = 0.97$, and (d) $r^2 = 0.97$.

Figure 17. *'Example of a parabolic fit to a blood velocity 2D map in four directions'*.

Table 3. *'Coefficient of determination (r^2) for all velocity profiles'.*

Patient	0-180	90-270	45-225	135-315	Average
1	0.93	0.98	0.98	0.98	0.97
2	0.94	0.98	0.96	0.98	0.96
3	0.89	0.94	0.92	0.80	0.89
4	0.78	0.94	0.68	0.87	0.82
5	0.57	0.92	0.80	0.66	0.74
6	0.45	0.85	0.91	0.91	0.78
7	0.65	0.67	0.69	0.58	0.65
8	0.80	0.74	0.82	0.65	0.75
9	0.94	0.89	0.91	0.86	0.90
10	0.83	0.88	0.67	0.86	0.81
11	0.97	0.95	0.92	0.77	0.90
12	0.90	0.95	0.92	0.88	0.91
13	0.80	0.96	0.96	0.93	0.91
14	0.87	0.72	0.78	0.71	0.77
15	0.90	0.93	0.85	0.77	0.87
16	0.78	0.86	0.82	0.78	0.81
17	0.77	0.70	0.66	0.58	0.67
18	0.72	0.57	0.64	0.77	0.68
19	0.87	0.96	0.95	0.91	0.92
20	0.96	0.94	0.93	0.77	0.90

Table 4. *'Overall comparison of calculated wall shear stress values in the ascending aorta using four methods (dynes/cm^2)'.*

	Method			
Patient	Linear Method (LM)	Average Flow Method (AFM)	Average Velocity Method (AVM)	Maximum Velocity Method (MVM)
1	2.11	3.69	3.50	4.25
2	4.02	3.54	3.97	5.27
3	2.79	1.54	1.62	4.00
4	2.52	3.68	4.38	5.26
5	1.39	3.06	3.15	2.20
6	2.63	4.17	4.59	2.88
7	1.82	2.44	2.14	2.42
8	2.97	2.81	3.07	2.39
9	6.00	7.11	7.06	6.43
10	6.53	9.35	11.04	8.18
11	4.60	4.88	4.56	7.09
12	3.68	2.15	1.99	5.27
13	4.82	5.24	4.68	4.13
14	2.37	1.98	2.22	2.58
15	1.23	1.42	1.38	1.73
16	4.08	3.68	3.75	2.78
17	5.06	2.28	2.47	3.57
18	7.09	9.98	10.39	6.34
19	1.92	3.11	3.42	2.87
20	2.74	4.17	4.03	5.18
Average	3.52	4.01	4.17	4.24

Table 5. *Intra-class correlation coefficients for all possible combinations of 4 methods per two*.

	LM	AFM	AVM
AFM	0.76 (0.49, 0.90)		
AVM	0.72 (0.42, 0.88)	0.98 (0.96, 0.99)	
MVM	0.75 (0.45, 0.89)	0.71 (0.41, 0.88)	0.69 (0.37, 0.86)

Intra-class correlation coefficient p-value was <0.001.

5.3 Wall shear stress calculation in the human ascending aorta throughout the cardiac cycle

WSS values were calculated using Equations (?) to (?) and the systolic, diastolic, minimum and maximum WSS values were computed. The same blood flow pattern in the ascending aorta during an R-R interval was exhibited for all patients. Maximum blood flow volume was observed at maximum systole, followed by a rapid fall in the cardiac output as shown in Figure ? The variation of WSS throughout the cardiac cycle for a single patient as calculated with the three methodologies is shown in Figure ?. Figure 3

Systolic WSS values are presented in Table ?. No statistically significant difference was observed between the AF, AV and MV methods (p= 0.95) with average values equal to 0.401 ± 0.235, 0.417 ± 0.259 and 0.424 ± 0.182 $\frac{N}{m^2}$ respectively.

Diastolic WSS values (Table ?) showed no statistically significant difference when calculated with the AF (WSS=0.003 ± 0.009 $\frac{N}{m^2}$) and the AV (WSS=0.003 ± 0.010 $\frac{N}{m^2}$) methods, but comparison with MV (WSS=0.116 ± 0.070 $\frac{N}{m^2}$) revealed significant differences ($p<0.0001$).

Maximum WSS values (table ?) showed no statistically significant difference when calculated with the AF (WSS=0.411 ± 0.233 $\frac{N}{m^2}$) and the AV (WSS=0.417 ± 0.245 $\frac{N}{m^2}$) methods, but comparison with MV (WSS=0.563 ± 0.140 $\frac{N}{m^2}$) revealed significant differences ($p=0.04$).

Minimum WSS values (table V) showed no statistically significant difference when calculated with the AF (WSS=-0.047 $\pm$0.042 $\frac{N}{m^2}$) or AV (WSS=-0.047 $\pm$0.042 $\frac{N}{m^2}$) method, but large differences ($p<0.0001$) were observed compared with the MV (WSS=0.062 $\pm$0.022 $\frac{N}{m^2}$) method.

OSI was calculated for the derived WSS values throughout the cardiac cycle obtained by the three methodologies (Table ?). Average OSI values for all patients were identical for AF and AV methods (0.098 $\pm$0.070 and 0.101 $\pm$0.070 respectively) while for MV method was higher (0.319 $\pm$ 0.100). ANOVA statistical tests showed no significant statistical difference between the AF and the AV method ($p= 0.07$). Comparison of the OSI values between the AF and AV with MV showed statistically significant differences ($p<0.001$ and $p<0.001$ respectively).

Comparison of peak systole WSS and maximum WSS values reveals that with the AF and AV methods maximum WSS values are obtained at the moment of peak systole ($p=0.18$ and $p=0.96$ respectively), whereas MV method shows different results between peak systole WSS and maximum WSS ($p<0.0001$). This implies that maximum WSS is not found at peak systole when the MV method is applied.

Additionally, when comparing end-diastole WSS with minimum WSS, results vary regardless of the method ($p<0.0001$ for the AF, $p<0.0001$ for AV and $p<0.0001$ for MV); this fact is seen in the averaged WSS values in tables ? and ?.

Table 6. *The degree of agreement among the four measurements of diastolic and systolic diameter was evaluated using intra-class correlation coefficient (ICC).*

Measure	Direction 1	Direction 2	Direction 3	Direction 4	ICC	p
Diastolic diameter (cm)	2.98±0.63	3.04±0.62	3.16±0.70	3.04±0.598	0.920	<0.001
Systolic diameter (cm)	3.51±0.69	3.50±0.65	3.61±0.68	3.48±0.65	0.953	<0.001

Data are presented as mean±standard deviation

Table 7. *Systolic WSS for twenty patients using three methodologies*

Patient	AF (N/m^2)	AV (N/m^2)	MV (N/m^2)
1	0.369	0.350	0.425
2	0.354	0.397	0.527
3	0.154	0.162	0.400
4	0.368	0.438	0.526
5	0.306	0.315	0.220
6	0.417	0.459	0.288
7	0.244	0.214	0.242
8	0.281	0.307	0.239
9	0.998	1.039	0.634
10	0.711	0.706	0.643
11	0.935	1.104	0.818
12	0.488	0.456	0.709
13	0.215	0.199	0.527
14	0.524	0.468	0.413
15	0.198	0.222	0.258
16	0.311	0.342	0.287
17	0.417	0.403	0.518
18	0.142	0.138	0.173
19	0.368	0.375	0.278
20	0.228	0.247	0.357
Average	0.401	0.417	0.424

AF: Average Flow**, AV:** Average Velocity**, MV:** Maximum Velocity

Table 8. *Diastolic WSS for twenty patients using three methodologies*

Patient	AF (N/m^2)	AV (N/m^2)	MV (N/m^2)
1	-0.005	-0.005	0.060
2	-0.013	-0.015	0.266
3	0.000	0.000	0.035
4	-0.008	-0.009	0.080
5	0.002	0.002	0.074
6	0.002	0.003	0.103
7	0.002	0.002	0.209
8	0.015	0.015	0.119
9	-0.012	-0.012	0.181
10	0.008	0.010	0.109
11	0.000	-0.001	0.222
12	0.001	0.000	0.042
13	0.001	0.001	0.036
14	0.000	0.001	0.125
15	-0.012	-0.013	0.094
16	0.019	0.019	0.084
17	0.008	0.007	0.244
18	0.021	0.019	0.087
19	0.008	0.012	0.043
20	0.013	0.013	0.112
Average	0.003	0.003	0.116

AF: Average Flow**, AV:** Average Velocity**, MV:** Maximum Velocity

Table 9. *Maximum WSS for twenty patients using three methodologies*

Patient	AF (N/m^2)	AV (N/m^2)	MV (N/m^2)
1	0.384	0.383	0.721
2	0.358	0.396	0.656
3	0.155	0.164	0.408
4	0.386	0.438	0.574
5	0.348	0.305	0.469
6	0.484	0.442	0.655
7	0.345	0.294	0.373
8	0.293	0.307	0.549
9	0.996	0.923	0.778
10	0.716	0.752	0.644
11	0.939	1.098	0.818
12	0.487	0.416	0.709
13	0.206	0.219	0.537
14	0.513	0.492	0.476
15	0.200	0.221	0.479
16	0.326	0.316	0.560
17	0.397	0.354	0.684
18	0.146	0.136	0.429
19	0.319	0.438	0.310
20	0.223	0.241	0.441
Average	0.411	0.417	0.563

AF: Average Flow**, AV:** Average Velocity**, MV:** Maximum Velocity

Table 10. *Minimum WSS for twenty patients using three methodologies*

Patient	AF (N/m^2)	AV (N/m^2)	MV (N/m^2)
1	-0.007	-0.007	0.049
2	-0.040	-0.044	0.104
3	-0.027	-0.028	0.035
4	-0.034	-0.038	0.046
5	-0.029	-0.027	0.060
6	-0.063	-0.062	0.061
7	-0.067	-0.057	0.078
8	-0.028	-0.027	0.086
9	-0.073	-0.075	0.063
10	-0.028	-0.023	0.049
11	-0.051	-0.066	0.070
12	-0.020	-0.019	0.042
13	-0.027	-0.027	0.033
14	-0.052	-0.047	0.082
15	-0.076	-0.080	0.022
16	-0.024	-0.023	0.084
17	-0.033	-0.027	0.085
18	-0.207	-0.202	0.087
19	-0.004	-0.006	0.033
20	-0.053	-0.059	0.064
Average	-0.047	-0.047	0.062

AF: Average Flow**, AV:** Average Velocity**, MV:** Maximum Velocity

Table 11. *OSI in the R-R- interval for twenty patients using three methodologies*

Patient	AF	AV	MV
1	0.003	0.003	0.185
2	0.077	0.077	0.436
3	0.106	0.106	0.212
4	0.046	0.045	0.261
5	0.118	0.130	0.294
6	0.060	0.067	0.300
7	0.063	0.061	0.473
8	0.219	0.217	0.332
9	0.023	0.024	0.377
10	0.054	0.058	0.316
11	0.018	0.019	0.437
12	0.018	0.013	0.157
13	0.102	0.115	0.192
14	0.051	0.057	0.377
15	0.180	0.181	0.403
16	0.185	0.190	0.252
17	0.102	0.099	0.465
18	0.229	0.230	0.266
19	0.100	0.118	0.294
20	0.214	0.209	0.355
Average	0.098	0.101	0.319

AF: Average Flow**, AV:** Average Velocity**, MV:** Maximum Velocity

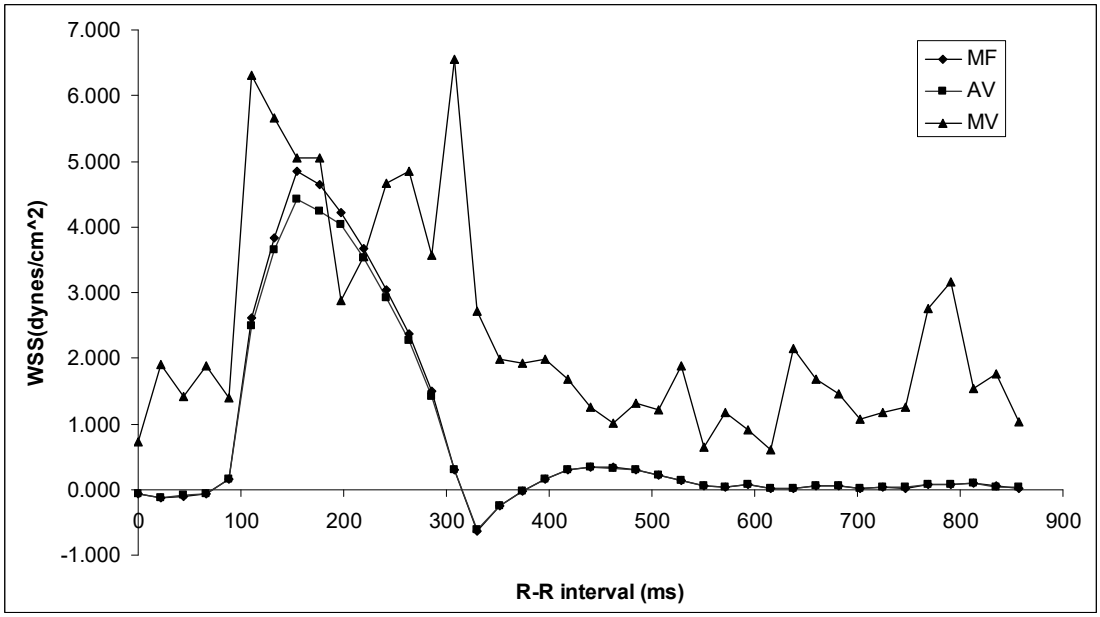

Figure 18 '*Blood flow as a function of time (a) and WSS variation within the R-R interval using the three methodologies'.*

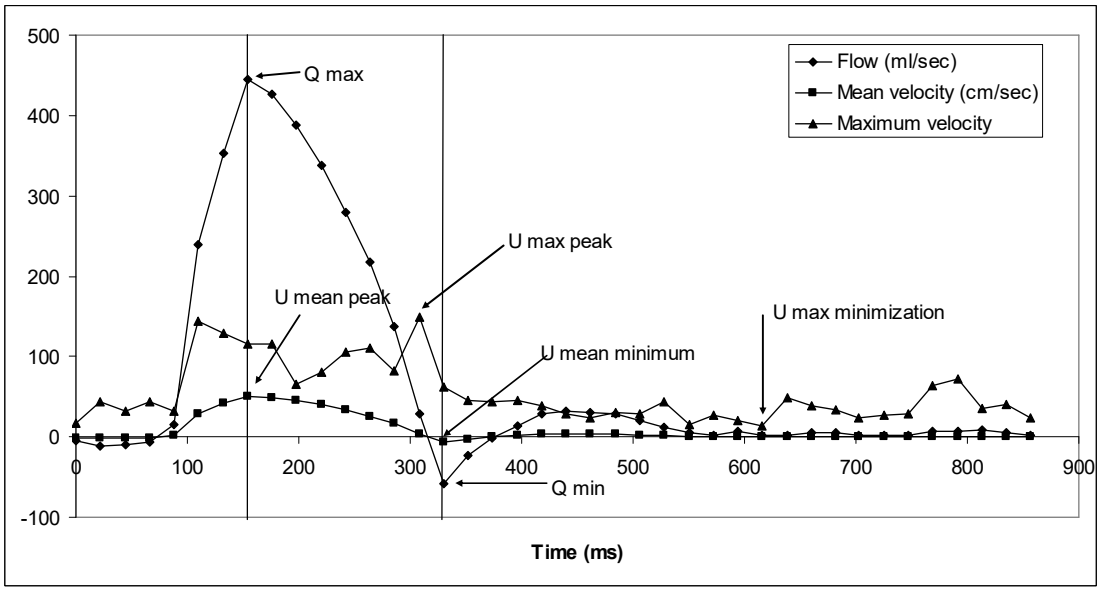

Figure 19. '*Temporal distribution of peak and minimum values for flow, mean velocity and max velocity* Q_{max} *and* Q_{min} *is the maximum and minimum flow throughout the heart cycle.* $U_{peak\ ave}$*, is defined as the temporal peak value of average velocity.* $U_{min\ ave}$*, is the temporal minimum value of average velocity.* $U_{peak\ max}$*, is the temporal peak value of the maximum velocity.* $U_{min\ max}$*, is the temporal minimum value of the maximum velocity.'*

CHAPTER 6

IN VITRO RESULTS

6.1.1 Volumetric volume flow rate (VFR) values

VFR values as obtained volumetrically for each pump output and 6 different pump outputs for each pump rate.

Twenty values of VFR are averaged per set of bpm and pump output:

f= 60bpm	P=2,5b 10%	P=3,3b 20%	P=3,7b 30%	P=4,2b 40%	P=4,4b 50%	P=4,6b 60%
	VFR(ml/s)	VFR(ml/s)	VFR(ml/s)	VFR(ml/s)	VFR(ml/s)	VFR(ml/s)
Average	11,52	19,28	22,97	26,73	29,55	32,77
St.Deviation	0,49	0,42	0,26	0,61	0,47	0,73
Cv%	4,25	2,19	1,14	2,27	1,61	2,22

Table 12. *'**VFR volumetric** results for 6mm straight tube, measured at 10%, 20%, 30%, 40%, 50% and 60% of pump output for 60 bpm pump rate'*

f= 75bpm	P=2,5b 10%	P=3,3b 20%	P=3,7b 30%	P=4,2b 40%	P=4,4b 50%	P=4,6b 60%
	VFR(ml/s)	VFR(ml/s)	VFR(ml/s)	VFR(ml/s)	VFR(ml/s)	VFR(ml/s)
Average	16,03	20,83	25,33	29,65	33,03	36,13
St.Deviation	0,40	0,48	0,37	0,33	0,51	0,60
Cv%	2,51	2,29	1,48	1,12	1,53	1,65

Table. 13*. 'VFR volumetric** results for 6mm straight tube, measured at 10%, 20%, 30%, 40%, 50% and 60% of pump output for 75 bpm pump rate'.*

6.1.2 Straight and oblique tube

A) VFR values

	VFR MRI (ROIs)			
	Straight tube		Inclined tube	
	60 bpm	75 bpm	60 bpm	75 bpm
PO	VFR (ml/s)	VFR (ml/s)	VFR (ml/s)	VFR (ml/s)
5	9,662 ± 0,49	8,932 ± 0,8	10,754 ± 0,13	11,06 ± 0,46
10	10,139 ±0,28	22,542± 10,34	13,614 ± 0,06	14,171 ± 0,216
20	14,049 ±0,17	15,732 ± 2,44	15,177 ± 1,1	16,544 ± 0,42
20 (QFP)	16,896 ± 0,61			

	VFR volumetric	
	60 bpm	75 bpm
PO	VFR (ml/s)	VFR (ml/s)
10	11,52 ± 0,49	16,03 ± 0,4
20	19,28 ± 0,42	20,83 ± 0,48

Table 14. *'**VFR** values: comparison of MR (**ROI**) values vs VFR **volumetric** values, for 6mm tube in both straight and inclined position, at 60, 75 bpm, PO: 5, 10, 20%'.*

B) Vmax values

	Vmax MRI (ROIs)				Vmax MRI (LOIs H)				Vmax MRI (LOIs V)			
	Straight tube		Inclined tube		Straight tube		Inclined tube		Straight tube		Inclined tube	
	60 bpm	75 bpm	60 bpm	75 bpm	60 bpm	75 bpm	60 bpm	75 bpm	60 bpm	75 bpm	60 bpm	75 bpm
PO	Vmax (cm/s)	Vmax (cm/s)	Vmax (cm/s)	Vmax (cm/s)	Vmax (cm/s)	Vmax (cm/s)	Vmax (cm/s)	Vmax (cm/s)	Vmax (cm/s)	Vmax (cm/s)	Vmax (cm/s)	Vmax (cm/s)
5	61,3 ±1,44	82,8 ±12,24	68,2 ±2,49	69,1 ±0,35	50,38 ±3,71	72,72 ±13,81	65,19 ±2,64	96,98 ±19,65	56,53 ±2,55	78,27 ±12,66	62,9 ±2,02	63,49 ±0,57
10	122,5 ±6,99	123 ±13,15	85,3 ±0,14	85,8 ±1,06	109,12 ±67,25	112,8 1±13,55	103,01 ±29,9	80,9 ±0,76	113,2 ±7,41	105,69 ±14,68	80,02 ±0,7	78,96 ±1,08
20	156,2 ±31,84	169,75 ±28,07	166,5 ±19	194,6 ±13,12	136,04 ±28,11	128,43 ±1,57	161,25 ±33,99	160,7 ±24,26	147,9 ±28,22	144,79 ±46,02	158,6 ±18,76	185,91 ±15,49
20 (QFP)	116,8 ±34,53				106,96 ±15,44				112,66 ±33,07			

Table 15. ***Vmax** values extracted from MRI: a) elliptical **ROIs,** b) **LOIs** vertical, c) **LOIs** horizontal), for 6mm tube in both straight and inclined position, at 60, 75 bpm, PO: 5,10,20%.*

C) R^2 values

	R^2 (ROIs H)			
	Straight tube		Inclined tube	
	60 bpm	75 bpm	60 bpm	75 bpm
PO	R^2	R^2	R^2	R^2
5	0,933 ±0,025	0,894 ±0,16	0,902 ±0,05	0,903 ±0,05
10	0,919 ±0,23	0,761 ±0,11	0,929 ±0,004	0,824 ±0,26
20	0,839 ±0,04	0,477 ±0,24	0,874 ±0,08	0,906 ±0,11
20 (QFP)	0,713 ±0,18			

	R^2 (ROIs V)			
	Straight tube		Inclined tube	
	60 bpm	75 bpm	60 bpm	75 bpm
PO	R^2	R^2	R^2	R^2
5	0,979 ±0,01	0,955 ±0,17	0,908 ±0,02	0,918 ±0,004
10	0,972 ±0,01	0,942 ±0,04	0,91 ±0,06	0,926 ±0,01
20	0,954 ±0,01	0,848 ±0,12	0,892 ±0,02	0,957 ±0,12
20 (QFP)	0,931 ±0,1			

Table 16. ' ***R^2*** *values extracted from MRI profiles:* ***LOIs*** *a) vertical, b) horizontal, for 6mm tube in both straight and inclined position, at 60, 75 bpm, PO: 5,10,20%.'*

D) Velocity profiles for straight and inclined tube:

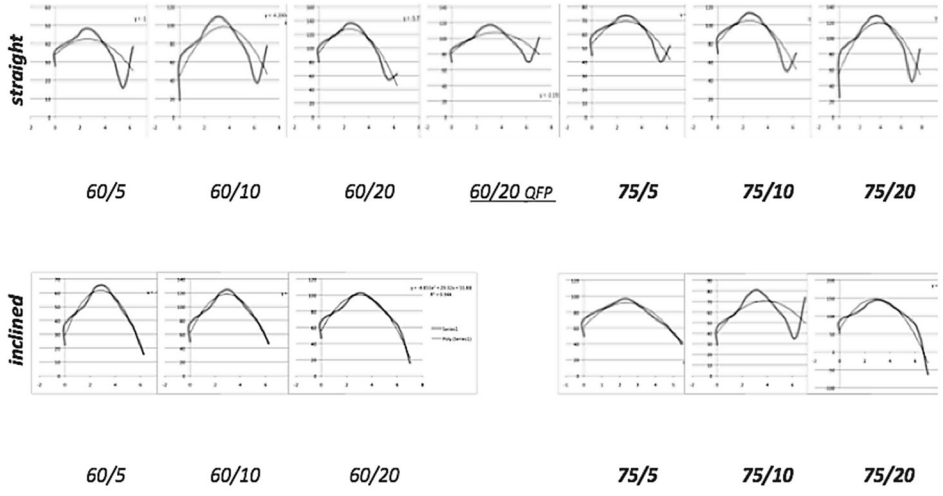

Fig 20*.' Velocity profiles from* ***LOIsH****, for* ***straight*** *and* ***inclined*** *tube at 60, 75 bpm and 5, 10, 20% pump output'*

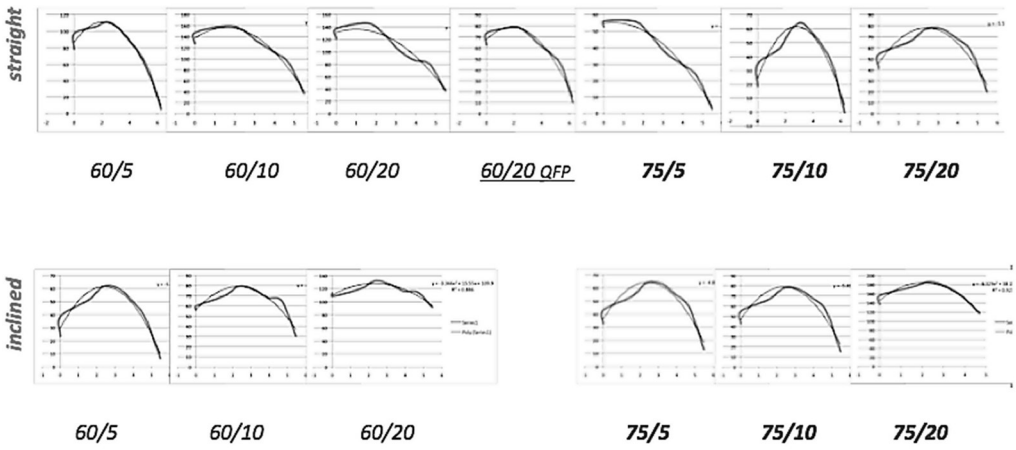

Fig.21 *'Velocity linear profiles from **LOIsV**, for **straight** and **inclined** tube at 60, 75 bpm and 5, 10, 20% pump output'*

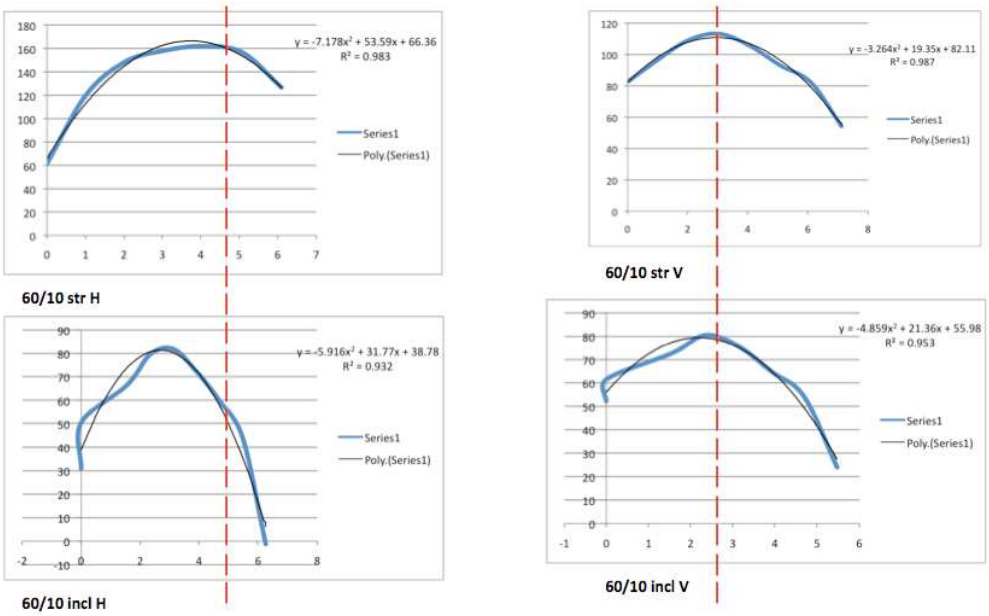

Fig22. *'Fitted curves extracted from **horizontal** and **vertical LOIs**, at 60 bpm, 10% pump output, in straight and inclined position of the PVC tube of 6mm internal diameter.'*

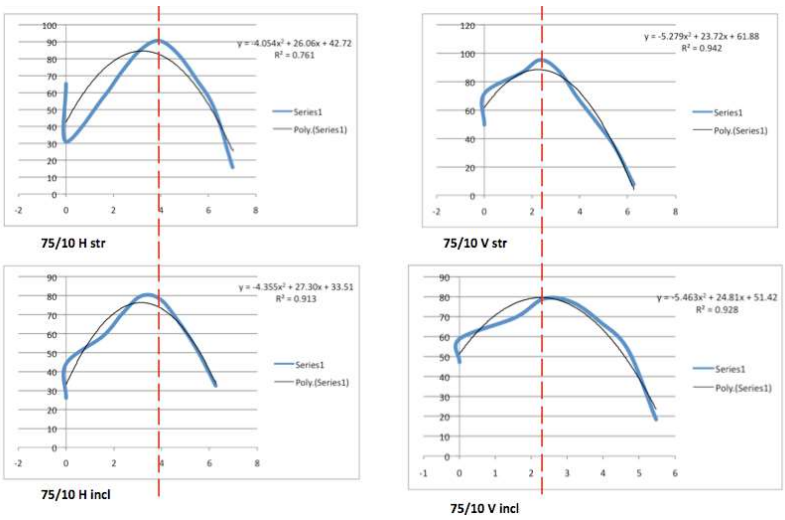

Fig.23 *'Fitted curves extracted from horizontal and vertical LOIs, at 75 bpm, 10% pump output, in straight and inclined position of the PVC tube of 6mm internal diameter.'*

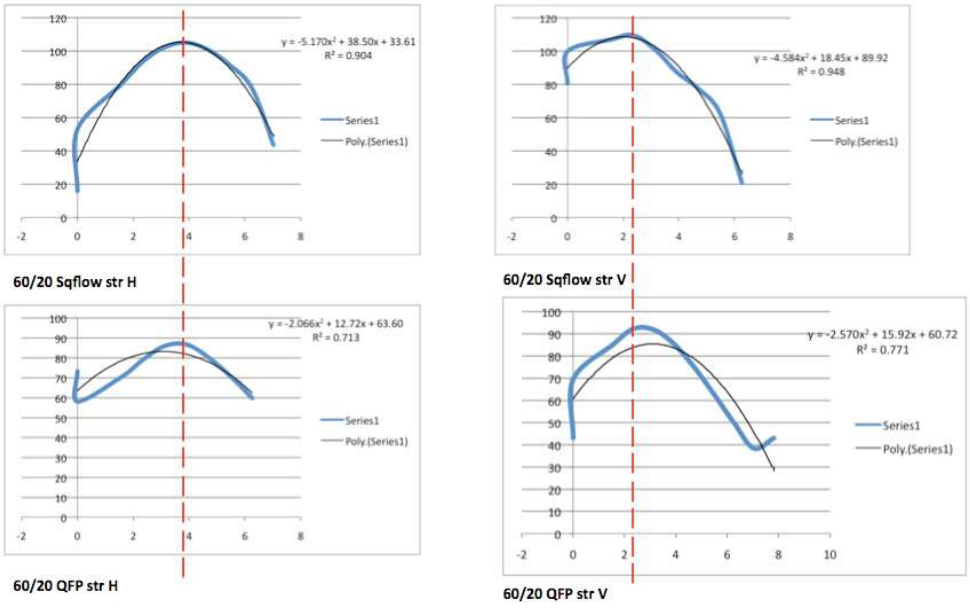

Fig.24 *'Fitted curves extracted from horizontal and vertical LOIs, at 60 bpm, 20% pump output, in straight and inclined position of the PVC tube of 6mm internal diameter, by QFP and Sqflow sequences'.*

6.1.3 Stenotic tube:

A) VFR values

(Stenotic tube) **elliptical** ROIs (ejection fraction 10%)									
	VFR **pre** stenosis (cm^3/s)				Intra-stenotic	VFR **post** stenosis (cm^3/s)			
bpm/ distance	**4 (cm)**	**3 (cm)**	**2(cm)**	**1(cm)**	**0(cm)**	**1(cm)**	**2(cm)**	**3(cm)**	**4(cm)**
60	13,429	26,317	40,5	13,232	**67,255**	33,776	28,224	10,395	13,182
75	9,175	9,435	8,252	8,723	**70,5**	44,057	31,643	8,347	15,155
100	10,881	42,659	11,493	24,377	**73,311**	29,89	8,397	13,888	7,281
120	3,354	13,996	3,532	16,707	**82,352**	16,831	19,063	24,222	7,839

Table 17. *'**VFR** values in stenotic 8mm tube, pre and post stenotically, measured at 10 % of pump output for 60, 75, 100, 120 bpm'*

B) Vmax values

(Stenotic tube) **elliptical** ROIs (ejection fraction 10%)									
	Vmax **pre** stenosis (cm/s)				Intra-stenotic	Vmax **post** stenosis (cm/s)			
bpm/ distance	**4 (cm)**	**3 (cm)**	**2(cm)**	**1(cm)**	**0(cm)**	**1(cm)**	**2(cm)**	**3(cm)**	**4(cm)**
60	16,2	38,7	51,7	36,8	**199,5**	181,8	30	46,9	53,3
75	35,2	16,6	16,7	41,1	**95,6**	97,3	18,9	16	48,8
100	12,6	119,1	35,5	23,2	**139**	206,5	68,4	10,1	40,5
120	29,8	63,3	9,6	51,5	**46,7**	197,9	22,4	33,7	33,9

Table 18. *'**Vmax** values in stenotic 6mm tube, pre and post stenotically, measured at 10 % of pump output for 60, 75, 100, 120 bpm'*

(Stenotic tube) **LOIs (H) pump output 10%**									
	Vmax **pre** stenosis (cm/s)				Intra-stenotic	Vmax **post** stenosis (cm/s)			
bpm/ distance	**4 (cm)**	**3 (cm)**	**2(cm)**	**1(cm)**	**0(cm)**	**1(cm)**	**2(cm)**	**3(cm)**	**4(cm)**
60	13,258	4,929	6,085	13,55	**24,307**	10,787	1,689	8,463	5,724
75	4,65	1,261	7,82	4,004	**35,48**	32,455	7,158	4,625	14,284
100	2,893	9,054	3,651	10,262	**44,057**	52,147	7,792	31,827	14,159
120	2,386	7,52	2,826	2,504	**39,273**	40,746	8,337	60,358	2,314

Table 19. *'**Vmax** values from LOIs (**horizontally** designed) in stenotic 6mm tube, pre and post stenotically, measured at 10 % of pump output for 60, 75, 100, 120 bpm'*

(Stenotic tube) **LOIs (V) pump output 10%**									
	Vmax **pre** stenosis (cm/s)				Intra-stenotic	Vmax **post** stenosis (cm/s)			
bpm/ distance	**4 (cm)**	**3 (cm)**	**2(cm)**	**1(cm)**	**0(cm)**	**1(cm)**	**2(cm)**	**3(cm)**	**4(cm)**
60	2,51	0,52	15,11	14,94	122,52	11,15	6,1	4,24	14,64
75	0,41	1,74	2,22	4,58	79,92	19,42	2,17	10,92	4,46
100	1,97	6,16	2,06	3,47	16,68	60,05	31,71	19,27	2,2
120	1,89	7,74	3,08	3,21	16,82	46,14	11,58	8,64	7,32

Table 20. *'**Vmax** values from LOIs (**vertically** designed) in stenotic 6mm tube, pre and post stenotically, measured at 10 % of pump output for 60, 75, 100, 120 bpm'*

C) R^2 values

(Stenotic tube) LOIs (H) pump output 10%									
	R^2 (pre stenosis)				Intra-stenotic	R^2 (post stenosis)			
bpm/ distance	4 (cm)	3 (cm)	2(cm)	1(cm)	0(cm)	1(cm)	2(cm)	3(cm)	4(cm)
60	0,062	0,706	0,458	0,461	**0,419**	0,915	0,834	0,037	0,711
75	0,087	0,727	0,495	0,794	**0,685**	0,62	0,119	0,581	0,591
100	0,667	0,159	0,544	0,503	**0,84**	0,366	0,489	0,795	0,713
120	0,511	0,227	0,824	0,753	**0,436**	0,574	0,179	0,612	0,753

Table 21. *'R^2 values from LOIs **horizontally** designed, in stenotic 6mm tube, pre and post stenotically, measured at 10 % of pump output for 60, 75, 100, 120 bpm'*

(Stenotic tube) LOIs (V) pump output 10%									
	R^2 (pre stenosis)				Intra-stenotic	R^2 (post stenosis)			
bpm/ distance	4 (cm)	3 (cm)	2(cm)	1(cm)	0(cm)	1(cm)	2(cm)	3(cm)	4(cm)
60	0,485	0,735	0,966	0,828	0,153	0,581	0,882	0,9	0,916
75	0,354	0,382	0,957	0,929	0,882	0,71	0,87	0,882	0,944
100	0,297	0,7	0,548	0,042	0,983	0,065	0,862	0,952	0,795
120	0,648	0,569	0,5	0,185	0,552	0,345	0,934	0,934	0,913

Table 22. *'R^2 values from LOIs **vertically** designed, in stenotic 6mm tube, pre and post stenotically, measured at 10 % of pump output for 60, 75, 100, 120 bpm'*

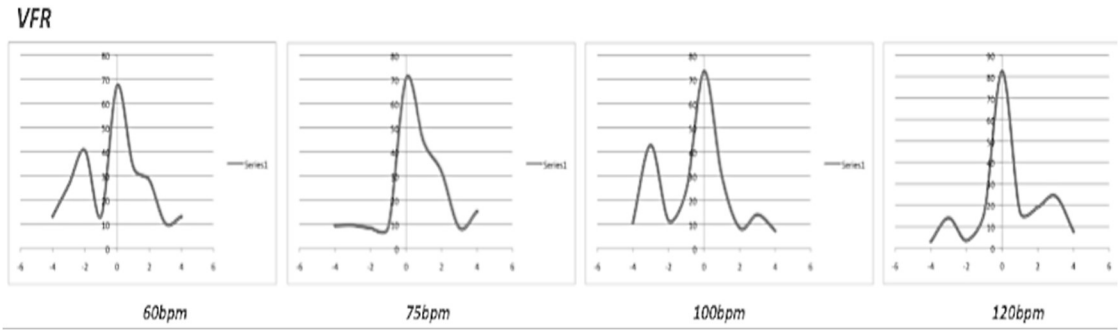

Fig 25. *'Variation of VFR as a function of distance across the stenosis measured at regular intervals of 1cm upstream and downstream the stenosis.'*

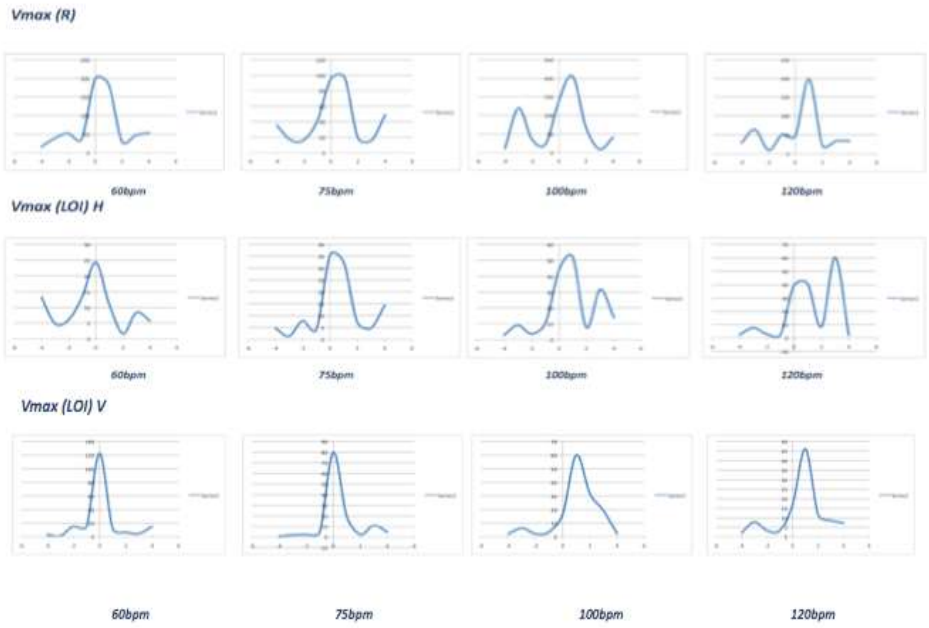

Fig.26. *'Variation of Vmax a) ROIs,, b) LOIs H, c) LOIs V) as a function of distance across the stenosis measured at regular intervals of 1cm upstream and downstream the stenosis'.*

D) Velocity profiles for straight and inclined tube

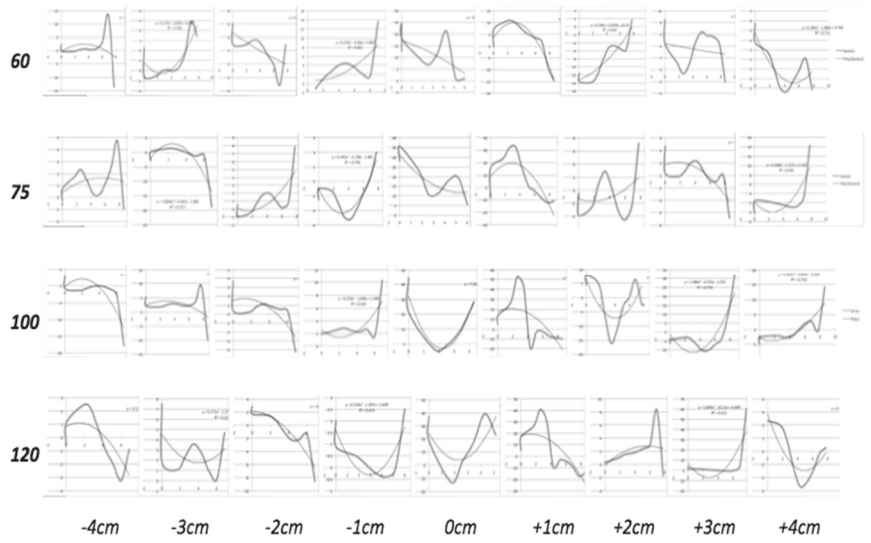

Fig.27. *'Velocity profiles acquired from (LOIs in horizontal direction), stenotic tube at 60, 75,100,120 bpm and 10% pump output, for intervals of 1cm upstream and downstream the stenosis'*

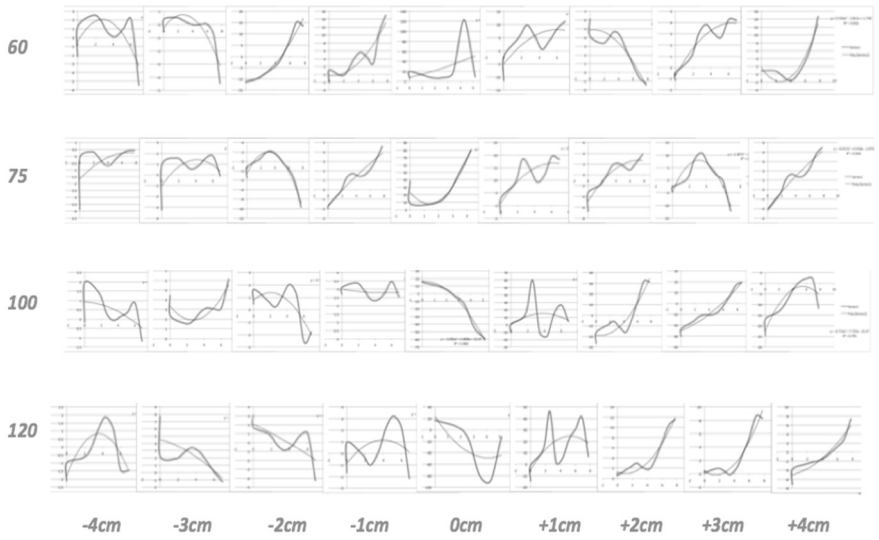

Fig.28 *'Velocity profiles acquired from (LOIs in the vertical direction) stenotic tube at 60,75,100,120 bpm and 10% pump output, for intervals of 1cm upstream and downstream the stenosis'*

E) Percentage of stenosis (X)

X% = 100*[1- ($V_{\pm 4}$ / V_{in})] *(H) LOIs*					
bpm	**Vmax** *(cm/s)* 4 cm pre	**Vmax** *(cm/s)* 4cm post	**Vintr** *(cm/s)*	**Xpre %**	**Xpost %**
60	13,258	5,724	24,307	45,45	76,45
75	4,65	14,284	35,48	86,89	59,74
100	2,893	14,159	44,057	93,43	67,86
120	2,386	2,314	39,273	93,92	94,11

X% = 100*[1- ($V_{\pm 4}$ / V_{in})] *(V) LOIs*					
bpm	**Vmax** *(cm/s)* 4 cm pre	**Vmax** *(cm/s)* 4cm post	**Vintr** *(cm/s)*	**Xpre %**	**Xpost %**
60	2,51	14,64	122,52	97,95	88,05
75	0,41	4,46	79,92	99,49	94,42
100	1,97	2,2	16,68	88,19	86,81
120	1,89	7,32	16,82	88,76	56,48

Table 23. '*Rate of stenosis* ***X%*** *for 6mm stenotic tube, measured at 10 % of pump output for 60, 75, 100, 120'*

	X% = 100*[1- ($V_{\pm 4}$ / V_{in})] ***elliptical ROIs***				
bpm	**Vmax***(cm/s)* 4 cm pre	**Vmax***(cm/s)* 4cm post	**Vintr** *(cm/s)*	**Xpre%**	**Xpost%**
60	13,429	53,3	**199,5**	91,88	73,283
75	9,175	48,8	**95,6**	48,954	63,18
100	10,881	40,5	**139**	70,863	90,935
120	3,354	33,9	**46,7**	27,409	36,188

Table 24. *'Calculated rate of stenosis* ***X%****, for 6mm stenotic tube, measured at 10 % of pump output for 60, 75, 100, 120 bp'm*

LOIs CT X%			
Diameter stenosis		*Area stenosis*	
100*(1-(Dsten/Dp))		100*(1-(Asten/Ap)	
0,58	90,21%	0,305	98,98%
5,925		29,802	

$$A= D*(2-(D/100)) \Leftrightarrow A=99\%$$

Table 25.' *Estimated rate of stenosis* ***X%, from CT scans,*** *for 6mm stenotic tube, measured at 10 % of pump output for 60, 75, 100, 120 bpm'*

G) Signal to noise ratio SNR:

Rectangular ROIs SNR= $Intensity_{mean}$ / $Intensity_{std}$							
10% pump output	Pre-stenosis			Post-stenosis			
bpm	$Intensity_{mean}$	$Intensity_{std}$	SNR_{pre}	$Intensity_{mean}$	$Intensity_{std}$	SNR_{post}	Ratio%
60	716,8	64,84	11,054	496,1	97,88	5,068	54,15
75	746,4	44,74	16,682	527,8	109,41	4,824	71,08
100	738,7	48,39	15,264	520,9	107,88	4,829	68,37
120	775,2	42,85	18,09	558,1	112,71	4,951	72,63

Table 26.' ***SNR*** *values for 8mm stenotic tube, measured at 10 % of pump output for 60, 75, 100, 120 bpm'*

Volumetric Results

Percentage (%)	5	10	15	20	25	30
Pressure (bar)	1,8	2	2,4	2,6	2,7	3
Volume (ml=cm^3) 1	4	6	11,3	15	17,3	20,6
2	4,3	5,6	11,3	15,3	17,3	20,6
3	4	5,6	11,3	14,6	17,3	21
4	4	5,3	11,3	14,6	17,3	20,6
5	4	5,6	11,3	14,6	17,3	20,6
6	4	5,3	11,3	14,6	17,3	20,6
7	4,3	5,3	11,3	14,6	17,3	20,3
8	4	5,3	11,3	14,6	17,3	20,6
9	4	6,3	11,3	14,6	17,3	20,6
10	4,3	6	11,3	14,6	17,3	20,6
Average Volume	***4,1***	***5,6***	***11,3***	***14,7***	***17,3***	***20,6***
Standard Deviation	0,15	0,33	0	0,21	0	0,14

Table 27 '*Volumetric measurements at 75 bpm for 5%, 10%, 15%, 20%, 25% and 30% of nominal pump output'*

	stenosis 1	*stenosis 2*	*stenosis 3*
I_{in}	1429,94	124,14	751,65
$I_{std\ in}$	230,72	77,01	213,95
SNR_{in}	*6.1977*	*1.612*	*3.5132*
I_{out}	411,95	164,31	323,37
$I_{std\ out}$	59,67	31,19	60,66
SNR_{out}	*6.9038*	*5.268*	*5.330*
SNR_{ratio}	0,8977	0,3063	0,6590
$SNR_{\%loss}$	*10.23%*	*69.37%*	*34.10%*

Table 28 *'SNR calculated values'*

Slice- center of stenosis distance (cm)	**Stenosis 1**	**Stenosis 2**	**Stenosis 3**
-7,5	0,994	0,985	0,961
-6	0,993	0,995	0,994
-4,5	0,993	0,987	0,969
-3	0,989	0,991	0,94
-1,5	0,99	0,796	0,823
0	-	-	-
1,5	0,891	0,976	0,845
3	0,839	0,991	0,972
4,5	0,98	0,984	0,946
6	0,91	0,964	0,945
7,5	0,976	0,963	0,963
Average	***0,95***	***0,96***	***0,93***
Standard deviation	0,05	0,05	0,05

Table 29 '*R^2 values derived from the paraboloid fit to Image J imported data'*

% percentage stenosis			
Slice- center of stenosis distance (cm)	*stenosis 1*	*stenosis 2*	*stenosis 3*
-7,5	92,8205	56,9377	89,1362
-6	81,5384	78,9473	73,3748
-4,5	85,6410	80,3827	87,9786
-3	87,1794	44,9760	84,1495
-1,5	87,1794	70,3349	80,2315
0	0	0	0
1,5	-161,5384	-10,5263	17,6313
3	-91,2820	-66,5071	42,6536
4,5	59,4871	23,9234	84,5057
6	70,7692	64,5933	86,5538
7,5	45,6410	65,0717	88,0676
Average	35,7435	40,8133	73,4283
Standard Deviation	83,7139	44,4538	24,0124

Table 30 '% percentage stenosis calculated from MRA'

Multislice CT results

roi (cm^2)	**stenosis 1**	**stenosis 2**	**stenosis 3**
pre	1,01	1,16	1,16
At stenosis	0,01	0,01	0,1
post	1,01	1,15	1,15
percentage stenosis	***99,01***	***99,13***	***91,37***
loi cm	stenosis 1	stenosis 2	stenosis 3
pre	1,22	1,21	1,18
At stenosis	0,06	0,1	0,21
post	1,23	1,21	1,14
percentage stenosis	***95,08***	***91,73***	***82,20***

Table 31 '*% stenosis calculated from MSCT'*

CHAPTER 7

IN VIVO ANALYSIS

7.1 Tabulated results of WSS values in the arterial tree using PC-MRI

The results presented in Tables 1 and 2 indicate that most of the in vivo measurements of WSS at each arterial segment show qualitative agreement. However, differences exist in absolute values of WSS values measured by different investigators. These variations can be attributed to the following factors:

(a) Different techniques were used to acquire the blood velocity data,

(b) Different interpolation algorithms were used to estimate WSS,

(c) Different values of dynamic blood viscosity were used,

(d) The exact site of WSS measurement at each arterial segment was inconsistent,

(e) Wide variations in the measured WSS values among individuals were observed.

The measured values of WSS included in this review oppose a widely accepted notion that physiological WSS values are maintained at 1.5N/m^2 in all parts of the arterial system, especially at the large and straights arteries that are subject to steady and laminar flow [72,73,74].

The rationale of constant WSS throughout the arterial system is based on numerous experiments that have shown that WSS variations actively influence wall remodeling [75] by expansion or contraction of the internal vessel radius in order to maintain a mean WSS magnitude of about 1.5N/m^2. Apart from the argument of whether WSS magnitude is constant in arterial circulation, to date it has been well established that WSS is an important determinant of arterial diameter, both acutely and chronically, and that these adaptations result in maintaining mean arterial WSS within limits with changing flow requirements or changes in blood viscosity [76-77].

The accuracy of the measured values of WSS included in this review depends on the methodology used in each study. One important source of error in the studies that calculate WSS by measuring the velocity gradient near the vessel wall and applying Equation 3.1.1 ($WSS = \mu \frac{du}{dr}$) is the limited spatial resolution of PC-MRI. Another lesser source of error is the limited temporal resolution of velocity measurements[27]. The studies than calculate WSS by single velocity measurements and the application of Equations 3 ($WSS = \frac{2\mu u_M}{R}$) and 4 ($WSS = \frac{4\mu u_{ave}}{R}$) are

limited by the assumptions on which these equations are based (steady and laminar flow, straight and cylindrical vessels and blood resembling a Newtonian fluid) which are not valid in arterial circulation.

The inherent low spatial and temporal resolution of PC-MRI limits the accuracy of WSS determination, at least with the current generation of MR units that are used in clinical practice. An alternative to overcome this limitation that is widely used is the integration of MR imaging and computational flow dynamics (CFD). CFD is a general term used to describe the body of knowledge and methods that seek the numerical solution of the governing (Navier-Stokes) equations of fluid flow. Typically, a CFD problem consists of simulating the flow patterns in a given geometry under certain boundary conditions for the flow variables. This simulation involves the numerical solution of the governing equations by discretizing the given geometry into a large number of small geometric segments forming a computational mesh on which the variables of interest are calculated. The discretization (in space and time) of the governing differential equations results in a system of algebraic equations, whose numerical solution yields the problem unknowns at the mesh points. To perform a CFD simulation of flow in a blood vessel, the three-dimensional geometry of the vessel lumen is required and also the inflow and outflow boundary conditions for the variables have to be imposed. MR imaging can provide both the three-dimensional description of the vessel lumen and the flow data required to perform the CFD simulation. The main limitations of the application of CFD to the study of arterial blood flows arise from the uncertainties in defining the problem with the requisite precision, rather than the inherent limitations of the numerical techniques or hardware capabilities. For example, in the simulation of blood flow in coronary arteries, the ambiguities associated with the precision of the three-dimensional reconstruction of the coronary arterial tree and the definition of the inflow/outflow boundary conditions, as well as the motion of the coronary vessels during the cardiac cycle, give rise to considerable uncertainty regarding the validity of computational results.

Conclusively, in vivo data of WSS measured in healthy humans exist for the following arteries: carotid arteries, brachial arteries, aorta and femoral arteries. WSS values are not constant within the arterial system but are site specific. WSS values at the same site measured by different investigators show qualitative agreement; however, differences exist in absolute values due to the methodology utilized in each study. The main limitation of PC-MRI is its spatial and temporal resolution that limits the accuracy of shear stress assessment near the vessel wall.

Expert commentary

The appearance and progression of atherosclerotic disease occurs as a function of both genetic predisposition and risk factors, such as smoking, arterial hypertension, diabetes mellitus and hyperlipidemia. Although atherosclerosis is a disease affecting the vascular system as a whole, it has uneven distribution with substantial differences in the localization and progression of atheromatic plaques. Certain sites are predisposed to development of atheromatosis, such as the

outer wall of vessel bifurcations and the inner wall of curved arteries. There is evidence that independently of systemic factors, the presence of local hemodynamic factors such as WSS play a major role in the generation and progression of atherosclerotic plaques as well as in the risk of potential plaque rupture and subsequent thrombosis. The study of WSS distributions in the arterial tree and the spatio-temporal changes of WSS might indicate segments of the arterial tree that are predisposed to atheromatosis and at which plaques are more susceptible to rupture. The clinical implication for the management of vascular disease is that intervention must be decided on the basis of an extended set of determinants (including, WSS as well as mechanical strains induced by temporal changes of the vessel wall due to ventricular contraction) and not based solely on conventional assessment of vascular stenosis.

Five-year view

In vivo determination of WSS is particularly challenging since it requires the determination of the velocity gradient near the vessel wall under conditions of pulsatile flow. Thus the methodology of blood flow velocity measurement must provide measurements with high spatial and temporal resolution. The measuring methodology must be also applicable to both superficial and deep arteries. Ideally the methodology should be non-invasive for simple application and also to avoid uncertainties of the results due to the presence of a measuring probe in the blood flow field. The only current methodology that meets all of the above criteria appears to be PC-MRI. Nevertheless, the spatial and temporal resolution of PC-MRI is inferior compared to other techniques which are however either applicable only to superficial vessels or invasive. The new generation of MR units that are currently entering clinical practice incorporate 3T magnets rather than 1.5T magnets that current units use. These advanced units together with advanced acquisition protocols are expected to improve the spatial and temporal resolution of blood flow velocity measurements and thus will allow more accurate determination of WSS. The improved resolution will also allow the use of PC-MRI for the in vivo determination of WSS at small and moving vessels such as the coronary arteries. The availability of an accurate method to study blood flow characteristics such as WSS at the coronary arterial tree would be of cardinal clinical importance since the coronaries are particularly affected by atherosclerosis while at the same time various autopsy studies have validated the hypothesis that atherosclerosis primarily involves the segments of the coronary tree that is subject to “disturbed” blood flow behaviour.

Key issues

- The presence of local hemodynamic factors such as WSS plays a major role in the generation, progression and destabilization of atherosclerotic plaques.
- WSS values at various sections of the vascular tree may be of clinical significance.
- PC-MRI is the only non-invasive, in vivo method with adequate spatial and temporal resolution that is applicable to almost any artery in the human body.
- Current literature includes WSS values measured by PC-MRI for the following arteries: carotid arteries, brachial arteries, aorta and femoral arteries

- WSS values differ among different parts of the arterial tree.This finding opposes a widely accepted notion that physiological WSS values are maintained at a constant value in all parts of the arterial system.
- The absolute values of WSS measured at the same site differ mainly due to the dependence on the method used to obtain WSS values from velocity data.
- The limited spatial and temporal resolution of the method allows WSS assessment only in large vessels.

7.2 In vivo Wall Shear Stress calculation

This part of the thesis presents a comparison of WSS calculations in ascending aorta between 4 methods that have been previously presented for WSS calculations.

Calculations with LM are based on the equation which defines shear stress and can be characterized as position-sensitive method because WSS can be measured in any point of the circumference of the vessel wall and it can provide the circumferential distribution of WSS across the arterial wall. The basic advantage of LM is that it is not based on theoretical equations derived by assumptions, but results are calculated directly by measurements using the definition of WSS. Other advantages of the method are its inherent simplicity due to the fact that it does not require sophisticated calculations or complicated data processing. The basic disadvantage of this method is that it is more time consuming. Furthermore, it is limited by the fact that the measured velocity at the vessel walls is non-zero due to

i) in-plane vessel wall movement and deformation during the acquisition of image data and

ii) Partial volume artifact which can be overcome by higher acquisition matrix and therefore higher in-plane resolution in the cost of longer examination time or lower signal to noise ratio.

AFM, AVM and MVM are based on equations derived from Poiseuille's theory of flow. These methods provide the average value of WSS across the arterial lumen and thus they cannot provide information about its circumferential distribution. It is obvious that these methods are established under assumptions, such as steady conditions of laminar flow, and blood resembling a Newtonian fluid that is flowing inside a straight cylindrical tube with rigid walls. This is hardly the case in arterial circulation where flow is pulsatile and it occasionally becomes turbulent. Additionally, blood vessels are distensible and their cross-section is tapered. Finally, blood can be considered as a Newtonian fluid only under specific conditions. Given these considerations, it is obvious that the values of WSS obtained from equations ?-?, theoretically can only be considered as approximates. The main advantages of these three methods are that they are quick and easy to use in clinical practice. Since the operator defines the vessel by a region of interest, average WSS is calculated directly by the use of one single measurement for the specific cross-section of the

vessel; average blood volume flow for AFM, average blood velocity for AVM, and maximum blood velocity for MVM.

LM and MVM present another disadvantage against the other methods; they are point-sensitive, since LM is based on two velocity measurements, the two closest pixels on vessel wall, while MVM is based on only one velocity measurement, the maximum into the specific vessel cross-section.

An additional limitation of the LM is the in plane spatial resolution of acquired measurements. We evaluated aortic flow retrospectively at patients that have undergone cardiac MRI examination and the in plane spatial resolution for velocity measurement was 1.4 mm which is lower than similar studies [46]. However, since the ascending aorta is a large vessel (2.5-3 cm) we where able to acquire 15-19 velocity values across the aortic lumen and thus we could fit a parabolic function at the measured velocities with a good sampling. Therefore we consider this spatial resolution adequate for WSS calculations based on the assumption of a parabolic profile and the application of the Hagen-Poiseuille expressions. Nevertheless, higher spatial resolution is necessary to evaluate the velocity gradient near the vessel wall and derive accurate WSS values by application of LM.

Our data indicate that for our randomly selected set of patients all methods give similar results and therefore we can calculate WSS with the application of anyone of them. By application of the parabolic fit process we see that, for this cohort of patients, the shape of the velocities distribution is parabolic (R^2=0.83). It is therefore presumable that calculations based on parabolic assumption of Poiseuille's theory of flow, which are those made by AFM, AVM, MVM, work well. It is obvious that these three methods are applicable only at sites of the arterial circulation were the blood flow velocity distribution is parabolic. The later can be assumed to be valid at the straight parts of the arterial system that are not close to bifurcations or curvature or it can be checked as in the current study before applying the methodology of WSS calculation based on Poiseuille's theory of flow.

The consideration of blood as a Newtonian fluid is a limitation of the study. Comparison of various non Newtonian models of blood against the Newtonian model under steady and transient flow conditions has revealed that although the distribution of WSS at the vessel wall among the different model is identical, differences exist at the absolute values of WSS, especially when the rate of shear is low [21, 22]. However, the differences of absolute values of WSS among the models are relatively low compared to other possible sources of uncertainty such as vessel distensibility and motion. Therefore, the Newtonian model is commonly adapted in similar studies[56,57,59].

In conclusion, the results indicate that the four methods that have been proposed for WSS calculations in the ascending aorta give similar results. Thus, in clinical practice, one can adopt the method which is most easy and convenient for the user to apply. Our data indicate that all methods provide results with no statistically significant differences. The applicability of the straightforward methods based on Poiseuille's theory of flow relies on the existence of parabolic

velocity distribution inside the aortic lumen. Therefore, the parabolic behavior of flow in the ascending aorta has to be tested prior of selecting the measuring method. This test can be performed with the parabolic fit proposed in this study. Further work should be done to examine the results that different methods give when the profile of blood velocities inside the vessel is not parabolic.

8.3 Wall shear stress calculation throughout the cardiac cycle

Although in-vivo WSS data are generally scarce, a few studies exist in which WSS calculations are based on the formulas derived from Poiseuille's theory of flow [79, 80, 81,4]. This study presents a comparison between three methodologies for the calculation of WSS based on Poiseuille's theory of flow at the ascending aorta. To the best of our knowledge there has been no attempt to compare these three methodologies at a specific blood flow measurement application.

The three methods theoretically can be considered equivalent, as they are based on the Poiseuille's theory of flow, which estimates the value of wall shear stress under the assumptions described earlier. The interesting finding of this study is that in all circumstances AF and AV methods yield similar results whereas WSS calculations with the MV method present statistically significant differences with the two other methods except for the case of peak systolic WSS.

A possible explanation based on the hypothesis that the velocity profiles at the site of measurement are not parabolic in shape, especially if one considers the proximity of the specific site to the aortic valve, cannot be proved since the acquired velocity profiles showed a satisfactory parabolic profile with an average adjusted coefficient of determination of the fitted curve equal to 0.7. The average adjusted coefficient of determination is calculated as the average R^2 value of the parabolic curves fitting the acquired velocity data of all patients.

That means that Equations (3.1.2) – (3.1.4) are applicable at the particular site although the accuracy of the derived results is limited as discussed later.

Comparison of the average WSS values presented at tables ? and ? indicates that peak systolic WSS and maximum WSS values are equal when computed by the AF and AV methods. This means that volume flow and average flow velocity become maxima at peak systole. In contrast to this, maximum flow velocity reaches its peak value later than peak systole, thus peak systolic WSS values and maximum WSS values differ when computed by the MV method.

Comparison of the average WSS values presented at tables ? and ? indicates that minimum WSS values are different from end-diastolic WSS values. It is clear that WSS values that at the moment of maximum diastole, regardless of the method of calculation, are higher than minimum WSS values which are calculated at the time instances that volume flow, average flow velocity and maximum flow velocity are minimized.

A potential explanation for the observed discrepancies between the calculated WSS values is to be found in the blood flow curves through the R-R interval (Figure ?). In most cases (15 out of 20), blood flow reaches its peak before the velocity itself reaches its maximum value, while in two cases, time difference between maximum flow and maximum velocity was minimal and in other four, maximum velocity preceded maximum flow. Average time difference between flow (Q_{max}) and peak velocity ($U_{peak\ max}$) was 98.05 ms. Time difference is also observed between end-diastolic and minimum WSS measurements. In 15 out of 20 patients minimum flow (Q_{min}) was exhibited on average 226.65 ms before minimum velocity ($U_{min\ max}$).

Another factor affecting these discrepancies is that the AF and AV formulae are based on the average pixel values that each ROI exhibits, whereas the MV method is based on the value of the one single pixel that has the highest signal and thus velocity value. This implies that WSS calculations with the use of maximum velocity are prone to large uncertainties or even false results due to artifacts. Therefore, we consider WSS measurements based on the mean blood volume flow or the mean flow velocity as more reliable.

Direct evaluation of the accuracy of the derived results is not feasible since no gold standard exist for the estimation of WSS in vivo. Additionally, there are no published WSS values for the specific arterial site and since WSS is site specific [45,70] we cannot evaluate accuracy by comparing with WSS values measured at different arterial sites. The most comparable study is the one by Wentzel et al in which systolic WSS at the descending aorta was measured 0.79 N/m^2 (compared to the average systolic WSS value of 0.41 N/m^2 measured in this study).

The above results and indicate that WSS measurements based on the maximum blood velocity show large deviations with respect to the measurements that use the mean blood volume flow or the mean blood velocity. Therefore, in-vivo WSS measurements require careful selection of the applied methodology.

Limitations

The considered methodologies are based on the assumption of Poiseuille's theory of flow. As stated before, Poiseuille's theory of flow is established under steady conditions of laminar flow, for a Newtonian fluid that is flowing inside a straight cylindrical tube with rigid walls. It is obvious that this is not always the case in arterial circulation where flow is pulsatile by its nature and it becomes occasionally turbulent. This fact imposes undoubtedly intrinsic limitations to how accurately WSS can be calculated based on the aforementioned equations on occasions where the flow is non-laminar like in the beginning or end of the heart cycle. Additionally blood vessels are distensible resulting in a limitation on how accurately wall can be visualised and excluded from the measurements. Finally, blood cannot be generally considered as a Newtonian fluid but it is a common approximation in various similar studies [45,70]. Given these considerations it is obvious that the values of WSS obtained by the above methodologies can only be considered as approximates. It must be also noted that the considered methodologies provide the spatial average

of WSS at the site of measurement, thus they do not provide any information about the circumferential distribution of WSS.

In conclusion, estimation of systolic and diastolic WSS in the human ascending aorta is feasible by flow measurements obtained by phase-contrast MRI and the use of methodologies based on Poiseuille's theory of flow. However, the theoretically equivalent mathematical formulas do not yield equivalent results. It appears that when maximum blood flow velocity is used, the resulting WSS values are higher than the values obtained by the methodologies that utilize average volume flow or average velocity in the arterial lumen. This fact points towards the need of careful selection of the measuring methodology of WSS calculation at the human arterial tree especially when maximum WSS is to be considered as the parameter under investigation. When WSS is to be calculated at a particular phase of the cardiac cycle (e.g. at peak-systole or end-diastole) then the AF and the MV methods produce equivalent results. Methods based on the mean volume flow or the mean flow velocity should be preferably used for WSS calculations by phase-contrast MRI.

IN VITRO ANALYSIS

Stenosis quantification dependence on the pulsatility of flow using phase contrast MRA

The study of pulsatile flow through a stenosis is motivated by the need to obtain a better understanding of the impact of flow phenomena on atherosclerosis and stroke. MRI techniques have been employed to characterize flow emerging from a stenotic and a non-stenotic tube. Detection and quantification of stenosis serve as the basis for surgical intervention. In the future, the study of arterial blood flow will lead to the prediction of individual hemodynamic flows in any patient, the development of diagnostic tools to quantify disease, and the design of devices that mimic or alter blood flow. Blood flow and pressure are unsteady. The cyclic nature of the heart pump creates pulsatile conditions in all arteries. The heart ejects and fills with blood in alternating cycles called systole and diastole. Blood is pumped out of the heart during systole. The heart rests during diastole, and no blood is ejected. Pressure and flow have characteristic pulsatile shapes that vary in different parts of the arterial system. The experiments demonstrate that stenotic pulsatile flow exhibit flow disturbance phenomena which deviate the flow from the laminar behavior.

In vitro measurements can simulate blood flow to a satisfactory degree, under various assumptions for flow. In this study, estimation of various hemodynamic parameters, are achieved by means of a flow phantom. The phantom can simulate pulsatile blood flow in arterial system, in our case blood flow in carotid artery. The phantom consists of an one-headed positive displacement diaphragm pump, driven by an electrocardiogram (ECG) generator, with the tube, creating a closed circuit. Within the circuit, water (as blood mimicking fluid) is driven, simulating blood flow. We studied the flow using velocity-encoded MR phase contrast sequences.

Phase contrast angiography relies on dephasing the moving spins submitted to a bipolar gradient. For a bipolar gradient of a given intensity and time, the moving spins will dephase in proportion to their velocity. Similar to spatial encoding in the phase direction, the possible phase values range from $-\pi$ to $+\pi$. Beyond this range of values, aliasing occurs, causing poor velocity encoding. The encoding gradient characteristics are thus defined in order to encode flows within a certain velocity range from $-V_{enc}$ to $+V_{enc}$ to be determined by the user. Any velocity outside this range will be poorly encoded (similar to what happens in pulsed and color Doppler with PRF).

The present work refers to blood flow estimation by means of Magnetic Resonance Imaging. The MR imaging system used, is a 1.5 Tesla scanner (Intera 1.5T, Philips Medical Systems, Best, the Netherlands) of Attikon Hospital (Second Department of Radiology). CT imaging system is a Philips Brilliance 64, used to assess the percentage of the stenosis.

The experimental set up consists of a flow phantom, simulating blood flow through blood vessels under chosen conditions. Gradient echo (phase contrast) sequences used, precisely: SQ flow and QFP sequences. MR phase-contrast technique quantifies and displays flow velocities in

real times. The sequence uses a two-dimensional selective radiofrequency pulse followed by flow-sensitizing gradients with an echo planar readout. It provides the simultaneous display in real time of both an anatomic image for positioning and the through plane flow-velocity data. By controlling scan position and orientation interactively, one can optimize flow signal. The retrospective search of measurements is carried out with the database of a software used, called EVORAD. The software of the workstation automatically provided the following parameters: ROI area (cm^2), vessel lumen diameter (cm), blood volume flow (ml/s), mean and maximum blood flow velocities (cm/s). The LOIs in respective, used for velocity profiles determination, were acquired by ImageJ software, by similar procedure at vertical and horizontal direction on the lumens' plane perpendicular to the flow.

Two different geometries were used: a PVC tube mimicking a healthy carotid artery of 6mm internal diameter and a stenotic glass tube to simulate arterial pathology, of 8mm internal diameter. Considering the non-stenotic PVC tube, VFR values are estimated volumetrically (for various bpm and pump output values) and via MRI (for straight and inclined position). VFR values are then compared. MR maximum velocity values are estimated too, and velocity profiles are plotted. The procedure is similar in the case of the stenotic glass tube, for various (bpm and PO; pump output) and at intervals of 1cm across the stenosis reaching 4cm upstream and downstream. In the sequence of estimation, percentage of stenosis follows; estimated from both MRI and CT scans. Finally, variation of pressure and SNR in order to assess the signal loss due to stenosis are estimated.

Non stenotic tube: The first significant issue to mention, is the greatest cv (coefficient of variation) values at lower **VFRs** (measured at 10%pump output and pressure of 2,5b), among all VFR values for both 60 and 75 bpm, and the greatest std values noticed at the greatest VFRs (60%, 4.6b). VFR values are indeed greater at 75 bpm compared to those at 60 bpm, as expected. Values show no stable relevance between VFR and pump output. There are slight differences in VFR values from the inclined position, though are statistically insignificant, in all cases compared. No statistical differences (at 5% statistical significance), are noticed between volumetric measurements versus MRI extracted values as compared above, for both SQflow and QFP sequences. VFR values comparison between volumetric and MRI measurements, show no statistical difference.

Concerning **Vmax** values extracted from MRI ROIs and LOIs V,H: there are statistically significant differences for ROIs in the cases at 10%PO ($p=0.99$ for both 60, 75 bpm), with values at straight position higher. Concerning the values from LOIs H, the latter are also significantly different at 10%PO, but only for the case of 75bpm ($p=0.99$). Significant differences are obvious between the two sequences (QFP, Sqflow, $p=0.9$) in all cases of measurements at 60 bpm, 20% PO (ROIs, LOIs H, LOIs V). Another statistical difference to mention by the comparison between the Vmax values from ROIs vs LOIs H, is observed at 20%PO ($p=0.99$). The elliptical ROIs are considered to be more accurate compared with LOIs, in estimation of velocity values mean and maximum, due to higher area (thus probability) for precise definition of those values. Between values from ROIs vs LOIs V, there is no statistically significant difference. Consequently, LOIs V

appear to be more accurate in estimation contrary to LOIs H. Curves of velocity profiles are optimally fitted at straight position and from vertical LOIs. Figures better agreement is depicted, between straight and inclined position in the horizontal LOIs, as pulsatility increases to 75 bpm. The vertical LOIs lead again to better estimation in both cases of straight and inclined tube. SQflow profiles are optimal versus QFP profiles, and once again confirmation of higher R^2 values from vertical LOIs.

In the case of stenotic tube: Comparison, of **VFR** values at 75, 120 bpm, result in higher flow at the exit of the stenosis (49.16%, 80.14%). In the vicinity of stenosis (± 1cm), VFR is almost stable in the case of 120 bpm (0,74%), whereas the highest variation is noted at 75 bpm (133,9%). The highest VFR value intrastenotic is noted at 120 bpm (82,35ml/s). As flow increases, VFR variation is noted more distal to the stenosis. Percentage comparison indicate that greater variations for 60,75, 120bpm are noted in the vicinity of stenosis (±1cm), whereas for 100bpm at ±3cm.

Considering **Vmax** extracted values at 4cm post stenosis in all cases of pulsatility are higher than the respective values 4cm pre stenosis. At the neck of the stenosis extracted values are indeed high as expected, since laminar flow persists across the stenosis. The highest Vmax value among all intra-stenosis, appears at 60 bpm. As pump flow rate increases, maximum value occurs most post along stenosis. Post stenosis at +1cm (60bpm) and +2cm (75,100,120bpm), variations of Vmax values become higher as pulsatility increases (2.3%-60bpm, 33.7%-75bpm, 25%-100 bpm, 39.8%-120bpm). In the case of LOIs H, the highest intrastenotic value is depicted at 100 bpm flow rate. In the case of LOIs V, the highest intrastenotic value is depicted at 60 bpm flow rate. As aforementioned it is expected values extracted from LOIs to assemble those from ROIs. Post stenosis variations are expected to be higher at higher pulsatility,and are explained by means of Reynolds numbers (Re).

Vertical LOIs result in higher **R squared** values. In lower flow (corresponding to lower pulsatility 60,75bpm as mentioned above), parabolic profiles as noted pre and post stenosis (2cm,1cm pre and 4cm post). For higher flow, (100,120bpm), parabolic profiles are depicted post stenosis (2-4cm) and in the neck of stenosis for 100bpm. Deceleration occurs: 1cm pre (60bpm), 3cm pre (75bpm), 1cm pre (100bpm) and 2cm pre (120bpm), we validate these results by the respective profiles in figures, tables. Indeed, profiles appear flatter at 1cm pre (60bpm), at the neck of stenosis (75bpm), 1cm pre (100, 120bpm) close to predicted regions mentioned above.

Severity of stenosis is calculated as the percentage rate of Vmax upstream or downstream the stenosis to the intrastenotic Vmax, minus the unity. The pump output is set up to 10%, flow rate ranges from 60 to 120 bpm. Calculations account for Vmax values from both ROIs and LOIs (V,H). Measurements from CT scan are also acquired (gold standard) for comparison. Due to turbulence, X_{pre} values are considered as more reliable.

Better agreement for stenosis estimations to ROIs are acquired: in low flow from LOIsV, whereas at higher flow by LOIsH. Since only at 60 bpm, Vpeak appears in the neck of stenosis the respective Xpre values for 60 bpm should be assumed are more reliable, for LOIs and ROIs. Overall, values extracted by MR at 60 bpm imply a stenosis of 46% (LOIsH), 98% (LOIsV) and

93% (ROIs), whereas CT scans estimations lead to 90.2% using diameter stenosis and 99% using area stenosis. The LOIsH expectedly underestimate the percentage of stenosis, it is obvious so far that the estimations extracted from LOIsH, are s the least reliable, in almost every case of parameters' assessment. The CT value of 99% is the exact value, that result by the relationship described in Ota et al.(2005) study: A=D*[2-(D/100)], where D=0,902 is the "diameter stenosis".

Signal to noise ratio as indicative of the loss of signal as fluid flows along the stenosis. Rectangular ROIs are designed upstream and downstream the stenosis, thus SNR values: upstream the stenosis, are higher in contrast to all respective values downstream. Calculations lead to values of: 54.15% (60bpm), 71.08% (75bpm), 68.7% (100bpm) and 72.63% for 120 bpm. The highest loss is depicted at 120 bpm, and in descending order at 75, 100 and 60 bpm.

There are certain factors that are limiting when it comes to comparing the executed study to clinical flow measurements, many of which are connected to properties of the pump and phantom used. At very low pump output as used, there was instability at several times. On the other hand at high PO the pressure reached maximum value (manometer) and was thus avoided. The PO values of 5, 10, 20% are quite lower than that usually found in patients. Thus, a direct comparison to in vivo values would be invalid. The tube in the phantom differs from that of a blood vessel as it is rigid, tube wall consists of PVC or glass, and BMF has different relaxation properties than those found in vivo. Furthermore, the size of the phantom used is much smaller than that of an actual patient, which can lead to a significant divergence in susceptibility variations in scanned material.

Consequently, optimal future projects should include scanning faster flow, higher PO, higher magnitude of 3T, different sequences and modalities (various stenoses, oblique positions, blood mimicking fluids, different vessel walls; to more closely mimic in vivo conditions and to reduce the influence of partial volume effects) and perhaps a comparison among different techniques as ultrasound, computed tomography CT. Turbulence in flow is crucial for comprehension and interpretation of the flow across a stenosis. Hence, complete understanding of the interrelationship between pressure, flow, and symptoms for cardiovascular stenoses is a critical problem. New devices to repair stenotic arteries are continuously being developed. Thus fluid mechanics will continue to play an important role in the future diagnosis, understanding, and treatment of cardiovascular diseases.

Stenosis quantification dependence on the severity of the stenosis using phase contrast MRA

Tables 27 to 31 of chapter 6 present in a tabulated manner the results from the second part of the in-vitro project related to the current thesis.

So far as far as the in-vitro work is concerned, there has been a relation established between pulsatility, SNR ratio and stenosis quantification. For the second part of the in-vitro work the flow-related preconditions are as follows:

A) Steady flow rate (ml/s)

B) Steady pulsatility rate (bpm)

C) Three custom glass-made straight segments, which exhibit a stenotic geometry of unknown severity.

Table 27 depicts the flow related volumetric measurements performed in order to choose an appropriate, physiological-relate flow rate within the glass segment. It appears that as the pump output increases the flow rate volume increases and so does the pressure at the upper end of the pump. All the results in table 27 represent flow volumes that are regularly seen in small to medium sized human arteries under physiological conditions.

Table 28 shows the ratio of the measured SNR at and pre-stenotically. As expected the factor of SNR_{ratio} is the one that enables us to realize –in part- the severity of the stenotic geometry. Based upon this fact, in the particular cases examined, the first stenosis seems to exhibit the smallest loss of SNR post stenotically and thus it is expected to be the closest to the MSCT gold standard which is presented in table 31.

Table 30 shows the calculated R^2 values of the quadratic fits procedure that was followed for all three stenotic geometries at various perpendicular directions to the flow at 7.5, 6, 4.5, 3, 1.5 pre- and at 1.5, 3, 4.5, 6 and 7.5 cm post-stenotically. One might expected the velocity profiles to be very kyrtotic but in reality this does not seem to be the case. The average value of the R2 factor is 95, 96 and 93 for stenosis 1, and 3 respectively.

Table 31 present the calculated percentage stenosis for each of the three segments using velocity data at various distances pre- and post- stenotically at constant flow volume and pulsatility.

Depending on the site of measurement, results seem to differ considerably. For example stenosis 1 is calculated to be 92% based upon LOI SMCT measurements. The closest value to it from the MRA is found at the most distal pre-stenotic part of the segment, i.e. 7.5 cm pre-stenotically.

The same appears to be valid for stenosis number 3. MSCT data place the true percentage at 88.2%. The value of the MRA closest to this is technique is 84.14% found at 3 cm pre stenotically.

The most perplexing value is the quantification of the second stenotic tube (stenosis 2). The value measured by MSCT is 91%. There seems to be a large discrepancy between this value and the closest one achieved through MRA which is 80.38% found at 4.5 cm pre stenotically. This unexpected behavior cannot seem to be able to be resolved based upon the current analysis. The most likely reason is the fact that due to the hand-made construction of the segment; it is possible that this particular stenosis exhibited a non-symmetric geometry, a fact that cannot be derived from the observation of the R^2 factor, which for this particular segment is as high as the other two. The fact that directly points towards the reason for the miscalculation of stenosis 2 lies within the SNR_{loss} factor which for this segment is of the order of 65%. This is directly linked to a false velocity reading which in turn leads to a false results for the stenosis quantification.

From the analysis above it is evident that stenosis quantification based upon MRA-derived velocity maps is feasible if and only if the site of measurement lies pre- stenotic and flow profile together with SNR_{loss} analysis has been performed.

CONCLUSIONS

IN VIVO

Wall shear stress measurements in the arterial tree using PC-MRI

In vivo data for WSS measured in healthy humans exist for the following arteries: carotid arteries, brachial arteries, aorta and femoral arteries. WSS values are not constant within the arterial system but are site specific. WSS values at the same site measured by different investigators show qualitative agreement; however, differences exist in absolute values due to the methodology utilized in each study. The main limitation of PC-MRI is its spatial and temporal resolution that limits the accuracy of shear stress assessment near the vessel wall.

Wall shear stress calculation in the human ascending aorta using Poiseuille's equations

Our results indicate that the four methods that have been proposed for WSS calculations in the ascending aorta give similar results. Thus, in clinical practice, one can adopt the method which is most easy and convenient for the user to apply. Our data indicate that all methods provide results with no statistically significant differences. The applicability of the straightforward methods based on Poiseuille's theory of flow relies on the existence of parabolic velocity distribution inside the aortic lumen. Therefore, the parabolic behavior of flow in the ascending aorta has to be tested prior of selecting the measuring method. This test can be performed with the parabolic fit proposed in this study. Further work should be done to examine the results that different methods give when the profile of blood velocities inside the vessel is not parabolic.

Wall shear stress calculation in the human ascending aorta throughout the cardiac cycle

Estimation of systolic and diastolic WSS in the human ascending aorta is feasible by flow measurements obtained by phase-contrast MRI and the use of methodologies based on Poiseuille's

theory of flow. However, the theoretically equivalent mathematical formulas do not yield equivalent results. It appears that when maximum blood flow velocity is used, the resulting WSS values are higher than the values obtained by the methodologies that utilize average volume flow or average velocity in the arterial lumen. This fact points towards the need of careful selection of the measuring methodology of WSS calculation at the human arterial tree especially when maximum WSS is to be considered as the parameter under investigation. When WSS is to be calculated at a particular phase of the cardiac cycle (e.g. at peak-systole or end-diastole) then the AF and the MV methods produce equivalent results. Methods based on the mean volume flow or the mean flow velocity should be preferably used for WSS calculations by phase-contrast MRI.

IN VITRO

Stenosis quantification dependence on the pulsatility of flow using phase contrast MRA

The performance of flow measurements with phase contrast MRI was studied for different flow directions (obliquity), pulse sequences and tubes. For each set-up a range of different flow velocities was scanned. The results show that in a controlled setting, with flow through a phantom and pump, it is possible to get good measurements of pulsating flow, with differences between methods statistically insignificant. Differences were only noted at obliquity of the tube (V_{max} values) at 10%PO, but as mentioned above, the sample of measurements is small and does not permit safe conclusions. At 10%PO coefficient of variation in volumetric VFR values was also noted. Those differences perhaps could be attributed to the pumps' lower performance at low PO values. '*Sqflow'* sequence, seems to provide more reliable values in comparison to '*QFP'*. Also in almost all cases vertical LOIs seem to be more accurate in estimations of values and velocity profiles, contrary to horizontal LOIs that prevented proper design. At high pulsatility VFR values appear almost stable at the vicinity of stenosis, and result in higher values. High pulsatility seems to shift VFR, Vmax variations rightmost along the stenosis. At higher pulsatility SNR ratio is also higher. In low pulsatility, loss of energy seem to occur earlier, thus Vmax value appear at the neck of the stenosis, contrary to higher pulsatility, where it appears later. Vmax values post stenosis are higher than those pre stenosis. The presence of the jet indicate, a more extended study with measurements over longer distance post stenosis. The percentage of stenosis is accurately estimated by MRI (93%, 98%), excluding the value from LOIsH, in comparison to the CT values of 90% and 99%.

The magnitude of the errors are shown to be dependent on the size of the ROI selected, as in stenotic tube the estimation of area is far more uncertain, indicating the importance of carefully selecting the right area for which to calculate the flow rate. To examine why flow measurements

made clinically show large errors further investigation is needed. Future projects should include scanning faster flow, higher PO, higher magnitude of 3T, different sequences and modalities (various stenoses, oblique positions, and blood mimicking fluids, different vessel walls; to more closely mimic in vivo conditions and to reduce the influence of partial volume effects) and perhaps a comparison among different techniques as ultrasound, computed tomography. Also, currently the clinical studies make use of a phase offset correction that entails scanning of phantom after the patient 40 examination for reference. This procedure could maybe be verified using a phantom with known flow.

More importantly, our study reinforces concerns about the accuracy of clinical measurements that rely on simplistic assumptions about velocity profile shape. Further understanding of the role of compound curvature in flow and mass transport may also help inform the design of engineered arterial conduits. In fluid dynamics, turbulent flow is a flow regime characterized by chaotic and stochastic property changes, thus estimation becomes difficult. Apparat from difficult, turbulent flow is crucial for comprehension and interpretation of the flow across a stenosis. Hence, complete understanding of the interrelationship between pressure, flow, and symptoms for cardiovascular stenosis is a critical problem. New devices to repair stenotic arteries are continuously being developed. Thus fluid mechanics will continue to play an important role in the future diagnosis, understanding, and treatment of cardiovascular diseases.

Stenosis quantification dependence on the grade of the stenosis using phase contrast MRA

Finally, this work has shown that stenosis quantification is feasible for steady flow rate and pulsatility with varying percentage of lumen stenosis. Comparison was carried out successfully with stenosis quantification in 3 glass-made segments using MSCT image acquisition. Data extraction from ultrasound was not possible due to the high reflectivity index of the glass-material. Comparison with digital subtraction angiography was also not possible due the high reflectivity material. As a result, MSCT was used as a standard reference for the purpose of this work.

Pump output was set at 10% and pulsatility was set at 75 beats per minute in order to simulate best physiological rheological conditions. The stenotic percentage calculated for the three stenotic geometries was 9% lower for the first segment, 38% lower for the second segment (which was the highest stenotic grading according to MSCT) and identical for the third stenotic segment.

Flow disturbances due to the stenotic geometry can play a significant and negative role in the quantification procedure, as high turbulence leads to substantial signal loss and thus the acquired velocity maps suffer from loss of true velocity values, making stenosis quantification using magnetic resonance angiography prone to uncertainties.

FUTURE PROSPECTIVES

The purpose of the present work has been the presentation to the scientific community of a scientific approach to one of the most promising blood-flow-related rheological factors that exhibits interesting and useful clinical hemodynamic parameters. This factor is the arterial WSS. Along with the effort to better understand the behavior of this factor, came another interesting set of parameters that are related to the WSS either directly (such as the flow parabolicity, mean and maximum blood flow velocity) or indirectly (such as the imaging technique and the other flow related parameters that can be studied based upon the Poiseuille's model of flow).

Even though far for being complete, this work has proven the fact that under the Poiseuille's model of flow, WSS calculation IS feasible under Magnetic Resonance Angiography Imaging and it CAN lead to useful clinical conclusions. Of course, there are inevitably a certain number of limiting factors that could improve the present work towards even more clinically meaningful conclusions.

More in particular, 2D magnetic angiography seems to be becoming methodology of the recent past already, as it is being substituted by 3D or even 4D phase contrast velocity mapping. The latter can undoubtedly provide research community with real time 2D velocity filed mapping, which in turn can lead to a more accurate determination of the spatial distribution of arterial WSS.

As far as the IN VITRO part is concerned, the reality of complete simulation of blood circulation using experimental set up is slowly but steadily becoming more and more of a reality.

One of the key contributors to this is the rapidly evolving technology of 3D printing, which in this project could have enabled the user to draw vital conclusions about the hemodynamic behavior of blood flow. One limitation for the experimental work has been the lack of truly realistic geometry. More in particular, the validity of the Poiseuille's theory of flow was tested under the usual boundary conditions imposed by the physical and mathematical formulation of flow. For this reason WSS calculation was impossible, since the tubing was glass made with no wall elasticity or distensibility. Any set of acquired results would have been impossible to juxtapose to real in vivo data. This obstacle will be overcome as soon as 3D print devices can operate with materials that exhibit mechanical properties similar to the human endothelium.

This idea has already starting to become a reality in our laboratory since the first 3D segment of a human carotid has been printed on ceramic material following segmentation of a MSCT imaging data. Analytical description of the procedure is planned to be published when the research part of it is ready. The printed segment with the tissue-equivalent material and with its incorporation to the current experimental set up can provide extremely useful information on the ongoing research for the establishment of a straightforward relationship between hemodynamic characteristics of blood flow using MRA and clinical outcomes.

REFERENCES

[1] Morgan, B. E. and D. F. Young. 1974. "An Integral Method for the Analysis of Flow in Arterial Stenosis.*"*Bull. math. Biol.*,**36**, 39–53*

[2] Siggers Jennifer, 2009 Physiological Fluid Mechanics 10.2217/IIM.10.33 © 2010 Future Medicine Ltd Imaging Med. (2010) 2(4), 445–457 ISSN 1755-5191 445

[3] Guyton Arthur C., John E. Hall 2006 Textbook of Medical Physiology 11th edition, chapt.9; 103-110, 14;162-170, 15; 171-179

[4] Kraft SA, Larson CP, Shuer LM, Steinberg GK, Benson GV & Pearl RG. (1990) Effect of hyperglycemia on neuronal changes in a rabbit model of focal cerebral ischemia. Stroke21: 447−450.

[5] Berguer R, Cotton LT. Reversed autogenous saphenous vein by-pass from the common to the deep femoral (profunda femoris) artery.Br J Surg. 1973 Sep;60(9):676-9.

[6] Opdyke DF: Fed Proc 11:734, 1952

[7] https://www.cis.rit.edu/htbooks/mri/

[8] Firbank M J, R M Harrison, E D Williams, A Coulthard. Quality assurance for MRI: practical experience. The British Journal of Radiology, 73 (2000), 376-383.

[9] Firbank M J, A Coulthard, R M Harrison and E D Williams. A comparison of two methods for measuring the signal to noise ratio on MR images. Phys. Med. Biol. 44 (1999) N261–N264

[10] Goerner Frank and Geoffrey D. Clarke. Measuring signal-to-noise ratio in partially parallel imaging MRI. 2011 American Association of Physicists in Medicine. [DOI: 10.1118/1.3618730]

[11] Mascaro L, Strocchi S, Colombo P, Del Corona M, Baldassarri AM. Definition criteria for a magnetic resonance quality assurance program: multicenter study. Radiol Med. 1999 May;97(5):389-97.

[12] Smith B Travis & Krishna S Nayak. MRI artifacts and correction strategies. Imaging Med. (2010) 2(4), 445–457

[13] Niranjan Balu, Jinnan Wang, Li Dong, Florence Baluyot, Huijun Chen, and Chun Yuan.

Current Techniques for MR Imaging of Atherosclerosis. TMRI 08/2009; 20(4): 203-15

[14] Yuan Chun, Minako Oikawa, MD, Zach Miller, Thomas Hatsukami, [6d] MRI of Carotid Atherosclerosis 2008 J Nucl Cardiol.; 15(2): 266 -275.

[15] Corti Roberto. Noninvasive imaging of atherosclerotic vessels by MRI for clinical assessment of the effectiveness of therapy.Pharmacol Ther. 2006 Apr; 110(1):57-70. Epub2006 Jan 30

[16] Manbachi Amir, Yiemeng Hoi, Bruce A Wasserman, Edward G Lakatta and David A Steinman, 2011 On the shape of the common carotid artery with implications for blood velocity profiles, Physiol. Meas. 32 1885–1897

[17] Ku David. Blood flow in arteries. Annu. Rev. Fluid Mech. 1997. 29:399–434

[18] Chalela J.A. Evaluating the Carotid Plaque: Going beyond Stenosis. Cerebrovasc Dis 2009;27 (Suppl. 1):19-24

[19] Tomiyama Hirofumi; Akira Yamashina. Non-Invasive Vascular Function Tests: Their Pathophysiological Background and Clinical Application.CircJ. 2010 Jan;(1): 24-33. Epub 2009 Nov 17.

[20] Cai Jianming, Thomas S. Hatsukami, Marina S. Ferguson, William S. Kerwin,Tobias Saam, Baocheng Chu, Norihide Takaya, Nayak L. Polissar, Chun Yuan. In Vivo Quantitative Measurement of Intact Fibrous Cap and Lipid-Rich Necrotic Core Size in Atherosclerotic Carotid PlaqueComparison of High-Resolution, Contrast-Enhanced Magnetic Resonance Imaging and Histology. Circulation 2005; 112:3437-3444, Nov 21 2005.

[21] Kramer CM, et al. Magnetic resonance imaging identifies the fibrous cap in atherosclerotic abdominal aortic aneurysm. Circulation. 2004;109:1016–1021.

[22] Saam T, et al. Comparison of symptomatic and asymptomatic atherosclerotic carotid plaque features with in vivo MR imaging. Radiology. 2006;240:464–472.

[23] Tang C, Blatter DD, Parker DL. 1993. Accuracy of phase-contrast flow measurements in the presence of partial volume effects. Journal of Magnetic Resonance Imaging. 3:377- 385.

[24] Groen HC, et al. Plaque Rupture in the Carotid Artery is Localized at the High Shear Stress Region: A Case Report. Stroke. 2007;38:2379–2381.

[25] Kraft K.A., P.P. Fatouros, D.Y. Fei, S.E. Rittgers, P.R.S. Kishore. MR Imaging of model fluid velocity profiles. Magnetic resonance Imaging, vol.7, pp. 69-77, 1989

[26] Gatehouse P., Jennifer Keegan, Lindsey A. Crowe, Sharmeen Masood, Raad H. Mohiaddin, Karl-Friedrich, Kreitner, David N. Firmin. Applications of phase-contrast flow and velocity imaging in cardiovascular MRI. European Radiology 11/2005;15(10): 2171-84

[27] Oshinski John, W. James Parks, Christos P. Markou, Harris L. Bergman, Blake E. Larson, David N. Ku, Srinivasan Mukundan, Roderik I. Pettigrew. Improved Measurement of Pressure Gradients in Aortic Coarctation by Magnetic Resonance Imaging. AJJ Vol. 28, No. 7, December 1996:1818–26.

[28] Asakura T, Karino T. Flow patterns and spatial distribution of atherosclerotic lesions in humancoronary arteries. Circ Res, 66(4), 1045-1066 (1990).

[29] Feldman CL, Stone PH. Intravascular hemodynamic factors responsible for progression of coronary atherosclerosis and development of vulnerable plaque. Curr Opin Cardiol, 15(6), 430-440 (2000).

[30] Kassab GS, Fung YC. The pattern of coronary arteriolar bifurcations and the uniform shear hypothesis. Ann Biomed Eng, 23(1), 13-20 (1995).

[31] Malek AM, Alper SL, Izumo S. Hemodynamic shear stress and its role in atherosclerosis. Jama, 282(21), 2035-2042 (1999).

[32] Chatzizisis YS, Coskun AU, Jonas M et al. Role of endothelial shear stress in the natural history of coronary atherosclerosis and vascular remodeling: molecular, cellular, and vascular behavior. J Am Coll Cardiol, 49(25), 2379-2393 (2007).

[33] de Nigris F, Williams-Ignarro S, Lerman LO et al. Beneficial effects of pomegranate juice on oxidation-sensitive genes and endothelial nitric oxide synthase activity at sites of perturbed shear stress. Proc Natl Acad Sci U S A, 102(13), 4896-4901 (2005).

[34] Voetsch B, Jin RC, Loscalzo J. Nitric oxide insufficiency and atherothrombosis. Histochem Cell Biol, 122(4), 353-367 (2004).

[35] Ravensbergen J, Ravensbergen JW, Krijger JK, Hillen B, Hoogstraten HW. Localizing role of hemodynamics in atherosclerosis in several human vertebrobasilar junction geometries. Arterioscler Thromb Vasc Biol, 18(5), 708-716 (1998).

[36] Butcher JT, Tressel S, Johnson T et al. Transcriptional profiles of valvular and vascular endothelial cells reveal phenotypic differences: influence of shear stress. Arterioscler Thromb Vasc Biol, 26(1), 69-77 (2006).

[37] Cunningham KS, Gotlieb AI. The role of shear stress in the pathogenesis of atherosclerosis. Lab Invest, 85(1), 9-23 (2005).

[38] Gimbrone MA, Jr., Topper JN, Nagel T, Anderson KR, Garcia-Cardena G. Endothelial dysfunction, hemodynamic forces, and atherogenesis. Ann N Y Acad Sci, 902, 230-239; discussion 239-240 (2000).

[39] Davies PF. Flow-mediated endothelial mechanotransduction. Physiol Rev, 75(3), 519-560 (1995).

[40] Wang N, Miao H, Li YS et al. Shear stress regulation of Kruppel-like factor 2 expression is flow pattern-specific. Biochem Biophys Res Commun, 341(4), 1244-1251 (2006).

[41] Oshinski JN, Curtin JL, Loth F. Mean-average wall shear stress measurements in the common carotid artery. J Cardiovasc Magn Reson, 8(5), 717-722 (2006).

[42] Strackee J, Westerhof N. The Physics of Heart and Circulation (Institute of Physics Publishing, Bristol, 1993).

[43] Rowan JO. Physics and the Circulation (ed. Lenihan, PJMA) (Adam Hilger Ltd, Bristol, 1981).

[44] Milnor W. Hemodynamics (Williams & Wilkins, 1982).

[45] Nichols W, O'Rourke M. McDonald's Blood Flow in Arteries : Theoretical, Experimental and Clinical Principles (Hodder Arnold, 2005).

[46] Reneman RS, Arts T, Hoeks AP. Wall Shear Stress - an Important Determinant of Endothelial Cell Function and Structure - in the Arterial System in vivo. Discrepancies with Theory. J Vasc Res, 43(3), 251-269 (2006).

[47] Lou Z, Yang WJ, Stein PD. Errors in the estimation of arterial wall shear rates that result from curve fitting of velocity profiles. J Biomech, 26(4-5), 383-390 (1993).

[48] Oshinski JN, Ku DN, Mukundan S, Jr., Loth F, Pettigrew RI. Determination of wall shear stress in the aorta with the use of MR phase velocity mapping. J Magn Reson Imaging, 5(6), 640-647 (1995).

[49] Guo Z, Moreau M, Rickey DW, Picot PA, Fenster A. Quantitative investigation of in vitro flow using three-dimensional colour Doppler ultrasound. Ultrasound Med Biol, 21(6), 807-816 (1995).

[50] Lotz J, Meier C, Leppert A, Galanski M. Cardiovascular flow measurement with phase-contrast MR imaging: basic facts and implementation. Radiographics, 22(3), 651-671 (2002).

[51] Greil G, Geva T, Maier SE, Powell AJ. Effect of acquisition parameters on the accuracy of velocity encoded cine magnetic resonance imaging blood flow measurements. J Magn Reson Imaging, 15(1), 47-54 (2002).

[52] Powell AJ, Tsai-Goodman B, Prakash A, Greil GF, Geva T. Comparison between phase-velocity cine magnetic resonance imaging and invasive oximetry for quantification of atrial shunts. The American journal of cardiology, 91(12), 1523-1525, A1529 (2003).

[53] Shaaban AM, Duerinckx AJ. Wall shear stress and early atherosclerosis: a review. AJR Am J Roentgenol, 174(6), 1657-1665 (2000).

[54] Yim P, Demarco K, Castro MA, Cebral J. Characterization of shear stress on the wall of the carotid artery using magnetic resonance imaging and computational fluid dynamics. Stud Health Technol Inform, 113, 412-442 (2005).

[55] Masaryk AM, Frayne R, Unal O, Krupinski E, Strother CM. In vitro and in vivo comparison of three MR measurement methods for calculating vascular shear stress in the internal carotid artery. AJNR Am J Neuroradiol, 20(2), 237-245 (1999).

[56] Oyre S, Ringgaard S, Kozerke S et al. Accurate noninvasive quantitation of blood flow, cross-sectional lumen vessel area and wall shear stress by three-dimensional paraboloid modeling of magnetic resonance imaging velocity data. J Am Coll Cardiol, 32(1), 128-134 (1998).

[57] Wu SP, Ringgaard S, Pedersen EM. Three-dimensional phase contrast velocity mapping acquisition improves wall shear stress estimation in vivo. Magn Reson Imaging, 22(3), 345-351 (2004).

[58] Wu SP, Ringgaard S, Oyre S et al. Wall shear rates differ between the normal carotid, femoral, and brachial arteries: an in vivo MRI study. J Magn Reson Imaging, 19(2), 188-193 (2004).

[59] Stokholm R, Oyre S, Ringgaard S et al. Determination of wall shear rate in the human carotid artery by magnetic resonance techniques. Eur J Vasc Endovasc Surg, 20(5), 427-433 (2000).

[60] Oyre S, Pedersen EM, Ringgaard S, Boesiger P, Paaske WP. In vivo wall shear stress measured by magnetic resonance velocity mapping in the normal human abdominal aorta. Eur J Vasc Endovasc Surg, 13(3), 263-271 (1997).

[61] Pedersen EM, Oyre S, Agerbaek M et al. Distribution of early atherosclerotic lesions in the human abdominal aorta correlates with wall shear stresses measured in vivo. Eur J Vasc Endovasc Surg, 18(4), 328-333 (1999).

[62] Milnor W, Hemodynamics, Baltimore. Williams & Wilkins 1982

[63] Pearson T C. Hemorheology in the erythrocytoses, Mt Sinai J Med 2001: 68; 182-91

[64]Nichols W and O'Rourke M, McDonald's Blood Flow in Arteries : Theoretical, Experimental and Clinical Principles, Hodder Arnold 2005

[65] Nichols W and O'Rourke M, McDonald's Blood Flow in Arteries: Theoretical, Experimental and Clinical Principles, New York. Hodder Arnold 2005

[66] Abramoff M D, Magelhaes, P.J., Ram, S.J. Image Processing with ImageJ, Biophotonics International 2004: 11; 36-42

[67] Doriot P A, Dorsaz P A, Dorsaz L, De Benedetti E, Chatelain P, and Delafontaine P. In-vivo measurements of wall shear stress in human coronary arteries, Coron Artery Dis 2000: 11; 495-502

[68] Katritsis D, Kaiktsis L, Chaniotis A, Pantos J, Efstathopoulos E P, and Marmarelis V. Wall shear stress: theoretical considerations and methods of measurement, Prog Cardiovasc Dis 2007: 49; 307-29

[69] Thury A, van Langenhove G, Carlier S G, Albertal M, Kozuma K, Regar E, Sianos G, Wentzel J J, Krams R, Slager C J, Piek J J, and Serruys P W. High shear stress after successful balloon angioplasty is associated with restenosis and target lesion revascularization, Am Heart J 2002: 144; 136-43

[70] He X and Ku D. Pulsatile flow in the human left coronary bifurcation: average conditions, J Biomech Eng 1996: 118; 74-82

[71] Pettigrew Roderic, Wayne Dannels. Use of standard gradients with Compound Oblique Angulation for Optimal Quantitative MR Flow Imaging in Oblique Vessels. AJR 148:405-409, February 1987

[72] Kassab GS, Fung YC. The pattern of coronary arteriolar bifurcations and the uniform shear hypothesis. *Ann Biomed Eng*, 23(1), 13-20 (1995).

[73]LaBarbera M. Principles of design of fluid transport systems in zoology. *Science*, 249(4972), 992-1000 (1990).

[74]. Pries AR, Secomb TW, Gaehtgens P. Design principles of vascular beds. *Circ Res*, 77(5), 1017-1023 (1995).

[75] Kraiss LW, Kirkman TR, Kohler TR, Zierler B, Clowes AW. Shear stress regulates smooth muscle proliferation and neointimal thickening in porous polytetrafluoroethylene grafts. *Arterioscler Thromb*, 11(6), 1844-1852 (1991).

[76] Busse R, Fleming I. Pulsatile stretch and shear stress: physical stimuli determining the production of endothelium-derived relaxing factors. *J Vasc Res*, 35(2), 73-84 (1998).

[77] Melkumyants AM, Balashov SA, Veselova ES, Khayutin VM. Continuous control of the lumen of feline conduit arteries by blood flow rate. *Cardiovasc Res*, 21(12), 863-870 (1987)

[78] Pantos I, Patatoukas G, Efstathopoulos E P, and Katritsis D. In vivo wall shear stress measurements using phase-contrast MRI, Expert Rev Cardiovasc Ther 2007: 5; 927-38

[79] Doriot P A, Dorsaz P A, Dorsaz L, De Benedetti E, Chatelain P, and Delafontaine P. In-vivo measurements of wall shear stress in human coronary arteries, Coron Artery Dis 2000: 11; 495-502

[80] Katritsis D, Kaiktsis L, Chaniotis A, Pantos J, Efstathopoulos E P, and Marmarelis V. Wall Shear Stress: Theoretical Considerations and Methods of Measurement, Prog Cardiovasc Dis 2007: 49; 307-329

[81] Thury A, van Langenhove G, Carlier S G, Albertal M, Kozuma K, Regar E, Sianos G, Wentzel J J, Krams R, Slager C J, Piek J J, and Serruys P W. High shear stress after successful balloon angioplasty is associated with restenosis and target lesion revascularization, Am Heart J 2002: 144; 136-43

[82] Cheng C, Helderman F, Tempel D, Segers D, Hierck B, Poelmann R, van Tol A, Duncker D J, Robbers-Visser D, Ursem N T, van Haperen R, Wentzel J J, Gijsen F, van der Steen A F, de Crom R, and Krams R. Large variations in absolute wall shear stress levels within one species and between species, Atherosclerosis 2006

[83] Bendel Peter, Edward Buonocore, Andreas Bockisch, Myrwood C. Besozzi. Blood Flow in the Carotid Arteries: Quantification by Using Phase-Sensitive MR Imaging. AJR 152:1307-1310, June 1989

APPENDIX

Below is presented the code itself, which was used in Matlab language in order to fit the right parabolic equation, calculate shear rate (SR) and finally wall shear stress (WSS) according to the format of the Linear Method (LM) as described in chapter 3 of the present thesis

%%%Matlab code for calcuation SR,WSS and comparison%%%

%CALCULATION OF CONSTRAINED PARABOLIC FIT, SHEAR RATE AND WALL SHEAR STRESS FOR A GIVEN SET OF DATA%

%%%Matlab code for calcuation of fitting equation%%%

```
% x1=input('Enter x1 value=       ');
% x2=input('Enter x2 value=       ');
% y1=input('Enter y1 value=       ');
% y2=input('Enter y2 value=       ');
1=x(1);
x2=x(end);
y1=y(1);
y2=y(end);
beta1=((y2-y1)/(x2-x1));
beta2=(x2+x1);
beta3=(x2*x1);
disp('The parabolic fit equation for this set of data is :')
disp('(a*x^2+)');disp('[');disp(beta1);disp('-
a*');disp(beta2);disp(']');disp('x');disp('[');disp(y(1));disp('+a*');disp(beta3);disp('-
');disp(beta1);disp(']');
```

%%%Matlab code for calcuation SR,WSS and comparison%%%

```
%  a=input('Enter a value for the alpha parameter=  ');
%
% x1=x(1);
% x2=x(2);
% y1=y(1);
% y2=y(2);
%
% SR1=((y2-y1)/(x2-x1))-(a*(x2+x1));
% SR2=((y2-y1)/(x2-x1));
% disp('The SR value at point 1 according to the parabolic fit is:')
% disp(SR1);
% disp('The SR value at point 1 according to the raw data is:')
% disp(SR2);
% % gamma=(sum(y)-a*(sum(x.^2)-beta.*(sum(x)))./(19);
% % disp(gamma);
% WSS1=(0.0035)*(SR1);
% disp('The WSS value at point 1 according to the parabolic fit SR is:')
% disp(WSS1);
% disp('The WSS value at point 1 according to the raw data SR is:')
% WSS2=(0.0035)*(SR2);
% disp(WSS2);
%  SR_diff=(abs((SR1-SR2)/(SR1+SR2)))*100;
%  disp('The SR difference at point 1 is:')
% disp(SR_diff);
% WSS_diff=(abs((WSS1-WSS2)/(WSS1+WSS2)))*100;
%  disp('The WSS  difference at point 1 is:')
```

```
% disp(WSS_diff);
%
% x1=x(end);
% x2=x(end-1);
% y1=y(end);
% y2=y(end-1);
%
% SR3=abs((2*a*x1)-((y2-y1)/(x2-x1))-(a*(x2+x1)));
% SR4=abs(((y2-y1)/(x2-x1)));
% disp('The SR value at point 2 according to the parabolic fit is:')
% disp(SR3);
% disp('The SR value at point 2 according to the raw data is:')
% disp(SR4);
% % gamma=(sum(y)-a*(sum(x.^2)-beta.*(sum(x)))./(19);
% % disp(gamma);
% WSS3=(0.0035)*(SR3);
% disp('The WSS value at point 2 according to the parabolic fit SR is:')
% disp(WSS3);
% disp('The WSS value at point 2 according to the raw data SR is:')
% WSS4=(0.0035)*(SR4);
% disp(WSS4);
%  SR_diff_2=(abs((SR3-SR4)/(SR3+SR4)))*100;
%  disp('The SR difference at point 2 is:')
% disp(SR_diff_2);
% WSS_diff_2=(abs((WSS3-WSS4)/(WSS3+WSS4)))*100;
%  disp('The WSS difference at point 2 is:')
% disp(WSS_diff_2);
```